HETERODYNE DETECTION WITH SUPERCONDUCTING TUNNEL DIODES

Thesis by

Michael James Wengler

In Partial Fulfillment of the Requirements

for the Degree of

Doctor of Philosophy

California Institute of Technology

Pasadena, California

1988

(Submitted June 5, 1987)

Make him [the reader] laugh and he will think you a trivial fellow, but bore him in the right way and your reputation is assured.

—W. Somerset Maugham

Acknowledgements

First and foremost, thanks to my friend and constant collaborator Dave Woody, who has worked closely with me on every bit of work that has gone into this thesis. More importantly, he has deeply affected the way I live and work. Dave is in research because he likes it. He is very negligent in the pursuit of politics and mistrust of colleagues, which seems so essential to a successful scientific career. When I start to worrying about being beaten to the presses, or tenure, or the elusiveness of fame, my experiences with Dave will remind me that research is not worth giving up for a career. And I would probably want to continue working with Dave in the future, even if he didn't live so close to Mammoth.

The direction which my research has taken owes much to my advisor, Tom Phillips. He treated me as though I was a mature and independent researcher from the day I started here, and I think I may have finally become one in his labs. He has supported my research in a grand style during my long tenure as his student.

The experimental work in this thesis would not have been possible without Ron Miller at AT&T Bell Labs. He happily devoted months of his time to the difficult task of fabricating the very fast SISs required for the SIS-bowtie mixer. For his essential contribution to the success of this mixer, I thank him. I would also like to acknowledge the hospitality he has extended to me, both in his lab and in his home during my summer visits to Bell Labs.

I am pleased to thank my fellow inmates in Caltech's submillimeter group for their contributions to my thesis. We have something special here, which I will be missing soon enough. I am pleased to specifically acknowledge a representative sample of seven years of close interactions, both scientific and otherwise. Dan Watson's encyclopedic knowledge of optics, cryogenics, detectors, artwork, and life in general have contributed tremendously to this thesis work. Dan also carried out the two highest frequency measurements of the SIS-bowtie mixer, along with Thomas Buettgenbach. Finally, I thank Dan for a hundred drinks in the Ath, which have contributed to this thesis in ways which neither of us can remember. Erich Grossman tutored me in the *arcana* of photon operators, coherent states, and other aspects of quantum mechanics when I was trying to figure out the quantum heterodyne theory. He also introduced me to Melville and *Moby Dick*. Years of sharing an office with Elliott Brown were

Abstract

Heterodyne receivers based on superconductor-insulator-superconductor (SIS) tunnel diodes are the most sensitive available for near-millimeter wavelengths. Since the late seventies, receivers based on SISs have been used for millimeter band observations at radio observatories around the world. The work described here was carried out with the elusive goal in mind of developing ideal SIS receivers for radioastronomy. This thesis describes one researcher's path towards this goal.

In the first chapter, a basic description of SIS diodes, their interaction with radiation, and heterodyne detection are given. The important detailed results of J. R. Tucker's tunnel diode heterodyne theory are described, since subsequent chapters rely on Tucker's work quite heavily. Throughout this introductory chapter, extremely simple (by comparison with the algebraic theoretical results) physical models are used to describe superconductivity, SISs, photon-assisted tunneling, and heterodyne detection. It is the author's experience that these physical models can be used to derive correct theoretical results, long before these results are proved rigorously.

The second chapter presents a fully quantum mechanical theory of heterodyne detection with diodes. This theory was developed because Tucker's theory for tunnel diodes predicts a greater mixer sensitivity than is possible considering Heisenberg's uncertainty principle for radiation. Tucker does not quantize the radiation incident on the SIS, although his treatment of the isolated tunnel diode is completely quantum mechanical. In chapter 2, the quantization of radiation is carried out for heterodyne diode detectors. The formalism is shown to obey quantum limits on sensitivity. Finally, an ideal SIS mixer is shown to have noise properties identical to those of optical mixers based on ideal photodiodes.

In possession of an apparently complete theory for SIS mixers, the third chapter presents a sampling of numerical results from that theory. Four different non-ideal tunnel diodes are used for these calculations so that a quantitative feel for the importance of diode quality can be achieved. The effects of dc and LO bias, signal and image source admittance, frequency of operation, and junction quality are all explored. This information will be useful for the proper engineering of SIS mixers. Finally, the fully optimized performance of the four tunnel diodes is presented as frequency is varied. It is shown that reasonably good quality lead-alloy SISs should behave like photodiodes up to frequencies as high

as 1500 GHz.

Finally, chapter 4 presents a prototype open-structure SIS mixer. Measurements in the laboratory show this mixer to be quite sensitive for signal frequencies from 115 to 761 GHz. Unlike all other SIS receivers, in which the diode is mounted across a waveguide, this mixer relies on the bowtie-on-quartz antenna structure, which has been investigated by D. B. Rutledge and his students. This difference is essential to the multi-octave spectral coverage of this mixer. It is probable that waveguide designs will never achieve good results above 500 GHz, and as of now, there are no SIS-waveguide mixers which operate well above 300 GHz. Tests at the Owens Valley Radio Observatory verify the suitablility of this mixer for radioastronomy, but these tests have been limited to frequencies of 260 GHz and lower.

Table of Contents

List of Figures

Chapter 1 – SISs and Radiation Detection

"Be it known that, waiving all argument, I take
the good old fashioned ground that the whale is a fish,
and call upon holy Jonah to back me."
—Herman Melville, in *Moby Dick*.

1.1 Thesis Overview

An SIS (superconductor-insulator-superconductor) is a diode in which current flows due to tunneling

of electrons from one superconductor to another. Illuminated by coherent radiation of frequency ν,

two features of SISs as radiation detectors become apparent. First, incredibly low power levels are

required to see effects on the SIS. This implies an extremely high sensitivity to radiation, which makes

them overwhelmingly appealing to radioastronomers, who use them to detect fainter and fainter sources.

Second, the SIS current-voltage relationship (*I-V*) shows structure at voltages with characteristic spacings

of $h\nu/e$ and $h\nu/2e$. Classical theories for radiation detection by diodes are absolutely unable to deal

with this. Truly quantum theories, in which both the wave and the particle nature of light are relevant,

must be used to describe their performance.

An elegant quantum mechanical theory for these devices as mixers was developed by Tucker

(1979). Unlike devices which fit the classical mixer theory (Torrey and Whitmer, 1948), these devices

are capable of power gain on downconversion. This non-classical feature of SIS mixers has been verified

experimentally (McGrath *et al.*, 1981; Face *et al.*, 1986). The power conversion efficiency predictions

of this theory have been verified quantitatively (Phillips and Dolan, 1982; Feldman and Rudner, 1983;

Feldman *et al.*, 1983).

This theory predicts that good quality SIS diodes can achieve nearly perfect sensitivity as heterodyne

detectors. Unfortunately, this prediction violates measurement limits imposed by quantum mechanics.

A signal consisting of a single photon at frequency ν is detected with a signal to noise ratio (SNR) of

unity by the best possible receiver (Caves, 1982). In more conventional terminology, the quantum limit

of minimum detectable power is $h\nu B$, where B is the bandwidth in which the signal is detected; or the

quantum limit on the mixer noise temperature is $h\nu/k_B$ where k_B is Boltzmann's constant.

Heterodyne receivers based on SISs provide nearly quantum limited sensitivity for millimeter wavelengths (McGrath *et al.*, 1981; D'Addario, 1985; Face *et al.*, 1986; Face, 1987). They have served as practical radioastronomical receivers for many years, predominantly at Caltech's Owens Valley Radio Observatory (OVRO) (Woody, Miller, and Wengler, 1985; Sutton, 1983) and at AT&T Bell Labs' telescope at Crawford Hill (A. A. Stark and R. E. Miller, private communication). The development of SIS mixers and SIS mixer theory are reviewed by Tucker and Feldman (1985) and by Phillips and Woody (1982)

In this chapter, an introduction to SIS diodes and their interaction with radiation is given. The following subjects are introduced: the superconducting state, SIS diodes, classical and quantum theories for diode detection of radiation, and heterodyne detection.

In chapter 2, the quantum theory of heterodyne detection is presented. Most of the contents of chapter 2 have been published by Wengler and Woody (1987). Tucker's theory for SIS mixer gain is unchanged by the theory in chapter 2, but his theory for noise is augmented by an additional term due to radiation quantization. The theory of chapter 2 is constructed so that Caves' (1982) derivation of the quantum limit to receiver sensitivity applies directly. The full theory results in SIS mixers which do not violate the quantum limit on sensitivity. When this theory is applied to an ideal SIS, the mixer noise expressions are identical to those from the relatively simple theory for optical mixing in photodiodes. The theory can be viewed as a bridge between the low frequency classical radiation detection theories, in which light is treated as a wave, with the nearly classical theories of optical mixing, in which light is treated predominantly as a particle.

Chapter 3 presents a lot of numerical calculations from the quantum theory of mixing. Using this theory, the effects of various design parameters on mixer performance are investigated. The ultimate performance of various quality SISs under optimum conditions is investigated as a function of frequency.

Finally, Chapter 4 describes an SIS mixer which is extremely sensitive over much of the near-millimeter (100–1000 GHz) spectrum. The first results with this mixer have been described by Wengler *et al.*, (1985a & 1985b). The SIS in this mixer is integrated with a planar bowtie antenna, radiation is coupled to it through the quartz substrate on which the SIS-bowtie is fabricated. The bowtie antenna,

with bolometers instead of SISs, has been used for imaging arrays (Neikirk *et al.*, 1982). Planar antennas on dielectric substrates are extensively reviewed by Rutledge, Neikirk and Kasilingam (1984). Chapter 4 presents the latest results achieved with the bowtie-SIS mixer, both in the laboratory and on the telescope. Many of the design considerations for this mixer are discussed.

1.2 SIS Tunnel Junctions

The devices we use for radiation detection are tunnel junction diodes made from superconductors. Physically, they are a superconductor–insulator–superconductor (SIS) sandwich. The insulator presents a potential barrier, current is conducted by tunneling through the barrier from one superconducting electrode to the other. Barone and Paternò (1982) present a comprehensive introduction to tunneling between superconductors.

Superconductivity is a phenomenon of the electronic structure of a metal. An excellent introduction to superconductivity is given by Tinkham (1975). In a non-superconducting metal, the electrons behave as though they are a gas of independent particles. The ground state of the normal metal electron gas is most simply described as a Fermi sphere in momentum or k-space. All electronic states within a radius k_F are occupied, all outside are empty.

In metals, there is a small attractive force between electrons near the surface of the Fermi sphere. In superconductors, this attraction is strong enough so that bound pairs of electrons are formed at low enough temperatures. The resulting bound pair is a particle called a Cooper pair (Cooper, 1965). The Cooper pair has charge $-2e$, spin zero, and most importantly for the rich phenomena of superconductivity, it is a boson. In the superconducting state, the Cooper pairs experience a phenomenon called Bose condensation. These pairs all occupy the same minimum energy pair state, a phenomenon which is impossible for single, independent electrons since they are fermions. The nature of this pair state, and its ability to account for virtually every feature of superconductivity was first understood by Bardeen, Cooper and Schrieffer (1957). Their theory is widely cited simply as BCS theory. An informative introduction to this theory is given by Rickayzen (1969).

In the superconducting ground state, all of the electrons near the Fermi energy participate in the

Energy

Energy

E_F

Δ

k

E_F

Δ

Δ

Density of States
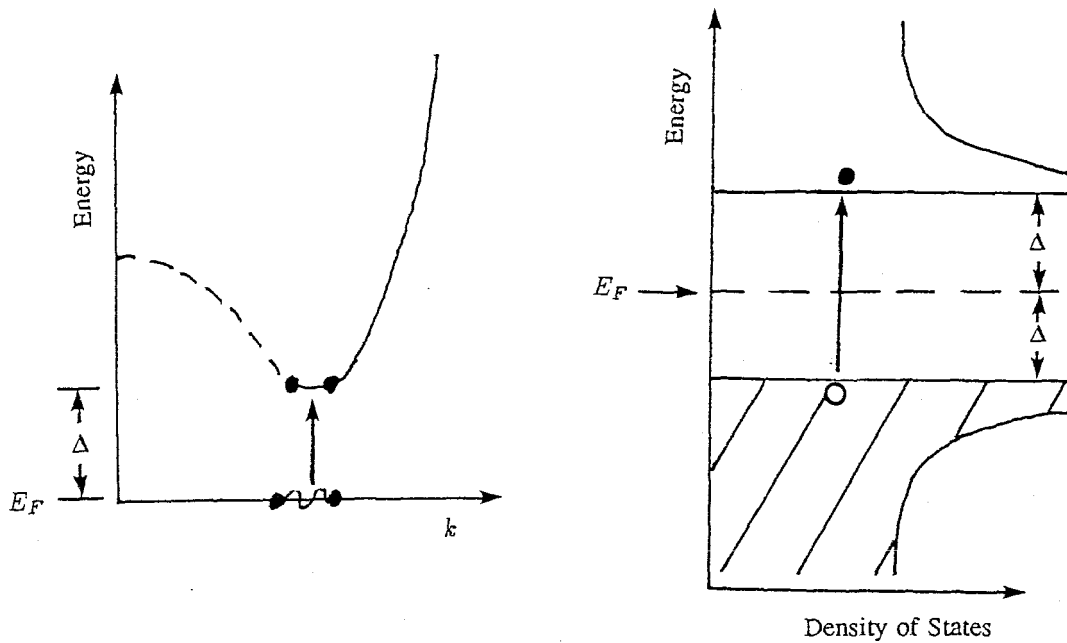
Figure 1.1 BCS superconductor electronic states. a) The pair states are all at the Fermi Energy. The quasiparticle excitation dispersion curve is shown with a broken pair occupying it (Barone and Paterno, 1982). The minimum quasiparticle excitation energy is Δ. b) In the semiconductor picture, the quasiparticle states are divided into a conduction-like and a valence-like band. A broken pair in this picture is represented by promoting a valence-like particle into the conduction band.

BCS pair state. The first excited state of a superconductor occurs when one Cooper pair is removed from the Bose condensate. There are no stable pair states above the BCS ground state, so the minimum energy procedure for removing a pair from the ground state is to break it. Each electron has a binding energy Δ to the Cooper pair. The minimum energy excitation above the ground state is therefore 2Δ, which is referred to as the superconducting energy gap, since any experiment to measure the gap must add Δ energy to two electrons at a time.

The breaking of a Cooper pair is analogous to the ionization of an atom. The electrons go from a single bound state into a continuum of free states, as shown in fig. 1.1a. The energy Δ corresponds to the ionization energy. The free electron states occupied by the electrons from a broken pair have a very odd energy vs. momentum dispersion relation due to the presence of the highly occupied BCS pair state. The "free" electrons are often referred to as quasiparticles, a term from Fermi-liquid theory. A quasiparticle is any particle which is found as the solution for an excited state of a system. In superconductors, the term "quasiparticle" refers to the single electron excitations resulting from breaking pairs.

The free electron excitation spectrum in a superconductor is highly analogous to the electronic density of states in a semiconductor, as shown in fig. 1.1b. The ground state of the superconductor is like the ground state of a semiconductor, the filled valence-like band and empty conduction-like band indicate the presence of no quasiparticle excitations. The first excited state of the system is described by the promotion of an electron from the top of the valence band to the bottom of the conduction band by giving it energy 2Δ. Two particles are created, a "hole-like" particle in the valence band, and an "electron-like" particle in the conduction band. Since this process is physically the result of breaking a bound pair of electrons, both the hole and the electron have the same charge $-e$. In this picture, the BCS pair state is analogous to the Fermi sea of electrons and positrons. The sea in a superconductor, however, has nothing but electrons in it, so pair creation produces two electrons.

The nature of the superconductor is such that there must always be equal numbers of electron-like and hole-like excitations. Thus the superconductor is always analogous to an intrinsic or pure semiconductor, and the electronic chemical potential energy μ must always lie exactly centered in the 2Δ energy gap. The presence of the BCS pair state in the superconductor can be schematically represented in this picture by a dashed line centered in the energy gap. With this representation, we are reminded that quasiparticle excitations occur by moving electrons Δ away from the pair state, and that when an electron in the conduction band falls into a $-e$ charged hole in the valence band, this really corresponds to the creation of a Cooper pair in the BCS ground state. The semiconductor picture can be used very successfully in understanding most of the quasiparticle effects in superconductors, especially those which describe radiation detection by SIS diodes. (This picture is not useful for understanding phenomena in which pairs are not broken. Those phenomena, including ac and dc Josephson currents, coherence lengths, penetration depths, parametric inductance, *etc.*, will go nearly unmentioned in this thesis, which is concerned with broken pairs only.)

We now discuss current conduction in an SIS tunnel diode. The SIS diode consists of a sandwich of two superconductors separated by a thin insulator, as shown in fig. 1.2a. The insulator is so thin, typically 10 to 20 Å, that the wavefunctions of electrons on either side have a significant overlap in the insulator. As a result, electrons and Cooper pairs can tunnel from one side of the barrier to the other.
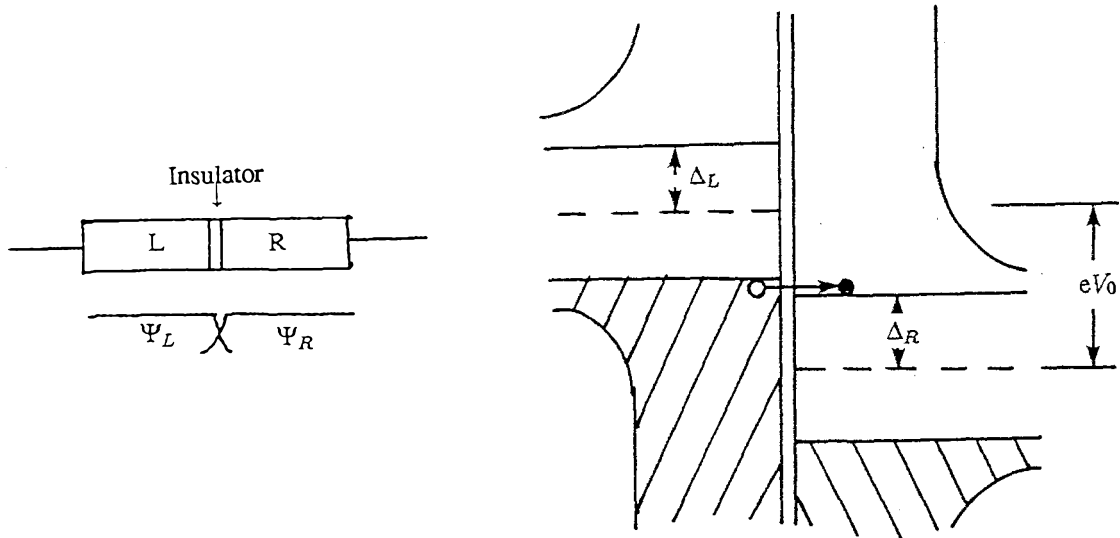
Figure 1.2 SIS tunnel junction. a) The diode consists of two superconductors, L and R, separated by a very thin insulator. Electronic wave functions, $\Psi_{(L,R)}$, overlap in the insulator. b) The semiconductor picture of an SIS, with a dc voltage V_0 applied, showing one quasiparticle tunneling.

Because the insulators typically present a $\sim .5$ eV barrier to electrons, tunneling is the only significant current source at the voltages (< 10 mV) and temperatures (< 5 K) at which the diodes are operated.

Figure 1.2b shows an energy level diagram for an SIS junction constructed by placing two semiconductor pictures back to back to represent "left" and "right" superconductors separated by a thin insulator. If there is no voltage applied across the SIS, the chemical potential for electrons in the left and right electrodes, μ_L and μ_R, are equal. If a dc voltage V_0 exists across the junction, the chemical potential of one side is shifted with respect to the other,

$$\mu_L = \mu_R + eV_0. \tag{1.2.1}$$

This is represented in fig. 1.2b by moving the diagram on the right side of the barrier up and down as V_0 is varied up and down.

The current through the junction is made up of electrons which tunnel from a filled state on one side of the barrier into an empty state on the other side of the barrier. If there is no interaction with another particle (such as a photon or a phonon), this electron transfer must conserve energy. Thus, an electron will only tunnel from the state it is in to an empty state on the other side of the barrier if these two states are at the same energy. The current-voltage (I-V) relationship predicted from the semiconductor

model assuming BCS ground state superconductors is shown in fig. 1.3a. A measured SIS I-V is shown in fig. 1.3b. When V_0 exceeds the gap voltage,

$$V_G = \frac{\Delta_L + \Delta_R}{e},$$

(1.2.2)

electrons at the top of the filled valence band on the left are able to tunnel into the empty conduction band states on the right. For all voltages $|V_0| < V_G$, there is no quasiparticle current.

The quasiparticle I-V predicted is nearly that of a perfect switch. Up to a voltage V_G no current flows through the SIS. At V_G, the current turns on suddenly, as it would in a perfect diode. Only a finite current can be supported at V_G, however, and above V_G, the I-V asymptotically approaches an ohmic relation. The asymptotic admittance value is labelled G_N. The I-V is antisymmetric, $I_{dc}(-V_0) = -I_{dc}(V_0)$.

A phenomenon know as the dc Josephson effect or supercurrent is also shown in fig. 1.3. This phenomenon is well reviewed in Brian Josephson's Ph. D. thesis, which has been published (Josephson, 1965). With no voltage applied across the junction, the BCS pair states are at the same energies on either side of the barrier. It is therefore possible for Cooper pairs to tunnel from one side of the barrier to the other. At finite V_0, the BCS pair states do not line up, and Cooper pairs can not tunnel.

When V_0 is finite, a Cooper pair will loose or gain energy $2eV_0$ in tunneling through the barrier. This tunneling can be mediated through interaction with, for instance, photons of the same energy, which would have a frequency

$$\nu_J = \frac{2e}{h} V_0$$

$$\frac{2e}{h} = 483.6 \frac{\text{GHz}}{\text{mV}} V_0.$$

(1.2.3)

Because there is only one macroscopically occupied BCS pair state on either side of the barrier, the potential for interaction with photons is accounted for by an ac supercurrent at frequency ν_J which flows across the junction. This current is referred to as the ac Josephson effect (Josephson, 1965). It can be observed indirectly by observing the effect of a microwave radiation field on the junction I-V, or directly by observing microwave radiation leaving the junction.

The detection mechanism considered in this thesis involves quasiparticle currents only. The Cooper pair currents do affect our detector experiments, but we try to operate our detectors so as to minimize
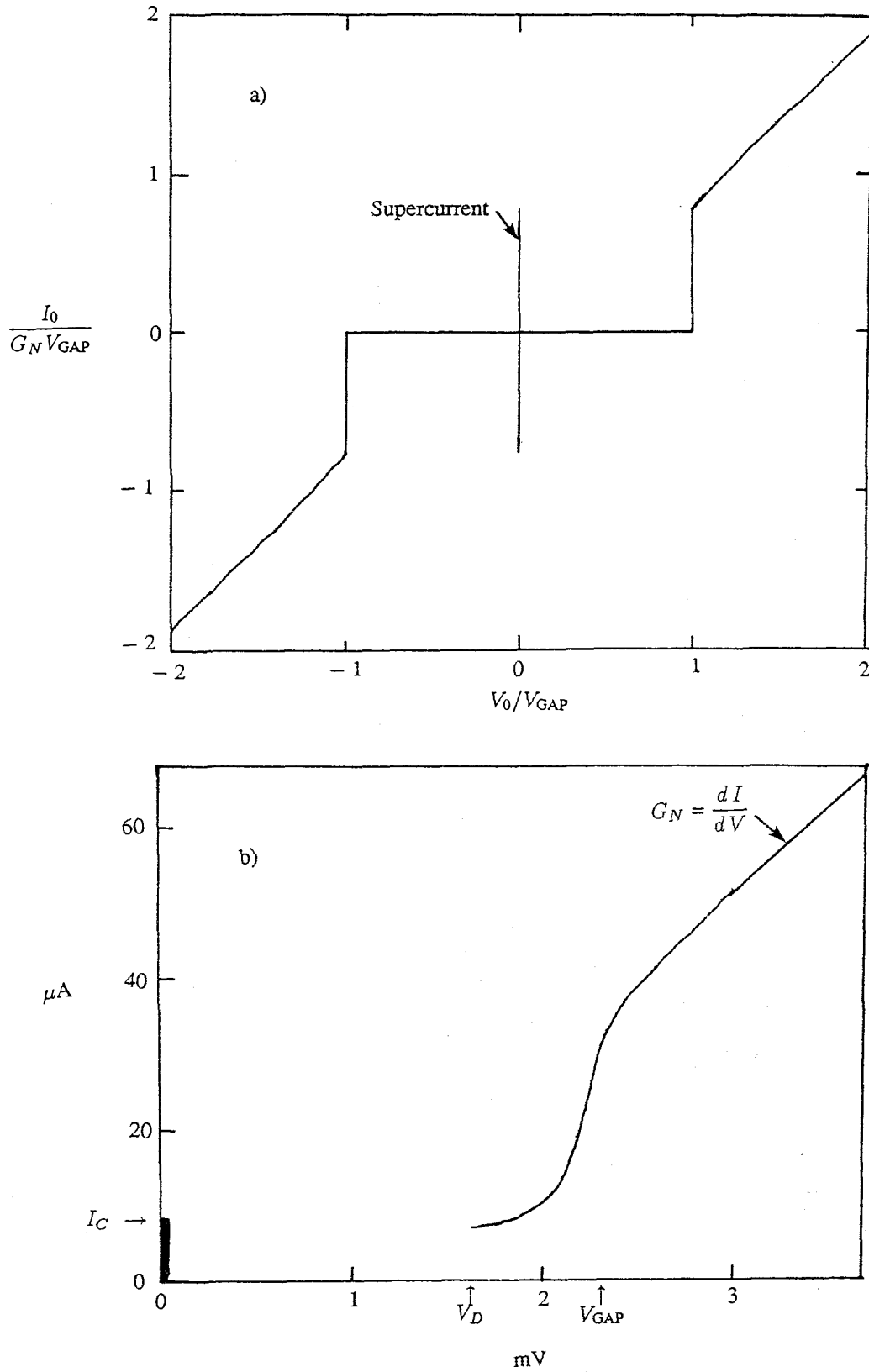
Figure 1.3 SIS dc I-V curve. a) The I-V calculated for an SIS at 0 K, using BCS theory. b) A measured I-V for an imperfect SIS at 4.5 K. Features such as the supercurrent, I_C, the gap voltage V_{GAP}, the normal state admittance G_N, and the dropback voltage V_D are shown.

their effect. We are also able to minimize these currents in some of our experiments through the application of a magnetic field to the SIS, as will be described in chapter 4.

1.3 Diode Response to Radiation: Classical Theory

We discuss the classical theory of radiation detection with resistive diodes (Torrey and Whitmer, 1948). A resistive diode is one in which the diode capacitance does not change significantly with voltage. We are not interested in a detailed theory of real diodes, so we assume a diode with no capacitance for this discussion. Our discussion is meant to give a simple point of reference on which to build the quantum theory of diode response to radiation. This classical diode is completely characterized by its current-voltage relationship (I-V) measured at dc, $I_{dc}(V_0)$.

We will use standard engineering convention for harmonic currents and voltages. Voltage and current waveforms at angular frequency ω are represented by complex valued voltage V_ω and current I_ω. The real time-varying waveforms associated with these complex phasors are

$$V(t) = \mathrm{Re}\ V_\omega e^{i\omega t}$$

$$I(t) = \mathrm{Re}\ I_\omega e^{i\omega t}.$$

(1.3.1)

An essential part of this convention is the use of complex valued admittances to relate voltage and current in linear elements. We will consistently use $\mathcal{Y}$ as our symbol for a complex admittance and we will use G and B as real numbers which represent the real and imaginary components respectively of $\mathcal{Y}$. So, at angular frequency ω we have

$$\mathcal{Y}_\omega = G_\omega + iB_\omega$$

$$I_\omega = \mathcal{Y}_\omega V_\omega$$

(1.3.2)

where I_ω is the complex current flowing through an admittance $\mathcal{Y}_\omega$ when the voltage across it is V_ω.

The general circuit we consider for calculating radiation detection is shown in fig. 1.4. The incident radiation has angular frequency ω_{LO}. (The subscript "LO" stands for Local Oscillator, anticipating the discussion of heterodyne detection in the next section.) The radiation source admittance is $\mathcal{Y}_{LO}$. A perfect current source $\mathrm{Re}\ \mathcal{I}_{LO} e^{i\omega_{LO} t}$ supplies the power incident on the diode. The dc circuit of the diode is assumed to be set up to provide a constant voltage bias, V_0.
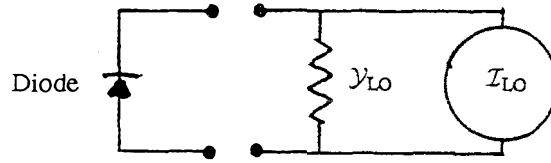
Figure 1.4 RF Circuit for a diode power detector. The power source is represented by an harmonic current source with angular frequency ω_{LO}, shunted by an admittance $\mathcal{Y}_{LO}$, which is called the source admittance.

In steady state, the current and voltage waveforms in the diode will be periodic with period $1/2\pi\omega_{LO}$.

In general, the current and voltage will have frequency components at dc, and at harmonics of ω_{LO}. For the sake of simplicity, assume that the external circuit presents a short to the diode at all frequencies above ω_{LO}. Then the voltage waveform across the diode is

$$V(t) = V_0 + V_1 \cos\omega_{LO}t. \tag{1.3.3}$$

In classical theory, the current waveform through the diode is simply related to its dc I-V,

$$I(t) = I_{dc}\left(V(t)\right). \tag{1.3.4}$$

The dc current through the junction is found by time averaging the current waveform,

$$I_0 = \int_0^{2\pi} \frac{d\phi}{2\pi} I_{dc}\left(V_0 + V_1 \cos\phi\right). \tag{1.3.5}$$

The current at the signal frequency is $I_1 \cos\omega_{LO}t$ where

$$I_1 = \int_0^{2\pi} \frac{d\phi}{\pi} I_{dc}\left(V_0 + V_1 \cos\phi\right)\cos\phi. \tag{1.3.6}$$

The diode presents an admittance to the incoming radiation which is

$$\mathcal{Y}_D = I_1/V_1 \tag{1.3.7}$$

A diode can be used as a radiation detector because the dc diode current I_0 changes as the amount of rf power absorbed in the diode changes. The rf power absorbed in the diode is

$$P_D = \text{Re}\,\frac{I_1^*V_1}{2} = \frac{G_D\,|V_1|^2}{2} = \frac{|V_1|^2}{2G_D}. \tag{1.3.8}$$
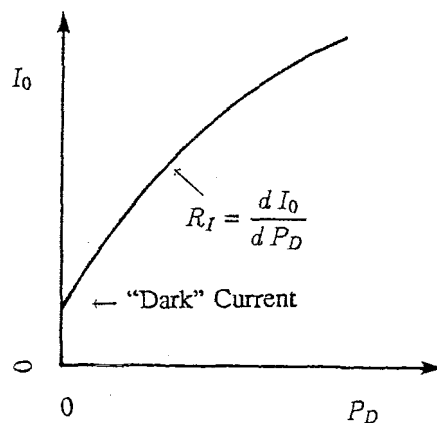
Figure 1.5 Photo-current response of a diode. At a constant dc voltage bias, the dc current through the diode is plotted as a function of the rf power absorbed in the diode. At low powers, the response is linear. The detection mechanism is rectification of the rf waveform.

The relation of I_0 to P_D can be found from (1.3.5) through (1.3.8), and typically looks like fig. 1.5. At any point along this curve, the current responsivity of the detector is defined,

$$R_I = \frac{d\,I_0}{d\,P_D}.$$ (1.3.9)

This describes the diode response to power it absorbs.

The power absorbed by the diode can be written in terms of the radiation source parameters. The maximum power available from the radiation source in fig. 1.4 is

$$P_{\mathrm{LO}} = \frac{|I_{\mathrm{LO}}|^2}{8G_{\mathrm{LO}}}.$$ (1.3.10)

The power absorbed in the diode is

$$P_D = \eta P_{\mathrm{LO}}$$ (1.3.11)

where η is the coupling efficiency between the source and the diode,

$$\eta = \frac{4G_{\mathrm{LO}}G_D}{|\mathcal{Y}_{\mathrm{LO}} + \mathcal{Y}_D|^2}.$$ (1.3.12)

It follows that a fraction $(1 - \eta)$ of the radiation incident on the diode from the radiation source is reflected from the diode. The diode current responsivity to *incident* power is ηR_I.

1.4 SIS Response to Radiation: Photon Assisted Tunneling

We now consider an SIS diode detector. Fig. 1.6a shows a family of dc I-V curves measured with three different levels of rf source power. fig. 1.6b shows the family of I-V curves that are expected from
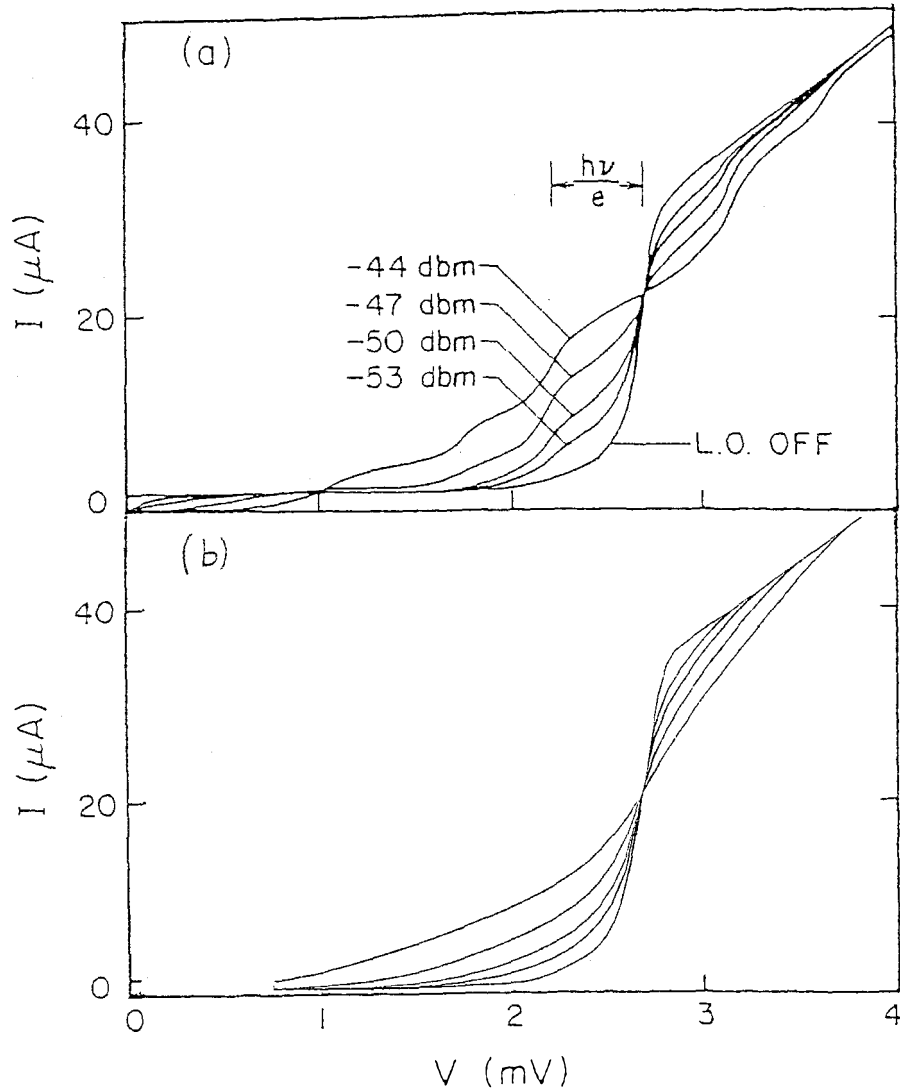
Figure 1.6 SIS *I-V*s with applied rf. a) The *I-V* measured with no rf and with four different rf power levels of 115 GHz radiation. Photon steps in the *I-V* are clearly seen. b) Predictions of the *I-V* with incident rf from the classical theory described in the previous section. Photon steps cannot be predicted with the classical theory.

the classical theory just described. The measured *I-V* curves show structure which the classical theory does not predict. Measurements at a large number of frequencies show that this structure is "photon steps" in the *I-V*, which occur at voltages $V_G \pm n V_\nu$ for small integer n, where

$$V_\nu = \frac{h}{e}\nu,$$

$$\frac{h}{e} = 4.13 \frac{\mu V}{GHz}.$$

(1.4.1)

These steps were first observed and explained by Dayem and Martin (1962). The voltage scale size of
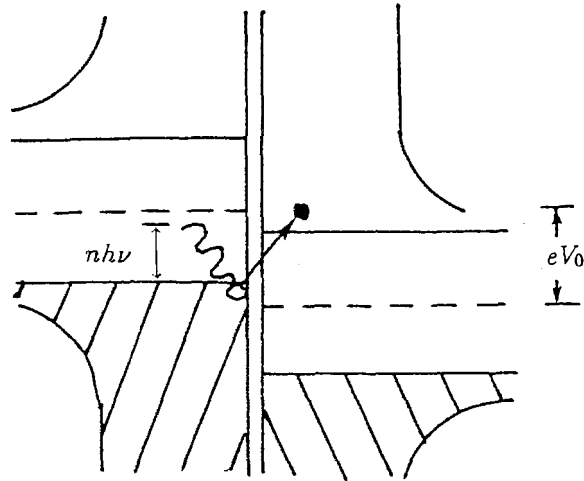
Figure 1.7 Photon-assisted-tunneling in an SIS. The simultaneous absorption of n photons can cause current to flow when $eV_0 + nh\nu > eV_{GAP}$.

the structures depends on the frequency of the radiation. It can be seen from (1.3.5) and (1.3.6) that classical theory I-V predictions do not depend at all on the frequency of the incident radiation, but only on its amplitude V_1.

The bumps are referred to as photon steps in the I-V curve. The conduction mechanism responsible for these steps is illustrated in fig. 1.7 using the semiconductor model of superconductivity. For a dc bias just below V_G, electrons at the top of the valence band on the lower voltage side of the barrier have a slightly lower energy than the empty electron states at the bottom of the conduction band on the other side of the barrier. If these electrons each absorb one photon from any incident radiation, their energy is raised by $h\nu$, which is enough to allow them to find empty states on the other side of the barrier. If the bias voltage is lowered to between $V_G - 2V_\nu < V_0 < V_G - V_\nu$, then each electron must absorb at least two photons from the radiation field in order to tunnel. The steps in the I-V occur as V_0 explores ranges in which a different number of photons must be absorbed to energetically allow electron tunneling.

A quantitative theory of photon assisted tunneling in SISs has been developed by Tucker (1979) from a tunneling Hamiltonian formalism (Bardeen, 1961; Cohen, Falicov and Phillips, 1962; Rogovin and Scalapino, 1974). The rest of this section is a slightly enhanced account of the development Tucker outlines in his paper.

As in the classical diode theory, the measured $I_{dc}(V_0)$ curve supplies all necessary information about the SIS diode. Currents are given in terms of a complex response function $j(x)$ which is an analytic

continuation of I_{dc},

$$j(x) = u(x) + iv(x)$$

$$v(x) = I_{dc}\left(\hbar x/e\right),$$

(1.4.2)

$$u(x) = \frac{1}{\pi}P\int_{-\infty}^{\infty}\frac{v(x')}{x'-x}dx'$$

where $P\int$ indicates that a Cauchy principal value is required since the integral will often be infinite. The real and imaginary parts of j are related through a Kramers-Kronig transform, and are both determined by a measurement of $I_{dc}(V_0)$. $v(x)$ is essentially the dc I-V curve, and it will appear in expressions for the components of current in the junction which are in phase with the voltage driving them. There will, however, be currents which are out of phase with the driving voltage, and the expressions for these will contain $u(x)$.

Tucker's theory starts with the two junction electrodes sufficiently separated that they are non-interacting. The Hamiltonian for the electronic state in the right side electrode is

$$H_R = \sum_q E_q c_q^\dagger c_q$$

(1.4.3)

where c_q is the creation operator for an electron in the q state and q ranges over all right electrode states. The energies E_q have their zero at the chemical potential μ_R for electrons in this electrode. With no voltage between them, the left electrode Hamiltonian would have a similar form. A voltage $V(t)$ between the two electrodes causes the chemical potential for electrons in the left electrode to be raised above that in the right electrode,

$$\mu_L = \mu_R + eV(t).$$

(1.4.4)

The left side electrode has Hamiltonian

$$H_L = \sum_k \left(E_k + eV(t)\right)c_k^\dagger c_k$$

(1.4.5)

where k ranges over all the states in the left electrode.

The voltage changes the energy of every electronic state in the left side electrode. For a Heisenberg picture operator $c_k(t)$, the electronic states are independent of time, so the time dependence of the operator must satisfy Schrödinger's equation. With no voltage applied, the creation operator is

$$c_k^0(t) = e^{-i\frac{E_k}{\hbar}t}c_k^0(0).$$

(1.4.6)

The effect of the ac voltage on the electronic creation operator is characterized by a voltage phase term

$$W(t) = \exp\left\{ -i\frac{e}{\hbar} \int^t dt' \left(V(t') - V_0 \right) \right\}$$ (1.4.7)

or its Fourier transform

$$W(\omega) = \int_{-\infty}^{\infty} \frac{dt}{2\pi} W(t) e^{i\omega t}.$$ (1.4.8)

The creation operator with applied voltage is related to the no voltage creation operator through

$$c_k(t) = c_k^0(t) \exp\left(-ieV_0 t/\hbar \right) W(t).$$ (1.4.9)

The two electrodes are now brought close enough together so that electronic states in each superconductor interact. This interaction is described by a tunneling Hamiltonian (Cohen, Falicov and Phillips, 1962)

$$H_T = \sum_{k,q} T_{kq} c_k^\dagger c_q + \sum_{k,q} T_{kq}^* c_q^\dagger c_k$$

$$= H_T^+ + H_T^-.$$ (1.4.10)

T_{kq} is the matrix element for tunneling from the k state on the left side to the q state on the right. H_T^+ contains terms which describe tunneling from right to left across the barrier, while the terms in H_T^- carry current in the other direction. The full Hamiltonian of the system is

$$H = H_R + H_L + H_T.$$ (1.4.11)

A current operator is found by calculating the time derivative of the right-side number operator (Cohen, Falicov and Phillips, 1962)

$$I' = e\frac{dN_R}{dt} = i\frac{e}{\hbar} \left[H, N_R \right]_-$$

$$= i\frac{e}{\hbar} \left(H_T^+ - H_T^- \right)$$ (1.4.12)

$$= I_+ - I_-$$

This operator does not contain the full time dependence of the current. The operators which it is made up of, c_k and c_q, are Heisenberg picture operators of the uncoupled Hamiltonian, $H_R + H_L$. The addition of coupling through H_T adds additional time dependences. The Heisenberg picture current operator, which contains all time dependences due to H, can be found approximately by treating the effect of

H_T to second order in perturbation theory. Because the current vanishes in the absence of H_T, standard linear response theory yields (Rogovin and Scalapino, 1974)

$$I(t) = -\frac{i}{\hbar} \int_{-\infty}^{t} dt' \left[I'(t), H(t') \right]_{-}.$$ (1.4.13)

The expectation value is taken over the unperturbed states of the electrodes to yield (Werthamer, 1966)

$$\langle I(t) \rangle = \text{Im} \int_{-\infty}^{\infty} d\omega' d\omega'' W(\omega') W^*(\omega'') e^{-i(\omega' - \omega'')t} j(\omega' + eV_0/\hbar).$$ (1.4.14)

For monochromatic radiation at angular frequency ω, $V(t)$, and therefore $W(t)$, are periodic with period $1/2\pi\omega$. $W(t)$ can be represented by a Fourier series

$$W(t) = \sum_{n=-\infty}^{\infty} W_n e^{-in\omega t}.$$ (1.4.15)

The quantum theory expressions for the currents flowing in the junction will depend on the value of j at a discrete set of values

$$j_n = j \left(eV_0/\hbar + n\hbar\omega \right) \qquad \text{for integer } n.$$ (1.4.16)

The expected current is also periodic. The dc current is

$$I_0 = \text{Im} \sum_{n=-\infty}^{\infty} W_n^* W_n j_n.$$ (1.4.17)

The ac current has frequency components

$$I_m = i \sum_{n=-\infty}^{\infty} W_{n+m}^* W_n (j_{n+m}^* - j_n) \qquad \text{for } m = 1, 2 \ldots$$ (1.4.18)

For the sinusoidal voltage $V(t) = V_0 + V_1 \cos(\omega t)$, W_n are real and

$$W_n = J_n(\alpha), \qquad \alpha = \frac{V_1}{\hbar\omega/e}$$ (1.4.19)

where J_n is the nth Bessel function of the first kind. If these values of W_n are used, then (1.4.17) and (1.4.18) are the quantum extensions of the classical diode theory equations (2.5) and (2.6). I_1 flowing at ω_{LO} is now represented by a complex current even for the pure real V_1 of (1.4.19). The admittance

$$Y_D = I_1/V_1$$ (1.4.20)

that the diode presents to the incoming radiation can have both dissipative (real) and reactive (imaginary) components. The quantum theory predicts a "quantum reactance" at high frequencies which has no classical analog.

A good quality SIS is a photodiode for microwave frequencies. The responsivity (2.2.9) of an SIS can be calculated for the voltage (1.4.19). Tucker (1979) shows that for an SIS biased with $V_G - \hbar\omega/e < V_0 < V_G$, the responsivity for small absorbed power is

$$R_I = \frac{e}{\hbar\omega}. \tag{1.4.21}$$

This is 2415 amps per watt for $\omega/2\pi = 100$ GHz. This responsivity corresponds to exactly one electron in the photo-current for each photon absorbed by the SIS. This is the characteristic responsivity of perfect photodiodes operated in the infrared and optical spectral range.

Tucker (1979) has determined that the quantum theory reduces to the classical theory when

$$\frac{I_{dc}(V_0 + \hbar\omega/e) - I_{dc}(V_0)}{\hbar\omega/e} = \frac{dI_{dc}(V_0)}{dV_0} \tag{1.4.22}$$

for all V_0. A quantized theory is affected by the detailed shape of the I-V on a voltage scale $\hbar\omega/e$. If the I-V is quite smooth on this voltage scale, then quantum theory predictions are identical to classical diode theory. The sharpest non-linearity of an SIS I-V is at V_G. For the I-V curves shown above, photon structure is clearly seen for 100 GHz photons. Good quality SISs made in other labs can have sharp enough non-linearities that photon structure is clearly seen for frequencies of just a few GHz.

1.5 Heterodyne Detection

Fig. 1.8 shows schematically what heterodyne detection involves. A signal at frequency ν_S and an LO (local oscillator) at frequency ν_{LO} are incident together on a radiation detector. The signal appears at the output of the mixer at a frequency $\nu_0 = |\nu_S - \nu_{LO}|$. The output is traditionally referred to as the IF (intermediate frequency). Mixers are more useful if their performance is linear,

$$P_0 = \mathcal{G}\left(P_S + P_N\right), \tag{1.5.1}$$
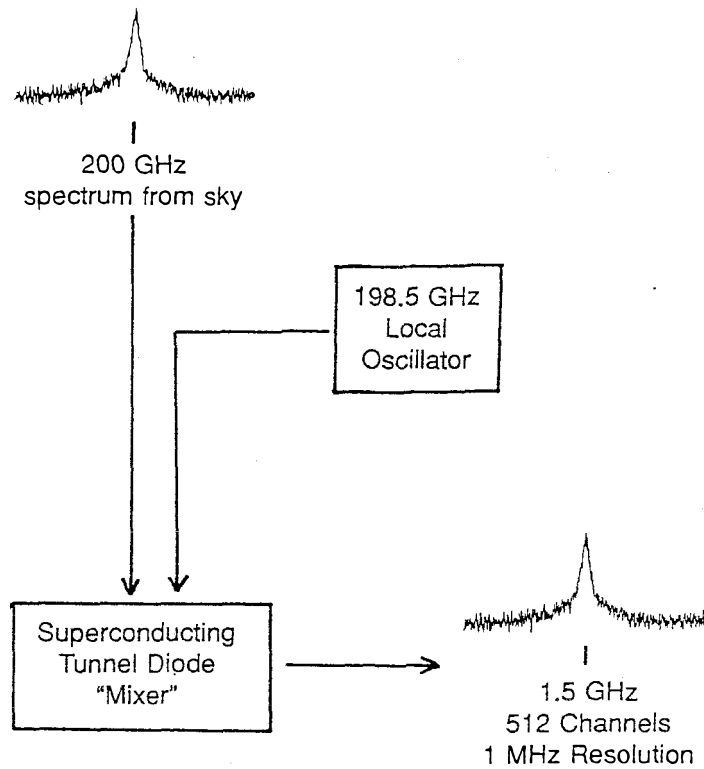
Figure 1.8 Heterodyne detection. Signal radiation at some high frequency ν_S is combined with a coherent oscillation at frequency $\nu_{LO} = |\nu_S - \nu_0|$. These are "mixed" by the detector diode so that the spectral information at ν_S is reproduced at the much lower frequency ν_0. This low frequency, or downconverted spectrum can be amplified and analyzed with (relatively) straightforward microwave components.

where P_0 is the mixer output power, P_S is the input signal power, $\mathcal{G}$ is called the gain of the mixer, and P_N is the noise power of the mixer referred to its input.

Heterodyne techniques are most useful when ν_S is too high to be processed with currently existing electronics. SIS mixers, as discussed in this thesis, are intended primarily for radioastronomy in the near-millimeter spectral range, $100 < \nu_S < 1000$ GHz. The output frequencies used in radioastronomy range as high as 5 GHz, and are more usually $1 < \nu_0 < 2$ GHz. These frequencies can then be processed with reasonably simple microwave electronics. For instance, the conceptually simplest processing would be to examine the IF on a commercially available 1-2 GHz spectrum analyzer.

The rf voltage across the radiation detector with LO and signal incident is

$$V_{rf}(t) = V_{LO} \cos \omega_{LO} t + v_S \cos \omega_S t \tag{1.5.2}$$

where $\omega_X = 2\pi\nu_X$ for all X. The rf power absorbed by the detector is

$$P_{rf} = G_D \left\langle V_{rf}^2(t) \right\rangle_T$$

$$= G_D \left(V_{LO}^2/2 + v_S^2/2 + v_S V_{LO} \cos \omega_0 t \right) \qquad (1.5.3)$$

$$= \eta \left(P_{LO} + P_S + 2\sqrt{P_S P_{LO}} \cos \omega_0 t \right)$$

where G_D is the real part of the admittance (1.3.7) presented by the detector to the incoming radiation, and η is the coupling efficiency (1.3.12) between the detector and the incoming radiation. The time-average is taken over a time T which is short compared to $1/\nu_0$, but long compared to $1/\nu_{LO}$, it serves to eliminate terms oscillating at $\sim 2\nu_{LO}$.

The current through the power detector will be $R_I P_{rf}$ where R_I is the current responsivity of the detector (1.3.9). This has dc terms due to P_{LO} and P_S, but there is also an oscillating current $i_0 \cos \omega_0 t$ with amplitude

$$i_0 = 2R_I \eta \sqrt{P_S P_{LO}}. \qquad (1.5.4)$$

If the diode presents an admittance G_{IF} at the output frequency, this current corresponds to an available IF power of

$$P_0 \left(\text{avail.} \right) = \frac{R_I^2 \eta^2 P_{LO}}{2G_0} P_S. \qquad (1.5.5)$$

Generally, R_I, G_D, G_{IF}, and η vary slowly with P_{rf}. If P_S is kept below some saturation power, then $P_{rf} \approx P_{LO}$ is constant, and (1.5.5) represents linear mixer response.

In general, signals incident on the mixer at all sideband frequencies $|\omega_m|$ are converted with some efficiency to power at the output frequency, ω_0. The sideband frequencies are

$$\omega_m = m\omega_{LO} + \omega_0 \qquad \text{for all integers } m. \qquad (1.5.6)$$

For the signal above, ω_S was either ω_1, called the upper sideband (USB), or it was $-\omega_{-1}$, called the lower sideband (LSB). For near-millimeter wave mixers, it is usually the case that $\omega_0 \ll \omega_{LO}$, which implies $-\omega_{-m} \approx \omega_m$. Many of these mixers respond equally well to signals in either the USB or the LSB. If signal is applied to such a mixer simultaneously in both these sidebands, the mixing is called double sideband (DSB).
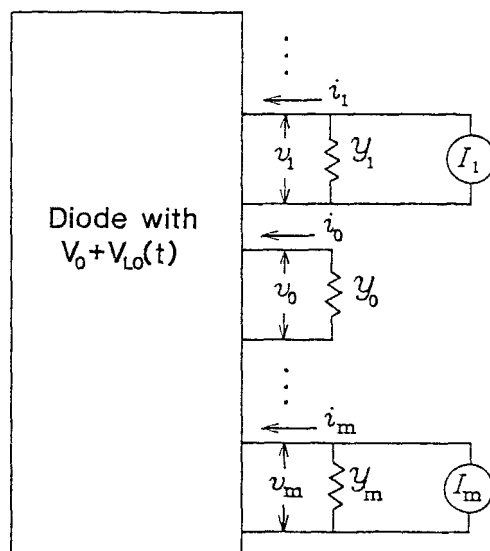
Figure 1.9 Schematic diagram of the equivalent circuit for a mixer diode heterodyne receiver. The LO pumped diode is represented by a multi-port linear network. Each port corresponds to a different sideband. The circuit to which the diode is attached is represented by an admittance $\mathcal{Y}_m$ at each sideband port. A current source $\mathcal{I}_m$ accounts for any noise or signal power incident on the diode at that frequency.

A full mixer analysis including all of the sidebands requires the Y-matrix formalism introduced by Torrey and Whitmer (1948). Tucker (1979) presents an excellent and compact explanation of this formalism.

The detector to be used in mixing is equated to some linear multi-port network. Fig. 1.9 shows how this identification is made. The mth port of this network corresponds to the ω_m sideband frequency of the mixer. When considered as a multi-port network, the fact that different ports m actually correspond to different frequencies is irrelevant. Results derived from linear network theory apply directly to linear mixer properties.

Sideband current phasors i_m, and voltage phasors v_m are linearly related through the Y-matrix,

$$i_m = \sum_{m'} Y_{mm'} v_{m'}$$

$$\vec{\imath} = Y \vec{v}$$

(1.5.7)

where a vector notation is used to represent the collection of sideband voltages and currents. The external admittances in fig. 1.9 can be described by a diagonal matrix of their values,

$$\mathcal{Y}_{mm'} = \mathcal{Y}_m \delta_{mm'}.$$

(1.5.8)

Letting the current generators $\mathcal{I}_m$ at the different mixer ports define a vector, the currents and voltages of fig 1.9 are linearly related,

$$\vec{\mathcal{I}} = \vec{i} + \mathcal{y}\vec{v}$$

$$= (Y + \mathcal{y})\,\vec{v}.$$

(1.5.9)

If the matrix

$$Z = (Y + \mathcal{y})^{-1}$$

(1.5.10)

exists, then the sideband voltages are linearly related to the sideband current generators driving the mixer,

$$\vec{v} = Z\vec{\mathcal{I}}.$$

(1.5.11)

The external admittance $\mathcal{y}_0$ usually represents the input impedance of an IF amplifier. The dependence of mixer performance on this value is found from network theory. Consider the network with all the terminating admittances $\mathcal{y}_m$ and current sources $\mathcal{I}_m$ attached to the network, except for those at the output port $m = 0$. The network is then a one-port linear network, and as such is described by a single admittance value shunting a single current source. Thus, the mixer's output port is a power source with some characteristic source admittance $\mathcal{y}_{\text{IF}} = G_{\text{IF}} + iB_{\text{IF}}$. If Z' denotes the Z matrix calculated with $\mathcal{y}_0 = 0$, then (Shen and Richards, 1981; Shen, 1980)

$$\mathcal{y}_{\text{IF}} = \frac{1}{Z'_{00}}.$$

(1.5.12)

Let us assume that the signal is in the USB, $m = 1$. A signal current source $\mathcal{I}_1 = \mathcal{I}_S$ corresponds to an available signal power of

$$P_S = |I_1|^2 / 8 G_1$$

(1.5.13)

where G_1 is the real part of the USB source admittance $\mathcal{y}_1$. The mixer output power is

$$P_0 = .5 G_0 |v_0|^2$$

$$= .5 G_0 |Z_{01}|^2 |\mathcal{I}_S|^2.$$

(1.5.14)

The gain, $\mathcal{G}$ in (1.5.1), of this mixer is

$$\mathcal{G}_{01} = P_0 / P_S$$

$$= 4 G_1 G_0 |Z_{01}|^2.$$

(1.5.15)

The decoration "01" is placed on $\mathcal{G}$ to indicate that this is the gain from the $m = 1$ to the $m = 0$ sideband.

This gain can be written as a product of a matched gain and an IF matching factor,

$$\mathcal{G}_{01} = \eta_{IF}\mathcal{G}_{01}^{M} \qquad (1.5.16)$$

where the matching factor is

$$\eta_{IF} = \frac{4G_{IF}G_0}{|\mathcal{Y}_{IF} + \mathcal{Y}_0|^2} \qquad (1.5.17)$$

and the matched gain is

$$\mathcal{G}_{01}^{M} = \frac{G_1}{G_{IF}}|\mathcal{Y}_{IF}Z'_{01}|^2 . \qquad (1.5.18)$$

The matched gain is independent of the output terminating admittance $\mathcal{Y}_0$, all dependence of mixer gain on $\mathcal{Y}_0$ is included through the matching factor, η_{IF}.

For G_0 and G_{IF} both greater than zero, η_{IF} has a maximum of unity, which occurs when the IF load admittance is conjugately matched to the mixer, $\mathcal{Y}_0 = \mathcal{Y}_{IF}^*$. Under this condition, $\mathcal{G}_{01}^{M}$ is the gain of the mixer, and any change in the value of $\mathcal{Y}_0$ results in a lower mixer gain. For SIS mixers, however, there are conditions under which G_{IF} is predicted to be less than zero. In this case, η_{IF} goes to infinity under a negative match condition, $\mathcal{Y}_0 = -\mathcal{Y}_{IF}$.

The determinant of the matrix $Y + \mathcal{Y}$ is zero under negative match condition,

$$\det(Y + \mathcal{Y}) = 0 \qquad \text{for } \mathcal{Y}_0 = -\mathcal{Y}_{IF}, \qquad (1.5.19)$$

and its inverse, Z (1.5.10), does not exist. Even near the negative match condition, all of the elements of the Z matrix are very large, since

$$\det Z = \frac{1}{\det Z^{-1}} = \frac{1}{\det(Y + \mathcal{Y})}. \qquad (1.5.20)$$

The procedure above for analyzing match to the mixer at the output port $m = 0$ can be applied to any port of the mixer. In general, the mixer presents some admittance $\mathcal{Y}_{Mm}$ at the mth port. The value of $\mathcal{Y}_{Mm}$ depends on the external admittances $\mathcal{Y}_{m'}$ for $m' \neq m$. The result of (1.5.19) generalizes to all ports, negative match at any port results in a singular $Y + \mathcal{Y}$ matrix. This means that if one port

ɔf the mixer is deliberately negatively matched, it will be found that all other ports are also negatively matched.

At the signal port $m = 1$, the signal power reflection coefficient is $|\Gamma_{11}|^2$. In terms of the admittance $\mathcal{Y}_{M1}$ that the mixer presents to the signal,

$$|\Gamma_{11}|^2 = \left| \frac{\mathcal{Y}_{M1}^* - \mathcal{Y}_1}{\mathcal{Y}_{M1} + \mathcal{Y}_1} \right|^2 . \tag{1.5.21}$$

For a negative match, this power reflection coefficient is infinity. A mixer operated with large gain due to approximate negative match at the output port will simultaneously have a very large reflection coefficient at the signal port.

Their are two important implications of this result. First, it is in principle possible to build a reflection amplifier using an SIS. This is probably some new sort of parametric amplifier, but no attempt is made in this thesis to analyze this amplifier. Second, a mixer operated with high gain at conditions near negative match at the output port will have reflection coefficients greater than unity from its signal port. Thus, it will be very difficult to design this mixer so that oscillations do not develop in the signal frequency circuit. As an oscillator, or perhaps as a very narrow band parametric amplifier, conditions near negative match are interesting. But for broadband mixer circuits, a successful use of negative match will require extremely careful design and circuit analysis to avoid unwanted oscillations and standing wave problems.

Like gain, mixer noise can also be described as a network phenomenon without reference to the fact that different network ports m are operating at different frequencies. To calculate this noise, we consider the network with no signals incident on it. The current sources $\mathcal{I}_m$ at each network port fully specify the noise in the linear network. The noise power coupled out of the mixer into $\mathcal{Y}_0$ is

$$
\begin{aligned}
P_{0N} &= G_0 \langle v_0^* v_0 \rangle \\
&= G_0 \sum_{mm'} Z_{0m} Z_{0m'}^* \langle \mathcal{I}_m \mathcal{I}_{m'}^* \rangle \\
&= G_0 B \sum_{mm'} Z_{0m} Z_{0m'}^* H_{mm'}
\end{aligned}
\tag{1.5.22}
$$

where the exact nature of the averages represented by $\langle \rangle$ are not specified until chapter 2. The noise properties are specified by calculating all possible noise current correlation products, which then define

the H matrix,

$$H_{mm'} = \frac{1}{B} \langle \mathcal{I}_m \mathcal{I}_{m'}^* \rangle .$$

(1.5.23)

B is the bandwidth in which the noise power is measured.

The mixer noise power referred to the input, P_N in (1.5.1), is found by dividing the noise power

at the output by the mixer gain. For an USB mixer, (1.5.15) gives the mixer gain, so

$$P_N = \frac{B}{4G_1 |Z_{01}|^2} \sum_{mm'} Z_{0m} Z_{0m'}^* H_{mm'} .$$

(1.5.24)

This can be divided by k_B and the measurement bandwidth B to give a mixer noise temperature,

$$T_{\text{MIX}} = \frac{P_N}{B k_B} .$$

(1.5.25)

The interested reader can verify that T_{MIX} is independent of y_0 (Shen and Richards, 1981).

1.6 Tucker's SIS Heterodyne Theory

Tucker (1979) derives analytical expressions for the Y and H matrices which describe an SIS

diode mixer, for the limit that the output frequency, ω_0, is small. As will be shown in chapter 2, his

expressions do not include all noise in the mixer. The H matrix he derives will be referred to as H_D

(for "diode") in this thesis.

Consider a voltage

$$V(t) = V_{\text{LO}}(t) + v_{\text{SIG}}(t)$$

(1.6.1)

across an SIS. The "signal" voltage is made up from the various sideband voltages,

$$v_{\text{SIG}}(t) = \text{Re} \sum_m v_m e^{i\omega_m t} .$$

(1.6.2)

$V_{\text{LO}}(t)$ is assumed to have its origin in a monochromatic local oscillator. It is periodic with period

$1/2\pi\omega_{\text{LO}}$ and has no components at any of the sideband frequencies.

Mixer response is calculated by considering v_{SIG} to be a small perturbation on V_{LO}, and then

calculating a Taylor-like expansion for the current $I(t)$ through the SIS. Using (1.4.14) and (1.4.7), $I(t)$

can be written as a functional of the voltage on the SIS,

$$I(t) = I \left[V_{\text{LO}}(t) \right] .$$

(1.6.3)

This can be Taylor expanded to linear order in v_{SIG},

$$I(t) = I\left[V_{\text{LO}}(t)\right] + \text{Re} \sum_{m'} Y_{mm'}\left[V_{\text{LO}}(t)\right] e^{i\omega_m t} v_{m'}$$

$$= I_{\text{LO}}(t) + i_{\text{SIG}}(t). \qquad (1.6.4)$$

$I_{\text{LO}}(t)$ is the response of the SIS to the LO voltage, and has no components at any of the sideband frequencies. Equations (1.4.15) thru (1.4.18) can be used to calculate I_{LO}. The signal current, i_{SIG}, contains components at all the sideband frequencies,

$$i_{\text{SIG}}(t) = \sum_m i_m e^{i\omega_m t}. \qquad (1.6.5)$$

The time dependence of the Taylor expansion coefficients is included explicitly in (1.6.4), so $Y_{mm'}\left[V_{\text{LO}}(t)\right]$ are time-independent. The sideband current components are related to the voltage components,

$$i_m = \sum_{m'} Y_{mm'} v_{m'}. \qquad (1.6.6)$$

where the Y matrix's functional dependence on V_{LO} is left unwritten for notational convenience.

Tucker (1979) calculates the Y matrix elements for the SIS. They depend on the Fourier series terms W_n (1.4.15), calculated for V_{LO}. Their dependence on the SIS response function (1.4.2) is through terms j_n (1.4.16), calculated for the dc bias voltage V_0, and the LO angular frequency ω_{LO}. They also depend on the first derivative of the response function through the terms

$$j_n' = \frac{\partial j\left(eV_0/\hbar + n\omega_{\text{LO}}\right)}{\partial V_0}. \qquad (1.6.7)$$

The Y matrix elements are (Tucker, 1979)

$$Y_{m0} = i \sum_{n=-\infty}^{\infty} W_{n+m}^* W_n \left(j_{n+m}'^* - j_n'\right) \qquad (1.6.8)$$

and for $m' \neq 0$

$$Y_{mm'} = \frac{ie}{2m'\hbar\omega} \sum_{n=-\infty}^{\infty} W_{n+\delta m}^* W_n \left(j_{n+m}^* - j_n - j_{n+\delta m}^* + j_{n-m'}\right) \qquad (1.6.9)$$

where $\delta m = m - m'$.

Tucker (1979) also presents expressions for an H matrix which describes noise generated in the SIS. His matrix does not describe all the noise in the mixer, as is discussed in chapter 2. The matrix he

derives is therefore referred to in this thesis as H_D, because it accounts for the part of the mixer noise which is algebraically attributed to the diode. Equation (1.5.22) is used to calculate the mixer noise. $\mathcal{I}_m$ in this expression represents a noise source from within the SIS. Essentially, it is the ω_m component of the operator $I(t)$ in (1.4.14), calculated assuming no signal voltage on the SIS. In chapter 2, the derivation is explained completely, but here, Tucker's result is merely restated,

$$H_{Dmm'} = e \sum_{n=-\infty}^{\infty} W_n W_{n+\delta m}^* \left(I_{n+m}^S + I_{n-m'}^S \right) \tag{1.6.10}$$

where

$$I_n^S = \coth \left(\frac{eV_0 + n\hbar\omega_{\mathrm{LO}}}{2k_B T} \right) I_{\mathrm{dc}} \left(V_0 + n\hbar\omega_{\mathrm{LO}}/e \right). \tag{1.6.11}$$

T is the physical temperature of the SIS. For $T = 0$, this expression is simpler,

$$I_n^S = \left| I_{\mathrm{dc}} \left(V_0 + \frac{n\hbar\omega}{e} \right) \right| \quad \text{for } T = 0. \tag{1.6.12}$$

Calculated for $T = 0$, the only noise mechanism contributing to the H_D matrix is shot-noise as electrons cross the tunnel barrier. For finite T, the H_D matrix also includes the contribution of Johnson, or thermal noise in the SIS current.

Chapter 2 – Quantum Heterodyne Theory

"I don't like it, and I'm sorry I ever had anything
to do with it."
— Erwin Schrödinger

2.1 Introduction

In this chapter, a complete quantum heterodyne theory for diode detectors is presented. This theory was developed to extend the quantum mixer theory for SISs developed by John R. Tucker (1979), which underestimates mixer noise. This theory can also be related to the general linear amplifier formalism of Carlton Caves (1982), and thus it is guaranteed not to underestimate mixer noise. The contents of this chapter are largely contained in a paper by Wengler and Woody, (1987).

The response of SIS diodes to radiation is manifestly quantum mechanical. Tucker's predictions of SIS mixer gain have been verified quantitatively (Phillips and Dolan, 1982; Feldman and Rudner, 1983; Feldman *et al.*, 1983). The development of SIS mixers and SIS mixer theory are reviewed by Tucker and Feldman (1985) and by Phillips and Woody (1982)

Quantum mechanics places limits on the sensitivity of a heterodyne system. A mixer which down-converts an input signal at some high input frequency to some much lower output frequency can be treated as a special case of a high gain linear amplifier. The general limitations placed by quantum mechanics on these systems have been discussed by many authors (Heffner, 1962; Caves, 1982; Shapiro and Wagner, 1984; Yamamoto and Haus, 1986). The quantum limit to sensitivity can be expressed as a minimum detectable signal power of $h\nu B$, where B is the bandwidth in which the signal is being measured. This is usually divided by B and Boltzmann's constant k_B to define a mixer "noise temperature". The quantum limit for T_{MIX} is $h\nu/k_B$.

The theory for noise in mixers developed by Tucker is incomplete. For good quality SISs, Tucker's theory predicts either no measurement noise, or half the quantum limit value, depending on how the mixer image is terminated. It has long been recognized that Tucker has somehow not included photon noise which might be coupled to the SIS. Many authors have solved this problem in an *ad hoc* way by assuming a noise source with available power $h\nu B/2$ to be coupled to the SIS at all of its sideband

frequencies (Hartfuß and Tutter, 1984; Tucker and Feldman, 1985; Danchi and Sutton, 1986; Feldman, 1986).

In this chapter, a general quantum mixer theory for two terminal devices is developed. Comparing this theory with Tucker's, it is apparent that Tucker has dealt with the SIS device in a completely correct fashion, but that he has failed to quantize the radiation incident on the SIS in his mixer theory. Combining Tucker's theory for the SIS device with the quantum mixer theory developed here, it is shown that an ideal SIS mixer has the same mixer noise properties as an ideal photodiode mixer. This theory is a bridge between radio detection theories, in which light is dealt with as a wave, and optical detection theories, in which light is dealt with as a particle.

The theory developed here is shown to be consistent with the general quantum formalism Caves (1982) uses in discussing linear linear amplifiers. It is thus shown that this quantum mixer theory cannot predict noises below the quantum limit value, since Caves uses his formalism to derive that value.

2.2 The Quantized External Circuit

Tucker's theory for the interaction of the SIS with radiation is not fully quantum mechanical. The voltage waveform $V(t)$ which appears in the SIS diode Hamiltonian, eqns. (1.4.3) through (1.4.11), is physically due to an electromagnetic field external to the diode. If that radiation field is quantized, then the voltage in (1.4.5) must be replaced by an operator.

Our theory of diode interaction with radiation considers only two modes of the radiation field, that mode which travels towards the diode guided by the diode's leads, and the similarly guided mode traveling away from the diode. The diode we use is, in principle, vanishingly small. In practice it is $\sim 1 \ \mu m$ while the wavelengths of radiation we consider are always $> 100 \ \mu m$. Just from these considerations it can be concluded that the diodes cross-section for interacting with unguided radiation is quite small. However, guided radiation can be made to occupy arbitrarily small linear dimensions. As such, diode response to radiation is completely dominated by the waves guided to and from the diode. This radiation is fully specified by the voltage across the diode and the current through the diode.

The natural circuit to describe the radiation field interacting with the diode is shown in fig. 2.1a.
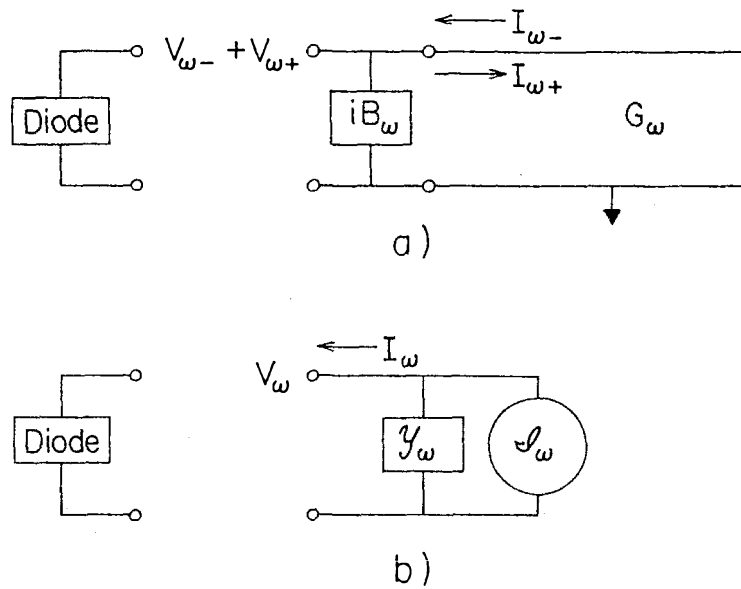
Figure 2.1 External circuit. a) The external circuit of the mixer is represented by a semi-infinite transmission line. Reactance from the external circuit appears as a lumped component at the line terminals. The direction of positive current flow for the − and + going waves are shown. b) An equivalent circuit which is usually used in mixer theories. A linear admittance shunted by a perfect current source models the circuit at each frequency.

No matter whether the diode is connected to an antenna, hanging across a waveguide, or in a stripline circuit, at the terminals of the diode the radiation guided to the diode is indistinguishable from radiation provided by the circuit of fig. 2.1a, if the values of the circuit elements are chosen properly. In this circuit, photons are carried towards and away from the diode by a lossless transmission line. Any reactance of the physical circuit attached to the diode is treated as a single lumped component placed at the terminals of the transmission line. The transmission line's characteristic admittance G_ω, and the reactive susceptance B_ω will have different values at different frequencies to correctly describe the actual circuit to which the diode is connected.

Before quantizing this circuit we present the conventions we will use for this development and throughout the rest of this thesis. As much as possible, we stay in the Heisenberg picture: quantum mechanical states are constant in time, time-evolution of an observable is completely determined by the time-evolution of the corresponding operator. This results in equations for voltage and current operators which are as similar as possible to the time evolution of their classical counterparts. Operators will often be given in terms of their frequency components. The ω frequency component $\widehat{W_\omega}(t)$ of an operator

$\widehat{W}(t)$ will be represented by a time independent "phasor" operator W_ω and its Hermitian conjugate $W_\omega^\dagger$. These operators for the same observable quantity are related through

$$\widehat{W}_\omega(t) = \tfrac{1}{2} \left(W_\omega e^{i\omega t} + W_\omega^\dagger e^{-i\omega t} \right).$$ (2.2.1)

A "hat" above any operator means that we want the time varying version of that operator, we will sometimes write $\widehat{W}(t)$ as $\widehat{W}$.

Quantization of the transmission line (Louisell, 1964) or of plane waves (Marcuse, 1980) requires consideration of a physically finite system. For the transmission line, the field is quantized in a length L of the line, and the voltage and current waveforms are assumed periodic along the line with period L. This periodicity results in a discrete set of allowed angular frequencies on the line,

$$\omega = n2\pi B \qquad \text{for} \quad n = 0, 1, 2 \ldots$$ (2.2.2)

where

$$B = c/L$$ (2.2.3)

and c is the speed of light on this transmission line. Usually, L is allowed, even forced, to go to infinity, and the allowed frequencies on the line take on the full continuum of values. Noise powers are typically proportional to the bandwidth over which they are measured. For theories in which the frequency does take on a continuum of values, it is necessary to integrate expressions involving operators and delta-functions in frequency over some finite frequency range to establish a finite bandwidth. The result is to prove that B in (2.2.3) can be interpreted as the bandwidth.

Because of this, we do not bring L to infinity in our theory. Angular frequency ω takes on discrete values, and the operator component W_ω is interpreted as being the operator for an angular frequency interval of width $b = 2\pi B$ centered on ω. Sufficient resolution for any physical problem can always be achieved by making L large, without having to resort to extending it through all the known universe and beyond. Time varying operators are then given as a sum (rather than an integral) over their frequency components,

$$\widehat{W}(t) = \sum_{n=0}^{\infty} \widehat{W}_{nb}(t).$$ (2.2.4)

All such operators are periodic in time with period $T = 1/B$. Measurements separated by a time interval T or longer can be looked at as independent experiments. The average value of these measurements is the expectation value $\langle \widehat{W} \rangle$ and the mean square noise is $\langle \widehat{W}^2 \rangle - \langle \widehat{W} \rangle^2$.

The voltage and current operators we use are equivalent to those found by Louisell's (1964) transmission line quantization. We quantize the incoming (−) and outgoing (+) travelling modes. All photon related operators expressed here have a spatial dependence along the transmission line which we do not write down, we are interested only in these operators at the terminals of the transmission line that connects to the diode in fig. 2.1. The Heisenberg photon creation operators for these modes are $\hat{a}_{\omega\alpha}^\dagger(t)$ where α takes on values + or −. Letting $a_{\omega\alpha}^\dagger$ represent the time independent or Schrödinger picture operator,

$$\hat{a}_{\omega\alpha}^\dagger(t) = a_{\omega\alpha}^\dagger e^{i\omega t} \tag{2.2.5}$$

shows the explicit time dependence of the Heisenberg operators.

In terms of phasor operators (2.2.1), voltage and current operators are

$$V_{\omega\alpha} = Q_\omega a_{\omega\alpha}^\dagger$$
$$I_{\omega\alpha} = G_\omega Q_\omega a_{\omega\alpha}^\dagger \tag{2.2.6}$$

where the "quantum of voltage"

$$Q_\omega = \sqrt{\frac{2\hbar\omega B}{G_\omega}} \tag{2.2.7}$$

is calculated from (2.2.3) and Louisell's eqn. (4.31). The current and voltage operators at the terminals including the effect of a lumped reactance iB_ω, are

$$V_\omega = V_{\omega-} + V_{\omega+}$$
$$I_\omega = I_{\omega-} - I_{\omega+} - iB_\omega V_\omega \tag{2.2.8}$$

Fig. 2.1b shows an equivalent circuit to fig. 2.1a which is usually used in mixer theory. The two circuits represent the same physical situation if the following relationships between them exist:

$$\langle I_{\omega-} \rangle = \mathcal{I}_\omega/2$$
$$\mathcal{Y}_\omega = G_\omega + iB_\omega \tag{2.2.9}$$

Voltage and current phasor operators are within a constant of the photon operators, just as electric and magnetic field operators are for free space modes. Their commutation relations are all within a

constant of the voltage operator commutators,

$$\left[V_{\omega\alpha}, V_{\omega'\alpha'}\right]_{-} = 0$$

$$\left[V_{\omega\alpha}^{\dagger}, V_{\omega'\alpha'}\right]_{-} = \frac{2\hbar\omega B}{G_{\omega}}\delta_{\omega,\omega'}\delta_{\alpha,\alpha'}.$$

(2.2.10)

The + and − modes are completely independent, their operators commute.

We find the power flux in each mode in terms of the voltage operators. The operator

$$\widehat{V}_{\omega\alpha}^{2}(t) = \frac{1}{4}\left[V_{\omega\alpha}^{2}e^{i2\omega t} + V_{\omega\alpha}^{\dagger 2}e^{-i2\omega t} + V_{\omega\alpha}V_{\omega\alpha}^{\dagger} + V_{\omega\alpha}^{\dagger}V_{\omega\alpha}\right]$$

(2.2.11)

will be used to define an instantaneous power flow operator. This operator has a time averaged expectation value

$$\left\langle \widehat{V}_{\omega\alpha}^{2}(t)\right\rangle_{t} = \frac{1}{4}\left\langle \left[V_{\omega\alpha}^{\dagger}, V_{\omega\alpha}\right]_{+}\right\rangle$$

(2.2.12)

where the subscript t indicates that an average over time $1/2\pi\omega$ is taken to remove terms at frequency 2ω. The average power flux in each mode is

$$P_{\omega\alpha} = G_{\omega}\left\langle \widehat{V}_{\omega\alpha}^{2}(t)\right\rangle_{t}$$

$$= \frac{G_{\omega}}{4}\left\langle \left[V_{\omega\alpha}^{\dagger}, V_{\omega\alpha}\right]_{+}\right\rangle$$

(2.2.13)

$$= \hbar\omega B\left(\langle n_{\omega\alpha}\rangle + \tfrac{1}{2}\right)$$

where

$$n_{\omega\alpha} = a_{\omega\alpha}^{\dagger}a_{\omega\alpha}$$

(2.2.14)

is the photon number operator for the mode. The anticommutator was simplified using the voltage commutation relation (2.2.10) and the definition of the voltage phasor (2.2.6). The quantum of radiation in traveling wave modes is $\hbar\omega B$ (Caves, 1982).

2.3 The Quantized Diode

A heterodyne mixer is made by connecting the terminals of a diode to the external circuit of fig. 2.1, which supplies signal, LO and dc bias and to which the output signal of the mixer is delivered. The approach taken is to separately quantize each half of this circuit, and to then attach them and require consistent solutions. For the purposes of this section, we label the photonic state of the external circuit

$|E\rangle$. The terminal voltage and current operators over this state are labeled $\widehat{V}_E(t)$ and $\widehat{I}_E(t)$. These operators could be explicitly constructed from (2.2.8) and (2.2.4).

In classical theory, each half of the mixer circuit has a current through it which depends on the voltage waveform across it. With the diode connected to the external circuit, the voltage across each, and the current flowing through each must be identical. The solutions of classical mixer theory are solutions of

$$I_D^{\mathrm{cl}}\left[V^{\mathrm{cl}}(t)\right] = I_E^{\mathrm{cl}}\left[V^{\mathrm{cl}}(t)\right] \tag{2.3.1}$$

where I_D^{cl} and I_E^{cl} give the current through the diode and the external circuit respectively as functionals of the voltage waveform. The square brackets in (2.3.1) are used to indicate that the current at any time is generally a functional of the voltage waveform, the current at time t may be functionally related to the voltage at all times t and earlier. A quantum generalization of the right half of (2.3.1) has been described in the previous section.

The quantum generalization of I_D^{cl} is much more complex than that for I_E^{cl}. For one thing, $|E\rangle$ can be factored into a product of independent states,

$$|E\rangle = \prod_{\omega,\alpha=\pm} |E\omega\alpha\rangle . \tag{2.3.2}$$

If a similar frequency factorization were possible for the mixer diode, then there would be no radiation detection, and no mixing! For another thing, the diode theory is really diode dependent. Whether the diode is constructed, for instance, from many layers of different semiconductors, or only a few layers of superconductors, should result in fundamentally different expressions for voltage operators in terms of electronic states operators.

What we present here is an outline of what a diode theory must include to be used in our mixer theory. Our paradigm for diode theories is Tucker's (1979) theory for tunnel junctions. Indeed, this is the only theory of a particular diode which is considered in this thesis. However, the outline here serves two purposes. First, it provides the theoretical framework for our view of the interaction of photons and electrons in circuits such as fig. 2.1. Second, it provides a point of view which will aid in the development of a diode theory for devices other than those Tucker considers.

We now turn to the task of quantizing the diode. By analogy to the external circuit notation, we label the electronic state of the diode by $|D\rangle$, and we define terminal voltage and current operators over $|D\rangle$, $\widehat{V}_D(t)$ and $\widehat{I}_D(t)$. When the diode and external circuit are connected at their terminals, $\widehat{V}_E$ and $\widehat{V}_D$ are distinct operators over disjoint sets of states, but for the same observable quantity. In fact, this applies to any observable function of these operators. For example,

$$\left\langle \widehat{V}_D^n(t) \right\rangle_D = \left\langle \widehat{V}_E^n(t) \right\rangle_E$$
$$\left\langle \widehat{I}_D^n(t) \right\rangle_D = \left\langle \widehat{I}_E^n(t) \right\rangle_E$$

(2.3.3)

for all integer n. The subscript E or D on the expectation value are meant to indicate that it is only necessary to evaluate this operator over the external photonic or diode electronic states respectively. The relationship of $|D\rangle$ and $|E\rangle$, which are by no means independent, is implicitly contained in (2.3.3). These relationships show that it is not necessary in an operator expression to indicate whether a voltage or current operator is over state $|D\rangle$ or $|E\rangle$.

We wish to create a quantum generalization for the left side of (2.3.1). We consider currents in the diode to be driven by voltages from the external circuit, so we will replace V^{cl} in (2.3.1) by $\widehat{V}$. The actual effect of the external circuit on the diode is to change its state $|D\rangle$. We can refer all such changes to the diode state when its leads are connected, i.e., its zero voltage state, which we label $|D0\rangle$. Then the state of the diode in contact with the external circuit is

$$|D\rangle = U\left[\widehat{V}(t)\right]|D0\rangle$$

(2.3.4)

where U is a unitary operator which is functionally dependent on voltage operators over the external circuit only. The quantum extension of the left side of (2.3.1) is then

$$\widehat{I}_{D0}(t) = \widehat{I}_{D0}\left[\widehat{V}(t)\right]$$

(2.3.5)

where this operator is related to the current operator on the left side of (2.3.3) by

$$\widehat{I}_{D0} = U^\dagger \widehat{I}_D U.$$

(2.3.6)

Expectation values of this operator are taken over the state $|D0\rangle$ even though the diode is not in this state with voltage applied. In this way, the junction current response is described as a functional of the external circuit voltage in a fully quantum fashion.

A heterodyne mixer has a large expected voltage on it due to the LO and dc bias, which we label $V_{LO}(t)$. The full voltage operator over the external circuit can be written as

$$\widehat{V}(t) = V_{LO}(t) + \widehat{v}(t). \tag{2.3.7}$$

The operator $\widehat{v}(t)$ will have small expectation values at all frequencies, since all the large voltages have been included in V_{LO}. It will only be necessary to keep terms in $\widehat{v}(t)$ to first order as a result.

We now consider how this field quantization modifies Tucker's theory. The voltage across the diode in his theory affects the diode through the voltage phase term (1.4.7). This is quantized by replacing the classical voltage term by $\widehat{V}(t)$ from (2.3.7). The voltage phase becomes an operator over photon states in the external circuit. It can be factored

$$\widehat{W}(t) = W\left[V_{LO}(t)\right]\ W\left[\widehat{v}(t)\right] = W_{LO}(t)W_v(t). \tag{2.3.8}$$

W_{LO}, which accounts for response to the large voltages, is unaltered from the classical term. The small voltage operator is a sum of its frequency components as described in (2.2.1) thru (2.2.4). From (2.2.10), it is seen that different frequency components of $\widehat{v}$ commute, so W_v can be factored,

$$W_v = \prod_\omega W\left[\widehat{v}_\omega(t)\right] = \prod_\omega W_{v\omega}(t). \tag{2.3.9}$$

Finally, we find $W_{v\omega}$ to linear order in voltage phase operators

$$W_{v\omega} = 1 - \frac{e}{\hbar\omega}\left(v_\omega e^{i\omega t} - v_\omega^\dagger e^{-i\omega t}\right). \tag{2.3.10}$$

2.4 Mixer Output Operator

In a mixer circuit, the voltage across the device is given by (2.3.8). The LO is from a coherent radiation source with fundamental angular frequency ω_{LO}, so $V_{LO}(t)$ has components at frequencies $m\omega_{LO}$ for positive integers m. (For notational convenience, we include any dc bias voltage in V_{LO}.) Input voltages at the sideband frequencies,

$$\omega_m = m\omega_{LO} + \omega_0 \qquad \text{for all integers } m, \tag{2.4.1}$$

are mixed together to produce the mixer output at frequency ω_0, as described in section 1.5.

Voltage and current operators have been previously defined for positive frequencies only, so

$$v_m = \begin{cases} V_{\omega_m}, & \text{for } \omega_m \geq 0; \\ V^\dagger_{-\omega_m} & \text{otherwise} \end{cases} \qquad (2.4.2)$$

are the sideband components of $\hat{v}$ in (2.3.7) where V_ω are the external circuit operators defined in (2.2.8). External circuit sideband current operators i_m are similarly defined, as are device current operators I_{D0m} for the components of (2.3.4). The external source admittances are

$$\mathcal{Y}_m = \begin{cases} \mathcal{Y}_{\omega_m}, & \text{for } \omega_m \geq 0; \\ \mathcal{Y}^*_{-\omega_m} & \text{otherwise.} \end{cases} \qquad (2.4.3)$$

Determining the mixer response is a matter of calculating the current operator in (2.3.4) as a function of the voltage operator in (2.3.8). Treating $\hat{v}$ as a perturbation on the device in the $U\left[V_{\text{LO}}\right]|D0\rangle$ state, the sideband current phasor operators are found as a first order perturbation

$$\begin{aligned} i_m &= I_{D0m}\left[V_{\text{LO}}(t)\right] + \sum_{m'} Y_{mm'}\left[V_{\text{LO}}(t)\right] v_{m'} \\ &= I_{\text{LO}m} + \sum_{m'} Y_{mm'} v_{m'}. \end{aligned} \qquad (2.4.4)$$

$I_{\text{LO}m}$ and $Y_{mm'}$ are operators over $|D0\rangle$ only, they do not operate on $|E\rangle$. Their functional dependence on V_{LO} is shown explicitly in (2.4.4), but will not be shown through the rest of this thesis. We need consider only the expectation value of $Y_{mm'}$, since the fluctuating component of $Y_{mm'}$ corresponds to gain fluctuations which are explicitly ignored in a linear theory (Caves, 1982). Without changing the symbol, we interpret $Y_{mm'}$ as an expectation value from here on.

Relating Tucker's tunnel junction device theory with our general notation, we have

$$I_{\text{LO}m} = 4\pi B I_T(-\omega_m) \qquad \text{for } T = 1/B \qquad (2.4.5)$$

where I_T is the current operator in Tucker's eqn. (7.9). This operator represents the sideband current flowing due to the LO voltage waveform. Its expectation value must be zero, since the expected current waveform must, like V_{LO}, have components only at ω_{LO} and its harmonics. Its fluctuations, however, have components at all frequencies.

The output voltage wave operator is found by comparing current operators in (2.4.4) and (2.2.9). In matrix and vector notation, (2.4.4) becomes

$$\vec{\imath} = \vec{I}_{\text{LO}} + Y\vec{v}. \tag{2.4.6}$$

The sideband current and voltage operators can be broken down into their $+$ and $-$ going components using (2.2.8). Rearranging terms

$$\left(\mathcal{Y} + Y\right)\vec{v}_+ = -\vec{I}_{\text{LO}} + \left(\mathcal{Y}^* - Y\right)\vec{v}_- \tag{2.4.7}$$

where $\mathcal{Y}_{mm'}$ is the diagonal matrix of $\mathcal{Y}_m$ values. In traditional mixer theory, the matrix $(\mathcal{Y} + Y)$ has an inverse matrix called Z, as discussed in section 1.5. We multiply both sides of (2.4.7) by this matrix

$$\vec{v}_+ = \Gamma\vec{v}_- - Z\vec{I}_{\text{LO}} \tag{2.4.8}$$

where

$$\Gamma = Z\left(\mathcal{Y}^* - Y\right)$$
$$= 2ZG - \mathbf{I}. \tag{2.4.9}$$

$\mathbf{I}$ is the identity matrix and the G matrix is the real part of $\mathcal{Y}$. Abandoning matrix notation, we have the output voltage operator

$$v_{0+} = \sum_m \left(\Gamma_{0m} v_{m-} - Z_{0m} I_{\text{LO}m}\right)$$
$$= -v_{0-} + \sum_m Z_{0m}\left(2G_m v_{m-} - I_{\text{LO}m}\right) \tag{2.4.10}$$

The output photon state $|E0+\rangle$ is implicitly determined by the states $|E-\rangle$ and $|D0\rangle$ by this equation, as one would expect from the causal chain described in section 2.3. This equation defines the output voltage wave at all frequencies except harmonics of the LO. Of course, the matrices and operators with subscripts m must be re-evaluated for each choice of ω_0 since m is a shorthand for $\omega_0 + m\omega_{\text{LO}}$.

The output power (2.2.13) of the mixer is

$$P_{0+} = \frac{G_0}{4}\left\langle \left[v_{0+}, v_{0+}^\dagger\right]_+ \right\rangle_{E+}. \tag{2.4.11}$$

Using (2.4.10), the expectation value of the anti-commutator can be evaluated over states $|D0\rangle$ and $|E-\rangle$,

$$\left\langle \left[v_{0+}, v_{0+}^\dagger\right]_+ \right\rangle_{E+} = \sum_{mm'} Z_{0m} Z_{0m'}^* \left\langle \left[I_{\text{LO}m}, I_{\text{LO}m'}^\dagger\right]_+ \right\rangle_{D0} + \sum_{mm'} \Gamma_{0m} \Gamma_{0m'}^* \left\langle \left[v_{m-}, v_{m'-}^\dagger\right]_+ \right\rangle_{E-}. \tag{2.4.12}$$

Cross terms are not written,

$$\left\langle \left[v_{m-}, I_{\text{LO}m'}^{\dagger} \right]_{+} \right\rangle_{E-,D0} = 2 \left\langle v_{m-} \right\rangle_{E-} \left\langle I_{\text{LO}m'}^{\dagger} \right\rangle_{D0} = 0 \qquad (2.4.13)$$

because $\left\langle I_{\text{LO}m'}^{\dagger} \right\rangle_{D0}$ is zero.

The first sum term in (2.4.12) accounts for output power which Tucker associates with noise in his mixer theory. To indicate that it accounts only for noise associated with the device operators, we label the current correlation matrix that Tucker calls H in his eqn. (7.14) H_D. Using (2.4.5) to calculate this in terms of our operators,

$$H_{Dmm'} = \frac{1}{4B} \left\langle \left[I_{\text{LO}m}, I_{\text{LO}m'}^{\dagger} \right]_{+} \right\rangle_{D0}. \qquad (2.4.14)$$

The second sum in (2.4.12) accounts for output power due to interaction with the incoming radiation. A current correlation matrix for the incoming radiation is

$$H_{Emm'} = \frac{G_m G_{m'}}{B} \left\langle \left[v_{m-}, v_{m'-}^{\dagger} \right]_{+} \right\rangle_{E-}$$

$$= \begin{cases} \frac{2 G_m G_{m'}}{B} \left\langle v_{m-} \right\rangle_{E-} \left\langle v_{m'-}^{\dagger} \right\rangle_{E-} & \text{for } m \neq m' \\ 4\hbar \omega_m G_m \left\langle n_{m-} + \frac{1}{2} \right\rangle_{E-} & \text{for } m = m'. \end{cases} \qquad (2.4.15)$$

The off-diagonal element $H_{Emm'}$ is non-zero only if the photon states $|Em-\rangle$ and $|Em'-\rangle$ are correlated. This occurs when, for instance, the radiation source is a parametric amplifier pumped with radiation which is phase-locked to the mixer LO (Caves, 1982). For most physical situations, H_E is diagonal and the mixer output power is

$$P_{0+} = G_0 B \sum_{mm'} Z_{0m} Z_{0m'}^{*} H_{Dmm'} + \sum_{m} \mathcal{G}_{0m} \left\langle n_{m-} + \frac{1}{2} \right\rangle \hbar \omega_m B. \qquad (2.4.16)$$

$\mathcal{G}_{0m}$ is the mixer conversion efficiency,

$$\mathcal{G}_{0m} = \frac{G_0}{G_m} \left| \Gamma_{0m} \right|^2 = \begin{cases} 4 G_0 G_m \left| Z_{0m} \right|^2 & \text{for } m \neq 0 \\ \left| 1 - 2 G_0 Z_{00} \right|^2 & \text{for } m = 0. \end{cases} \qquad (2.4.17)$$

We have made no attempt to describe the apparatus which measures P_{0+}. A photon counting power meter measures n_{ω_0} and detects $\hbar \omega_0 B / 2$ less than (2.2.13) predicts, while a classical power meter following a high gain linear amplifier would detect $\hbar \omega_0 B / 2$ more than our power expression. For the important special case that $\omega_0 \ll \omega_{\text{LO}}$, these differences are negligible, and (2.2.13) describes the

results of any type of power measurement accurately. For this case, our theory is a complete theory for heterodyne measurement. For larger output frequencies, the details of the output measuring system must be considered.

If ω_0 is small, we can also set P_{0-} to zero. Then the v_{0-} term in (2.4.10) does not contribute to the mixer output power, so (2.4.11) becomes

$$P_{0+} = G_0 B \sum_{mm'} Z_{0m} Z_{0m'}^* \left(H_{Dmm'} + H_{Emm'}\right) \qquad \text{for } P_{0-} = 0. \qquad (2.4.18)$$

Most of Tucker's expressions are derived under these assumptions. Tucker's mixer noise expressions involve sums like (2.4.18) over an H matrix which is equivalent to H_D. As we have defined H_E in (2.4.15), it accounts for mixer response to signal power, but as we show below, it also includes an additional noise term which completes tunnel junction mixer noise theory.

Eqn. (2.4.10) is close to the formalism used by Caves (1982) for consideration of lower limits on noise in amplifiers. Caves' eqn. (3.5) relates the output signal photon operator to input signal photon operators and a noise operator $\mathcal{F}_0$ through

$$a_{0+} = \sum_{m \in S} \left(M_{0m} a_{|\omega_m|-} + L_{0m} a_{|\omega_m|-}^\dagger\right) + \mathcal{F}_0 \qquad (2.4.19)$$

where S is the set of sidebands which carry signal. This is equivalent to (2.4.10) if

$$M_{0m} = \begin{cases} \sqrt{\frac{|\omega_m| G_0}{\omega_0 G_m}} \, \Gamma_{0m}^* & \text{for } \omega_m > 0 \\ 0 & \text{otherwise} \end{cases}$$

$$L_{0m} = \begin{cases} \sqrt{\frac{|\omega_m| G_0}{\omega_0 G_m}} \, \Gamma_{0m}^* & \text{for } \omega_m < 0 \\ 0 & \text{otherwise} \end{cases} \qquad (2.4.20)$$

$$\mathcal{F}_0 = \sum_m \sqrt{\frac{|\omega_m| G_0}{\omega_0 G_m}} \, Z_{0m}^* I_{LOm} + \sum_{m \notin S} \left(M_{0m} a_{|\omega_m|-} + L_{0m} a_{|\omega_m|-}^\dagger\right).$$

The Γ_{0m}^* for positive ω_m correspond to Caves' phase-preserving gain terms M_{0m}, while negative ω_m produce phase-conjugated gain L_{0m}. Caves refers to the modes which are summed over to produce $\mathcal{F}_0$ as internal modes. As he points out just before his conclusion, sideband modes which do not carry signal must be included with the noise-adding internal modes of the device.

Since our formalism is equivalent to Caves', it is consistent with the quantum limits he has derived for linear amplifiers. Although we are not going to pursue the interesting field of quantum non-demolition measurements in this paper, it is clear that (2.4.10) can be used to handle correlated photon input states (squeezed states) to heterodyne mixers.

2.5 Mixer Gain and Noise

In a classical theory, voltages can be measured instantaneously and exactly, so classical receiver theories use voltage and signal interchangeably. Quantum mechanically, the measurement of voltage is distinguished from voltage itself, so signal must be identified with the expectation value of the voltage waveform. The simplest use of a mixer is to determine the input voltage phasor in one sideband by measuring the output voltage phasor. For convenience we choose the $m = 1$ sideband to carry the signal. The input and output signals are

$$V_{\text{IN}} = \langle v_{1-} \rangle$$

$$V_{\text{OUT}} = \langle v_{0+} \rangle = \Gamma_{01} V_{\text{IN}}$$

(2.5.1)

where Γ_{01} in (2.4.10) is now identified as the voltage gain of the mixer. It is common to express mixer performance in terms of powers. The signal powers are

$$P_{\text{IN}} = \tfrac{1}{2} G_1 \, |V_{\text{IN}}|^2$$

$$P_{\text{OUT}} = \tfrac{1}{2} G_0 \, |V_{\text{OUT}}|^2$$

(2.5.2)

and they are linearly related by the conversion gain of the mixer (2.4.17)

$$P_{\text{OUT}} = \mathcal{G}_{01} P_{\text{IN}}.$$

(2.5.3)

Noise in the voltage measurement is characterized by the expected mean square deviation of a set of voltage measurements from the true expectation value. The voltage phasor operator is not an observable operator, so noise is calculated in the time domain using (2.2.13),

$$V_N^2 = \left\langle \left(\hat{v}_{0+}(t) - \langle \hat{v}_{0+}(t) \rangle \right)^2 \right\rangle$$

$$= \frac{1}{4} \left(\langle [v_{\omega+}, v_{\omega+}^\dagger]_+ \rangle - V_{\text{OUT}}^* V_{\text{OUT}} \right),$$

(2.5.4)

$$P_N = G_0 V_N^2$$

The minimum detectable signal power is defined to be the signal power which results in an output signal to noise ratio (SNR) of unity

$$P_{\text{det}} = P_N / \mathcal{G}_{01}. \tag{2.5.5}$$

The minimum detectable power is generally proportional to the bandwidth B, so the noise figure of merit for a mixer is a detectable noise power per bandwidth

$$E_M = P_{\text{det}} / B. \tag{2.5.6}$$

Traditionally, this is presented in units of temperature

$$T_M = E_M / k_B \tag{2.5.7}$$

but it can also be expressed in units of photons

$$N_M = E_M / \hbar\omega_1. \tag{2.5.8}$$

We now work out the noise for this measurement. Assume that the signal state $|E1-\rangle$ is an eigenstate of $v_{1-}^\dagger$ with eigenvalue V_{IN}. Since $v_{1-}^\dagger$ is proportional to a_{1-}, this eigenstate is a Glauber coherent state. This state carries power (2.2.13)

$$
\begin{aligned}
P_{1-} &= \frac{G_1}{4} \langle V_{\text{IN}} | \left[v_{1-}^\dagger, v_{1-} \right]_+ | V_{\text{IN}} \rangle \\
&= \frac{G_1}{2} \langle V_{\text{IN}} | v_{1-} v_{1-}^\dagger | V_{\text{IN}} \rangle + \hbar\omega_1 B / 2 \\
&= \frac{G_1}{2} | V_{\text{IN}} |^2 + \hbar\omega_1 B / 2 \\
&= P_{\text{IN}} + \hbar\omega_1 B / 2
\end{aligned}
\tag{2.5.9}
$$

where (2.2.11) was used to expand the anti-commutator. Comparison with (2.2.13) shows that photons counted by the number operator n_{1-} account exactly for signal power in this state, but power flux exceeds signal power by an unavoidable half photon which we attribute to the vacuum. To calculate minimum mixer noise, assume that all other incoming radiation states are in their vacuum states. Subtracting output signal power (2.5.3) from the total output power (2.4.16), we have the output noise power

$$P_N = G_0 B \sum_{mm'} Z_{0m} Z_{0m'}^* H_{Dmm'} + B \sum_m \mathcal{G}_{0m} \frac{1}{2} \hbar\omega_m. \tag{2.5.10}$$

The first term above is the noise term which Tucker derives for tunnel diode mixers. The second term is due to quantization of the external circuit, and it represents the minimum noise possible for the signal in one sideband only, since $\langle n_{m-} \rangle \geq 0$. For this mixer, the vacuum half photon at every sideband appears to be frequency converted into noise power at the mixer output.

The non-signal sidebands may be in thermal equilibrium photon states. The mth sideband photon state in thermal equilibrium at temperature T_m has

$$\langle v_m \rangle_{T_m} = 0$$

$$\langle n_{m-} + \tfrac{1}{2} \rangle_{T_m} = \tfrac{1}{2} \coth(\hbar \omega_m / 2 k_B T_m)$$

(2.5.11)

(Robinson, 1974) which has limiting forms

$$\langle n_{m-} + \tfrac{1}{2} \rangle = \begin{cases} \tfrac{1}{2} & \text{for } T_m = 0; \\ \frac{k_B T_m}{\hbar |\omega_m|} & \text{for } k_B T_m \gg \hbar |\omega_m|. \end{cases}$$

(2.5.12)

These limits are the vacuum state and the Rayleigh-Jeans limit, respectively. The noise in (2.5.10) represents the case that all unused sidebands are terminated at 0 K. We can include the effect of finite temperature termination of non-signal sidebands by replacing the $\tfrac{1}{2}$ in the second term on the right of (2.5.10) with the second line in (2.5.11).

Tucker suggests in his eqn. (7.8) that the Planck formula,

$$\langle n_{m-} \rangle_{T_m} = \frac{1}{\exp(\hbar \omega_m / k_B T_m) - 1},$$

(2.5.13)

be used to describe thermal noise. This is the traditional formula for the available photons, it does not include the unavailable one-half photon in (2.5.11) that is attributed to the vacuum. This relation between the Planck formula and (2.5.11) serves to emphasize the identification of the second term on the right of (2.5.10) as the quantum noise term. Amplifier gain and noise measurements are often made using black bodies at various known temperatures as calibrated power sources. Since one-half photon of (2.5.11) must always be identified with unavoidable noise, the Planck formula should be used to describe thermal "signals".

2.6 Photodiode Noise in SIS Mixers

We have developed the theory above very generally so it can serve as a framework for a quantum mixer theory of any device. The inclusion of the external circuit noise from H_E is not device dependent

at all, nor is the fact that the Y and Z matrices relate voltage and current operators in the external circuit. However, our formalism has been developed so that it will fit with the formalism developed by Tucker (1979) for SIS diodes, and complete the noise theory of these devices. We now show that this noise theory applied to perfect SIS mixers reduces to photodiode mixer theory.

In theory, a perfect SIS, dc biased just below its turn-on voltage V_G, has the responsivity of a perfect photodiode (Tucker, 1979). The SIS photo-current responsivity is $e/h\nu$, i.e., one electron joins the photo-current for each photon that is absorbed. It might be expected that the noise properties of such an SIS would be identical to the noise properties of a photodiode. Theories for the noise in mixers based on ideal photodiodes are described in textbooks by Kingston (1978) and Marcuse (1980).

For a perfect SIS operated at low LO powers, the expressions that Tucker gives for the Y and H_D matrices can be simplified, see for example Tucker and Feldman, (1985) and Feldman, (1986). The mixer noise (2.5.8) calculated for such an SIS, including the noise term H_E introduced in the previous section, is

$$N_M = 1/\eta \qquad (2.6.1)$$

where η has the form of a power coupling coefficient between two admittances,

$$\eta = \frac{4G_{\text{LO}}G_1}{|\mathcal{Y}_{\text{LO}} + \mathcal{Y}_1|^2}. \qquad (2.6.2)$$

$\mathcal{Y}_{\text{LO}}$ is the admittance presented by the SIS to the sinusoidal LO,

$$\mathcal{Y}_{\text{LO}} = \frac{I_{\text{LO}}}{V_{\text{LO}}}, \qquad (2.6.3)$$

I_{LO} can be calculated from Tucker's eqn. (5.2). $\mathcal{Y}_1$ is the signal source admittance. G_{LO} and G_1 are the real parts of $\mathcal{Y}_{\text{LO}}$ and $\mathcal{Y}_1$ respectively.

Note that the optimum source admittance is the admittance which the device presents to the LO and not the admittance it presents at the signal frequency. The load admittance which the SIS mixer presents to the input radiation at $m = 1$ can be calculated from the Y matrix and the terminating admittances $\mathcal{Y}_m$. In general, that admittance is *not* equal to $\mathcal{Y}_{\text{LO}}$, which is completely independent of all $\mathcal{Y}_m$. R. McGrath has suggested to us that the $m = 1$ mixer load admittance can be derived from an active circuit with a

feedback loop. $\mathcal{Y}_{LO}$ is apparently the passive admittance in this circuit. It is therefore this admittance to which Callen and Welton's (1951) fluctuation-dissipation theorem applies, and this admittance which the external circuit must match to minimize measurement noise.

This equation for mixer temperature is independent of image termination, $\mathcal{Y}_{-1}$. Consider the optimum mixer with $N_M = 1$ at $\mathcal{Y}_1 = \mathcal{Y}_{LO}^*$. If the image is also optimally coupled to the mixer, then $\mathcal{Y}_{-1} = \mathcal{Y}_{LO}$ and all of the mixer noise is algebraically due to the vacuum photon term on the right of (2.5.10). If, however, $\mathcal{Y}_{-1}$ is purely reactive, then half of N_M comes from the vacuum photons, and half comes from the device term involving H_D. We are seeing the detailed workings of the fluctuation-dissipation theorem. When the $\mathcal{Y}_{-1}$ is well coupled to the mixer, its dissipation enforces the quantum limit, but decoupling $\mathcal{Y}_{-1}$ from the mixer does not lower the quantum limit, instead dissipation in the device provides the necessary noise.

Equation (2.6.1) is the same as that obtained for a perfect photodiode. For photodiode mixers, η is defined as the fraction of radiation incident on the front of the photodiode which manages to get absorbed in the photodiode. Eqn. (2.6.2) is the circuit analog for this quantity. When (2.6.1) is derived for a photodiode mixer, it is calculated from the statistics associated with LO photon absorption. The fact that we derive this same amount of noise for an ideal SIS mixer leads us to conclude that, as in a photodiode mixer, noise in an ideal SIS mixer can ultimately be identified with the statistics of the photon absorption process. In fact, Devyatov *et al.*, (1986) provide expressions for SIS current which contain terms proportional to $a^\dagger a$ and $aa^\dagger$. We conclude that not only is an ideal SIS tunnel junction like a perfect photodiode in its response, producing one electron in its output current for each photon absorbed as Tucker has shown, but that it is like a perfect photodiode in its noise properties as well.

Real SIS mixers are not operated at low LO powers. At a higher LO power, SIS response to the LO saturates; not all absorbed photons result in the conduction of electrons across the device. While (2.6.1) is no longer exact for this case, we show that it is still a good approximation. Computer calculations of the mixer noise have been done for a nearly ideal SIS with the realistic values $V_{LO} = \hbar\omega_{LO} = eV_G$ and a variety of conditions on the image termination $\mathcal{Y}_{-1}$. This value of LO voltage represents more absorbed LO power than we typically find necessary in our actual mixers (Wengler *et al.*, 1985; Woody,
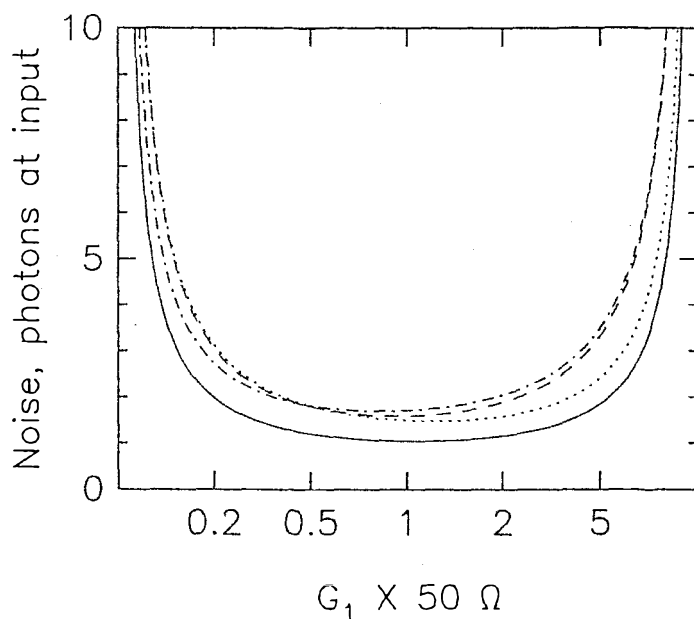
Figure 2.2 Mixer noise N_M vs. real source admittance G_1 for a nearly ideal SIS with large LO power. The a) dashed, b) dotted and c) dash-dot lines are for image termination equal to a) signal termination, b) open circuit, and c) short circuit. The solid line is a plot of (2.6.1) for comparison. The x-axis is the zero reactance slice through a standard Smith chart.

Miller and Wengler, 1985). These results are shown in fig. 2.2, along with a calculation of (2.6.1) for comparison. The image termination $\mathcal{Y}_{-1}$ slightly affects mixer noise for this high LO power, but simple photodiode theory still gives a good approximation to the mixer noise.

In this section, we have shown that the full noise theory for SIS mixers developed in previous sections is consistent with the conceptually simpler theory for noise in photodiode mixers. Since noise in photodiode mixers is completely derived from the statistics of the photon absorption process, we conclude that this is true for the ideal SIS mixer as well, even though the complex algebra of the full theory seems to obscure this relation. Finally, we have shown by calculations from the full noise theory, that photodiode theory describes, to reasonable accuracy, the noise in a good quality SIS mixer at realistic LO power levels. Of course, for poorer quality tunnel devices, noise sources other than photon noise are important, for these (2.5.10) from the full quantum mixer theory must be used to predict noise.

2.7 Summary

We have produced a fully quantum mixer theory which includes all noise effects in a heterodyne measurement. For the standard use of a mixer, we present expressions for mixer gain and noise. These

are derived from the expectation value of an output voltage operator and its square. Photodiode mixer theory is shown to be sufficient for describing noise in high quality SIS mixers. The operator formalism presented here can be easily extended to make predictions of SIS response to correlated photon states, which are the subject of much current research.

Our output operator expressions are similar to Caves' (1982), so his limits on amplifier performance should apply to any mixer analyzed with our theory. We have shown that, theoretically, SIS mixers can reach this limit. In fact, we have shown that for a good quality SIS, mixer noise is predicted by the simple expressions of photodiode mixer theory, and is simply related to how well radiation is coupled to the SIS.

Chapter 3 – Numerical Results from SIS Mixer Theory

"Looks an awful lot like a game of Empire to me."
— Jeff, in *Moby Mike* or *Captain Phillips and the Great White Wengler,* by Erich Grossman and Jeff Stern.

3.1 Introduction

Tucker's theory for mixing in tunnel diodes (Tucker, 1979), combined with the quantum heterodyne theory presented in chapter 2, lend themselves readily to use in computer programs. I have written an extensive set of such programs to aid in setting engineering specifications for SIS mixers, and to determine theoretical limits to SIS mixer performance. In this chapter, a brief outline of the information available from these programs is presented. Other numerical results from Tucker's theory have been published, (Danchi and Sutton, 1986; Devyatov *et al.,* 1986; Face, 1987; Feldman *et al.,* 1983; Feldman and Rudner, 1983; Hartfuß and Tutter, 1983 & 1984; Wengler and Woody in Phillips and Dolan, 1982; Phillips and Woody, 1982; Richards and Shen, 1980; Shen and Richards, 1981; Shen *et al.,* 1980). Many of these are reviewed by Tucker and Feldman (1985).

The engineering parameters considered here are 1) SIS junction quality, as measured by their *I-V* curves, 2) dc and LO bias 3) the admittances of the signal and image sources, $\mathcal{Y}_1$ and $\mathcal{Y}_{-1}$, and the IF load, $\mathcal{Y}_0$. The theoretical limits to SIS mixer performance are investigated by determining optimized mixer performance as a function of signal frequency, for four different tunnel diode *I-V* curves.

Mixer performance parameters are discussed in section 1.5. The mixing performance parameters presented in this chapter are mixer gain and mixer noise. Mixer input and output powers are related through

$$P_0 = \mathcal{G}\left(P_S + P_N\right) \tag{3.1.1}$$

where P_0 is the power coupled out of the mixer, P_S is the incident signal power, P_N is the mixer noise power referred to the mixer input, and $\mathcal{G}$ is the mixer gain. The gain reported in this section is the "available" gain, that which occurs for a properly matched IF amplifier. Mixer noise is reported in terms

of "mixer noise photons at the input,"

$$N_M = \frac{P_N}{h\nu_{LO}B}$$ (3.1.2)

where B is the bandwidth in which the mixer output signal is measured. This is related to the more usual "mixer input noise temperature" by

$$T_M = \frac{h\nu_{LO}}{k_B}N_M.$$ (3.1.3)

N_M, as described in chapter 3, has a quantum lower limit of unity for heterodyne detection. This quantum lower limit in terms of mixer noise temperature is $h\nu_{LO}/k_B$, which is 4.8 K at 100 GHz.

A complete receiver consists of a mixer followed by an IF amplification chain. Especially when the mixer gain is small, SNR is degraded because of noise in the IF amplifiers. As for the mixer, noise in the IF amplifier chain is characterized by its noise temperature referred to its input, T_{IF}. Total noise from the mixer and IF amplifier chain combination is also characterized by a receiver noise temperature,

$$T_R = T_M + \mathcal{G}^{-1}T_{IF}$$ (3.1.4)

From this relationship, it can be seen that high mixer gain is important insofar as T_{IF} is large. In the following sections, $\mathcal{G}$ and T_M are reported. For a given T_{IF}, the overall figure of merit, T_R, can be estimated from (3.1.4).

Until very recently, the state of the art for 500 MHz bandwidth amplifiers in the 1–2 GHz range was $T_{IF} \sim 10$ K, achieved with cooled GaAsFETs (Weinreb, Fenstermacher, and Harris, 1982). New transistors called HEMTs give early evidence of achieving $T_{IF} \sim 3$ K in this same range. Use of these amplifiers lower the importance of high mixer gain to overall receiver performance. Weinreb (1987) discusses a radically different approach to SIS-HEMT mixer-amplifier design.

3.2 Digitized *I-V* and Kronig-Kramers Transform

In his theory for SIS heterodyne response, Tucker (1979) considers current flow due to tunneling of quasiparticles, or single-electrons. Cooper pairs of electron can also tunnel, the currents due to this process are called Josephson currents (Josephson, 1965). For the mixer theory, the tunnel diode's

electronic structure is specified in terms of its complex response function, $j(x) = u(x) + iv(x)$, which is discussed in section 1.4. The portion of the device I-V which is due only to single-electron currents, $I_{dc}(V_0)$, fully specifies the imaginary part of j,

$$v(x) = I_{dc}(V_0) \qquad \left(x = eV_0/\hbar\right) . \tag{3.2.1}$$

The real part of j is related to v through a Kronig-Kramers transform (1.4.2).

For use in our programs, a measured $v(x)$ is treated as though it were piecewise linear between $M+1$ digitized points. For all devices that we consider, $v(-x) = -v(x)$ so it is only necessary to digitize the positive x side of v. Fig. 1.3b shows a measured SIS I-V curve with some of its interesting features noted. Most of the I-V is due to single electron currents, but the supercurrent, I_C, and the dropback voltage, V_D, are results of the interaction of the Josephson currents and the quasiparticle currents. The finite current I_C which flows with no dc voltage across the SIS consists of pairs. No quasiparticle current flows if there is no dc voltage, so $x_0 = v_0 = 0$ is the first digitized point for all SIS I-Vs. Stable bias is not possible for voltages between zero and V_D, due to chaos associated with ac Josephson currents. The second digitized point is $x_1 = eV_D/\hbar$, $v_1 = I_{dc}(V_D)$, and the quasiparticle I_{dc} is assumed linear between zero volts and this point. The SIS I-V asymptotically approaches an ohmic response, $I_{dc} \approx G_N V_0$, as V_0 gets large. We take a number of points $v_i = I_{dc}(V_{0i})$, $x_i = eV_{0i}/\hbar$ in ascending order, until $I_{dc}(V_{0M}) = G_N V_{0M}$ to within the accuracy which we care about. We then calculate slope, b_i, and intercept, a_i, for the straight line connecting (x_i, v_i) and (x_{i+1}, v_{i+1}). For voltages above V_{0M}, the ohmic values $b_M = \hbar G_N/e$ and $a_M = 0$ are used. The current at any positive $x = eV_0/\hbar$ is given by

$$I_{dc}(V_0) = \begin{cases} a_i + b_i x & \text{for } x_i \le x < x_{i+1} \\ b_M x & \text{for } x \ge x_M . \end{cases} \tag{3.2.2}$$

We refer to the collection of a_i and b_i as the "linefit" parameters of $v(x)$. We use linefit parameters to represent other curves in our programs.

To get the full complex response function $j(x)$ that corresponds to the measured I_{dc}, the Kronig-Kramers transform of $v(x)$ must be done numerically. From the relation (1.4.2), it can be seen that $I_{dc}(V_0) = -I_{dc}(-V_0)$ implies $j(x) = j^*(-x)$, and (1.4.2) can be rewritten as

$$u(x) = \frac{2}{\pi} P \int_0^\infty \frac{x'v(x')}{x'^2 - x^2} dx' . \tag{3.2.3}$$

All physical quantities in the mixer theory depend on differences $u(x_1) - u(x_0)$, or on $u'(x)$, so we can arbitrarily set $u(0) = 0$, in which case

$$u(x) = \frac{2}{\pi} \int_0^\infty \frac{x^2 v(x')}{x'(x'^2 - x^2)} dx'.$$ (3.2.4)

By setting $u(0) = 0$, we have made the integral finite when performed along the real axis, thus removing the requirement of taking a Cauchy principal value.

To evaluate this numerically, we write the integral as a sum over the linear bits of v. First we note that the transform of $v(x)$ is equal to the transform of $v(x) - b_M x$. This allows the elimination of the integral from x_M to $x = \infty$. The integral from 0 to x_M is the sum of its bits,

$$u(x_0) = \frac{1}{\pi} \sum_{i=0}^{M-1} a_i \ln \frac{(x_{i+1}^2 - x_0^2)x_i^2}{(x_i^2 - x_0^2)x_{i+1}^2} + (b_i - b_M) \ln \frac{(x_0 - x_{i+1})(x_0 + x_i)}{(x_0 + x_{i+1})(x_0 - x_i)}.$$ (3.2.5)

For each junction I_{dc}, we calculate this transform at 128 points and store its linefit parameters for use in further programs.

The first derivatives of u and v are used for finding elements of the Y matrix. We pretend that b_i is the value of v' halfway through the interval x_i to x_{i+1}. Linefit parameters for v' are then generated and stored for use by other programs. The same procedure is used on the linefit parameters of u'. Our avoidance of subtler splines for interpolation of the digitized data is made up for by our willingness to digitize many points wherever the curve has an interesting shape.

Each I_{dc} we digitize can be used for making mixer predictions. Through the years, we have built up a library of I_{dc} curves representing different quality junctions cooled to different physical temperatures. We store the linefit parameters for j and j' for each junction, and so any calculation we write a program for can be done for all these different sorts of junctions. In fig. 3.1 are shown I-V curves and their Kronig-Kramers transforms for four tunnel diodes. Table 3.1 summarizes some of the parameters of these junctions. The gap frequency,

$$\nu_{\text{GAP}} = \frac{e V_{\text{GAP}}}{h},$$ (3.2.6)

is a characteristic frequency for each junction. The current scales of these junctions have been scaled so that all four have $G_N = (50 \ \Omega)^{-1}$. Junction 1 is a PbBi alloy SIS cooled to 2.5 K (Dynes $et\ al.$,
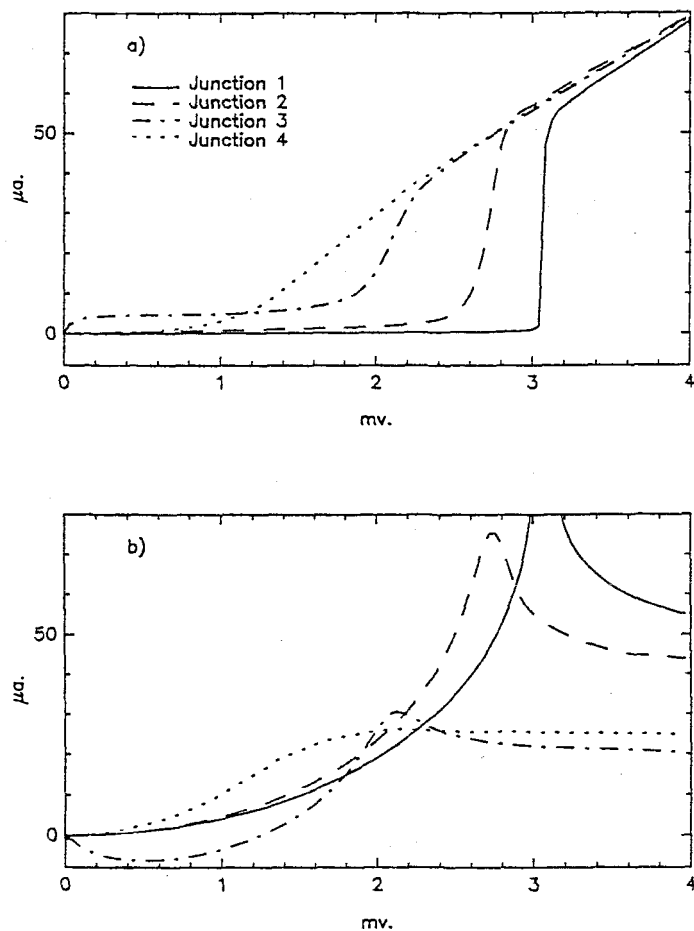
Figure 3.1 Complex response function, j, for four tunnel diodes. a) Im j is the measured I-V of each diode. b) Re j is the numerically determined Kronig-Kramers transform of Im j.

1978). Its I-V is nearly ideal in the sense that their is virtually no current flowing below V_{GAP}, and the current turns on very suddenly at V_{GAP}. Junction 2 is also cooled to around 2.5 K. It is a PbInAu alloy SIS that was used in early mixer experiments at Caltech. Junction 3 is also a PbInAu alloy SIS, cooled to 4.5 K. This junction is the one used for the first bowtie mixer experiments (Wengler et al., 1985), which are also discussed in chapter 4 of this thesis. Finally, junction 4 is a lead SIN tunnel junction cooled to 1.6 K (Giaever, 1960). An SIN is a superconductor-insulator-normal metal tunnel diode. Its I-V is much less non-linear than the SIS curves. SINs have been proposed for receivers because there is no Josephson effect in them, the Josephson effect is responsible for excess noise in some SIS mixers (Tucker and Feldman, 1985).

Mixer results for these four junctions are presented below. The three SIS I-Vs cover the full range of quality for which mixing experiments are reported. Hence, the effect of I-V quality can be determined

Table 3.1 – Junction data for Figure 3.1

Junction	V_{GAP}, mV	ν_{GAP}, GHz	Physical Temperature, K
1 (SIS)	3.06	740.	2.5
2 (SIS)	2.70	653.	2.5
3 (SIS)	2.13	516.	4.5
4 (SIN)	1.75	423.	1.6

from the results below. The inclusion of the SIN curve in calculations shows what performance must be sacrificed if these are used in mixers instead of SISs.

3.3 Assumptions for Numerical Calculations

A number of assumptions are made so that numerical calculations of mixer performance can be carried out. These assumptions are collected here, and the conditions under which they are valid are discussed.

For the mixer we investigate the IF or output frequency ω_0 is assumed small enough to be treated classically. Tucker (1979) presents the criterion that frequencies $\omega_0 < \delta x$ can be treated classically, where δx is the smallest x-axis scale on which the complex response function, $j(x)$, has structure. The output frequencies typically used with SIS heterodyne receivers for radioastronomy are 1 to 2 GHz. All of the I-Vs shown in fig. 3.1 are smooth on the voltage scale, about 8 μV, which corresponds to 2 GHz, so all the calculations presented in this chapter are valid for astronomical heterodyne receivers.

For a mixer, the LO is physically due to a monochromatic power source at frequency $\nu_{LO} = \omega_{LO}/2\pi$. We assume this results in a sinusoidal voltage $V_{LO} \cos \omega_{LO} t$ across the device. For this voltage, the W_n (1.4.19) are real, and

$$W_n = J_n(\alpha) \qquad \text{for } \alpha = \frac{eV_{LO}}{\hbar \omega_{LO}} \tag{3.3.1}$$

where J_n are Bessel functions of the first kind. A more general theory would allow for the possibility of harmonic generation at the device by including harmonic components $V_m \cos\left(m\omega_{LO} t + \phi_m\right)$ for $m \geq 2$ in the LO waveform. These will be small in SIS millimeter wave mixers for two reasons. First, the junction capacitance will tend to short out these high frequency harmonics. Second, as usually operated, an SIS mixer does not have much harmonic content in its LO waveform. As will be seen below, $\alpha \leq 1$

for efficient fundamental mixing in a good quality tunnel junction. Using (1.4.18) for $\alpha = 1$, the second harmonic current is about one-fifth the amplitude of the fundamental LO frequency current, $I_2 \approx .2I_1$. Unless it is deliberately arranged to be otherwise, the circuit to which the junction is connected presents similar admittances $|\mathcal{Y}_2| \sim |\mathcal{Y}_1|$ at the LO fundamental and first harmonic. The harmonic voltage is then $|V_2| \sim .2 |V_{LO}|$, and $|V_2|$ is even smaller if junction capacitance is taken into account. If the harmonic voltage is treated as an LO voltage, it corresponds to a a Bessel function argument $\alpha_2 = eV_2/\hbar 2\omega_{LO} \gtrsim .1$. A value of α_2 this small means that V_2 corresponds to less than one-fifth the optimum LO voltage, or less than 4% of the optimum LO power for mixing at $2\omega_{LO}$. The effects of this low harmonic content should be negligible by comparison to effects from the LO fundamental.

All mixer calculations are done using 3 by 3 matrices for Y, Z, and H_D. Equations for these matrices were developed by Tucker (1979), and are reviewed in section 1.6 of this thesis. The elements used are the central nine,

$$(Y, Z, H_D)_{mm'} \qquad \text{for } m, m' = -1, 0, 1, \qquad (3.3.2)$$

which relate voltages and currents at the signal, image and output frequencies. Matrix elements outside these central nine describe mixing between harmonics of the LO and the higher order sidebands, ω_m (1.5.6) for $|m| \geq 2$. Harmonic mixing calculations will depend strongly on harmonic content of the LO voltage waveform. The assumption made above that there is no harmonic content is therefore consistent with the use of only the central 3 by 3 terms from the Y, Z, and H_D matrices.

The expressions for currents, (1.4.18), and for the mixer matrix elements, (1.6.8) thru (1.6.10), involve summations over an infinite number of terms. For the numerical calculations discussed below, these summations are made finite by assuming

$$W_n = J_n(\alpha) = 0 \qquad \text{for } |n| > 50. \qquad (3.3.3)$$

The high order Bessel functions are given approximately by

$$J_n \approx \frac{\alpha^n}{n!} \qquad \text{for } \alpha \ll n. \qquad (3.3.4)$$

As examples, $J_{50}(10) \sim 10^{-15}$ and $J_{50}(1) \sim 10^{-65}$. The lower order Bessel functions are, by comparison, of order unity for this range of α. Very little is lost by terminating summations at $|n| = 50$.

The calculations presented here are made assuming the ambient temperature of the junction is 0 K in (1.6.11), so that (1.6.12) is used for I_n^S. A finite temperature in (1.6.11) allows the inclusion of Johnson noise in the predicted mixer noise. Using $T = 0$ K means we calculate only shot noise. The highest temperature at which the SIS mixers we describe are operated is less than 5 K. Voltage bias values are typically ~ 2 mV. For $V_0 = 1.5$ mV and $T = 5$ K, the coth term in (1.6.11) is equal to 1.06, while for $T = 0$ K it is equal to 1. This implies that Johnson noise accounts for at most a few percent of the noise in SIS mixers, the rest is the shot noise, which we calculate.

Many of the calculations presented will be for the so-called double-sideband (DSB) mixer. This refers to the condition that the external circuit presents the same admittance to the mixer at both the signal and image frequencies. This is achieved by requiring

$$\mathcal{Y}_1 = \mathcal{Y}_{-1}^*. \tag{3.3.5}$$

The complex conjugation is necessary because of the definitions of $\mathcal{Y}_m$ in (2.4.3). Under this condition, the conversion efficiencies for the signal and image are the same, $\mathcal{G}_{01} = \mathcal{G}_{0-1}$, hence the name double-sideband. The physical motivation for condition (3.3.5) is that the signal and image frequencies usually differ by only a few percent. Thus a circuit with a $Q \lesssim 10$ will present very similar admittances at these two frequencies. Mixers like the bowtie mixer described in chapter 4 almost certainly satisfy (3.3.5). However, it is often the case for waveguide based mixers that different conversion efficiencies are measured for the different sidebands. We present some calculations for non-DSB mixers which may be relevant to these experiments.

3.4 Performance vs. dc and LO Bias

The dc bias voltage V_0 and the LO voltage amplitude V_{LO} are referred to collectively as the voltage bias. Mixer gain and noise are calculated numerically as a function of the voltage bias to determine the best bias for an SIS mixer.

In fig. 3.2 are shown calculations of conversion gain vs. bias voltage for three situations. Calculations of mixer noise show the same structure as the gain, and so they are not shown. Fig. 3.2a shows the calculation for the nearly ideal I-V of junction 1 shown in fig. 3.2, assuming that it is being operated
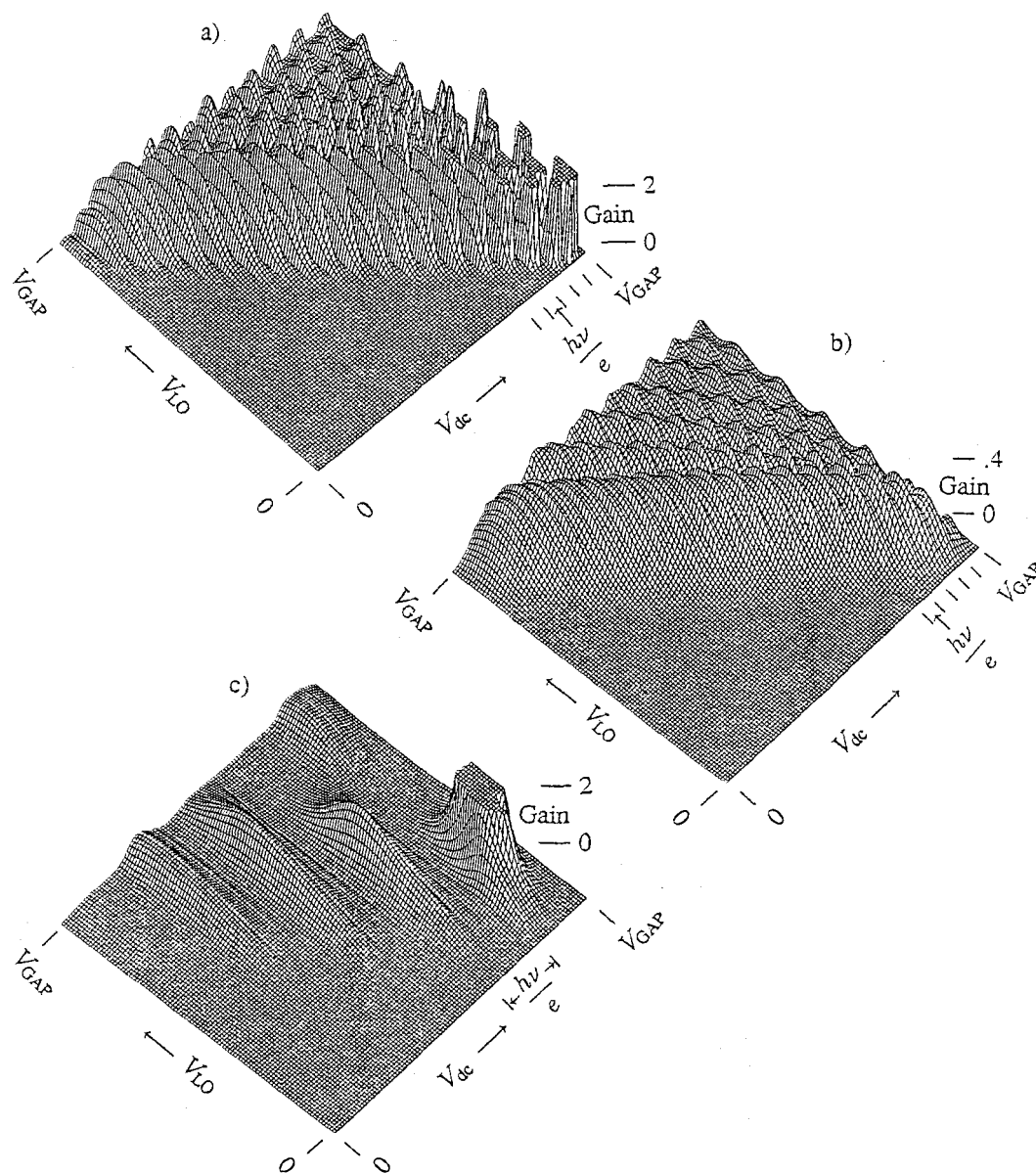
Figure 3.2 Conversion gain vs. dc and LO voltage bias. a) Junction 1 from fig. 3.1 operated at frequency .025ν_{GAP} = 37 GHz. Gain is clipped at 2. b) Junction 2 operated at frequency .025ν_{GAP} = 32.6 GHz. The gain scale in this case is 5 times lower than for a) or c). c) Junction 2 at a higher frequency, .1ν_{GAP} = 130.5 GHz. Gain is clipped at 2.

at a frequency .025ν_{GAP} = 37 GHz. Fig. 3.2b shows results for junction 2 with the same normalized frequency of .025ν_{GAP}, which corresponds to 32.6 GHz because V_{GAP} is lower for this junction. Finally, fig. 3.2c shows results for junction 2 at a higher frequency, .1ν_{GAP} = 130.5 GHz.

Figs. 3.2a and c show definite photon structure in the mixer response. In each of these cases, peaks

of conversion efficiency fall at dc bias voltages near the middle of each photon step,

$$V_0 \approx V_{\text{GAP}} - \left(n + \tfrac{1}{2}\right) \frac{\hbar \omega_{\text{LO}}}{e} \qquad \text{for } n = 0, 1, 2 \ldots \qquad (3.4.1)$$

These plots also show the presence of high conversion gains at dc voltages near to V_{GAP}. In this figure, conversion efficiencies greater than 2 are plotted as equal to 2. The flat-topped regions in these two plots actually include regions of infinite conversion efficiency, a non-classical phenomenon discussed above.

A comparison of figs. 3.2a and b shows the effect of I-V curve sharpness on mixer conversion efficiency. The photon steps which are so obvious in a are barely discernible as a slight ripple in conversion efficiency in b. The weaker I-V non-linearity limits the maximum conversion efficiency in b to .37, as compared to an infinite gain prediction for a.

For calculations of the gain vs. (V_0, V_{LO}), a mixer with external signal and image admittances $\mathcal{Y}_1 = \mathcal{Y}_{-1} = G_N$ is assumed. The IF load admittance is chosen to maximize mixer conversion efficiency as discussed above. Calculations made assuming other values for $\mathcal{Y}_1$ and $\mathcal{Y}_{-1}$ show essentially the same results described above. Therefore, the best bias point (V_0, V_{LO}) can be considered to be independent of the external circuit admittances chosen.

3.5 Performance vs. Signal and Image Source Admittance

The behavior of an SIS mixer as the external circuit admittance is varied is now determined. For this calculation, a junction at a particular bias point and frequency is characterized by its Y and H_D matrices. Calculations of mixer gain and noise, and receiver noise are calculated as $\mathcal{Y}_1$ and/or $\mathcal{Y}_{-1}^*$ are varied, results are presented on a Smith chart normalized to G_N. The optimum operating point, found as described above, is held constant for this calculation. Whichever of $\mathcal{Y}_1$ or $\mathcal{Y}_{-1}^*$ represents the signal sideband source admittance is labeled $\mathcal{Y}_S$, and the other, which is then the source admittance of the image sideband, is labelled $\mathcal{Y}_I$. For the low output frequency limit which is assumed here, results are mathematically identical whether the signal is in the upper or lower sideband.

Calculations of mixer noise expressed in photons, N_M (2.5.8), vs. $\mathcal{Y}_S$ in the DSB case are shown in fig. 3.3. These results are at the optimum operating point for junction 1 at $f = .1\nu_{\text{GAP}}$ corresponding
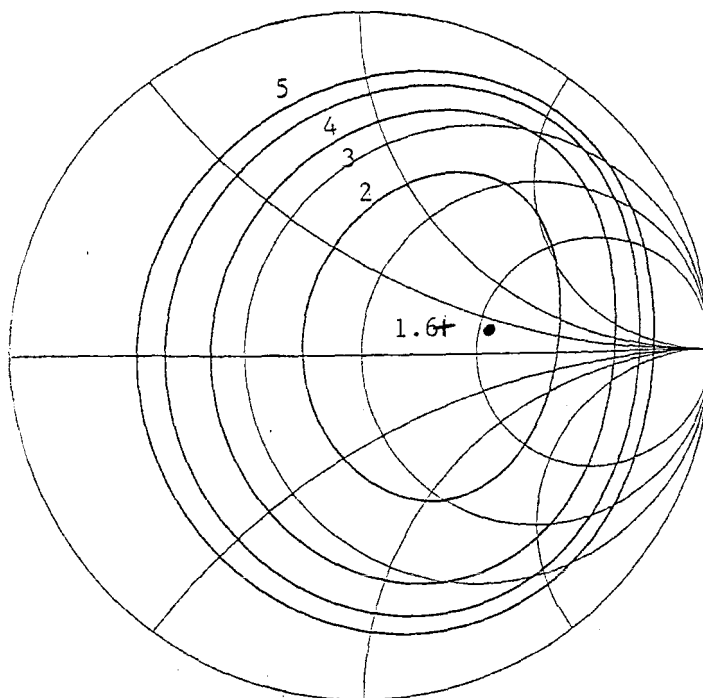
Figure 3.3 Mixer noise vs. $\mathcal{Y}_S$. Mixer noise is shown as contours of constant N_M. The calculations are done for junction 2 at frequency $.1\nu_{GAP} = 130.5$ GHz, assuming $\mathcal{Y}_S = \mathcal{Y}_I$. Minimum N_M is shown with a +, Y_{LO} is shown with a •.

to fig. 3.2b. N_M is minimum for $\mathcal{Y}_S \approx Y_{LO}$, consistent with the results presented in section 2.6. This minimum is fairly broad, a significant area of the Smith chart results in $N_M < 2$.

Mixer conversion gain, shown in fig. 3.4, varies in a way which is quite different from the mixer temperature. For most situations examined with these programs, infinite gain is available for values of $\mathcal{Y}_S$ which appear in the lower left half of the Smith chart. This corresponds to source admittances with a small to zero real conductance (high real impedance), and a small negative imaginary conductance. (A negative imaginary conductance corresponds to inductance, positive imaginary conductance corresponds to capacitance.)

The available gain from the mixer vs. $\mathcal{Y}_S$ is dominated by the change in the output admittance, G_{IF}, that the SIS mixer presents to the following IF amplifiers. Fig. 3.5 shows how G_{IF} varies with $\mathcal{Y}_S$. Especially at higher gain, the contours of constant gain are seen to be nearly parallel to the contours of constant G_{IF}. Infinite gain is available for $G_{IF} \leq 0$ as discussed in section 1.5.

Given this effect, it would seem that an SIS mixer should be designed to have an output admittance which is in the neighborhood of zero mhos, and a following amplifier with as high an input admittance,
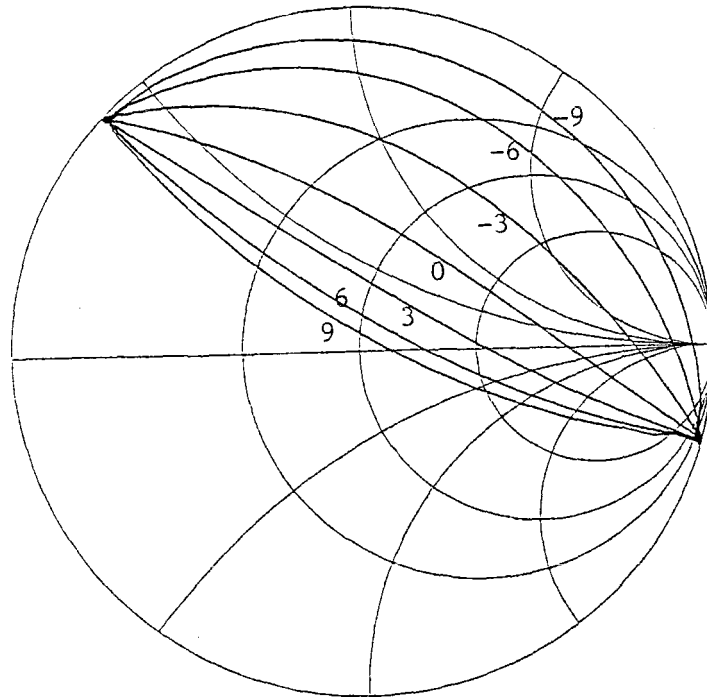
Figure 3.4 Mixer gain vs. $\mathcal{Y}_S$ for the DSB mixer. Gain is shown in contours of constant $\mathcal{G}_{01}$, expressed in dB. The calculations are done for junction 2 at frequency $.1\nu_{GAP} = 130.5$ GHz, assuming $\mathcal{Y}_S = \mathcal{Y}_I$. The lower left half of the Smith chart, with no contours of gain in it, is the region in which infinite gain is available from the mixer.
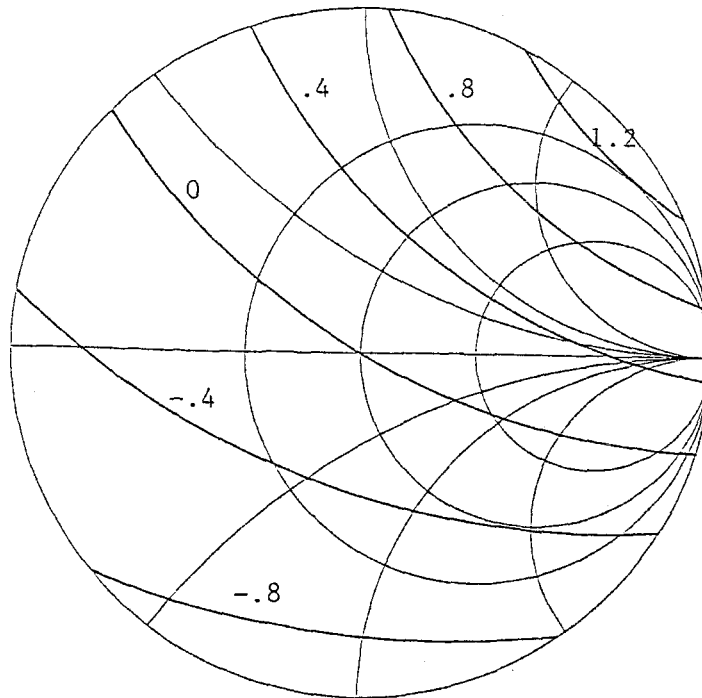
Figure 3.5 Mixer IF output admittance vs. $\mathcal{Y}_S$. The contours are labeled with the normalized output admittance, G_{IF}/G_N. Calculations are done using junction 2 at frequency $.1\nu_{GAP} = 130.5$ GHz, assuming $\mathcal{Y}_S = \mathcal{Y}_I$.

G_0, as can be achieved. Two effects must be considered in the construction of a mixer along these lines, saturation and stray capacitance. Saturation of the SIS mixer can occur when the signal power becomes comparable to the LO pump power, just as it can in classical mixers such as those based on Schottky diodes.

However, a more important saturation problem has been identified by Smith and Richards (1982) for SIS mixers with high conversion efficiency. This saturation results from the high rms voltages, V_{OUT}, developed across an SIS which is delivering a large output power to a following amplifier. For the case of negative match, where $G_0 = -G_{IF}$, V_{OUT} is infinite. For G_0 matched to $G_{IF} > 0$, $V_{OUT} \propto G_{IF}^{-1}$. While V_{OUT} accounts for the IF output power, it can also be considered as a random variation in the dc bias voltage, V_0. In section 3.3, the SIS mixer is seen to have a gain maximum which falls off if the dc bias voltage is changed by a significant fraction of a "photon step" voltage, $\hbar\omega_{LO}/e$. When V_{OUT} is a significant fraction of this voltage, the SIS mixer spends only some fraction of time biased near the high gain maximum, for the rest of the time it is at a bias voltage corresponding to a lower conversion efficiency. This results in a gain compression as an increasing V_{OUT} results in an increasing amount of time spent in a low gain state. One way to avoid this kind of saturation when G_{IF} gets small is to keep G_0 at some reasonably large value. This results in an IF mismatch, lowering the mixer gain. However, by turning down the gain, higher tolerance to saturation is achieved.

Another problem with high output impedances followed by high input impedance amplifiers is stray capacitance. There will exist some amount of capacitance between the IF output line and ground. This capacitance shunts G_{IF} and G_0. It causes degradation of output power when

$$C_p\omega_0 \sim G_{IF} + G_0. \qquad (3.5.1)$$

As G_{IF} gets small, and G_0 matches it, the amount of parasitic capacitance C_p that can be tolerated also shrinks. Even though C_p can be tuned out by careful circuit design, the small amount of capacitance that will ruin a low admittance IF circuit makes it very difficult to tune C_p out simultaneously over the entire output bandwidth. This problem, like saturation, is mitigated by keeping G_0 reasonably large, at the expense of a lower gain due to mismatch.
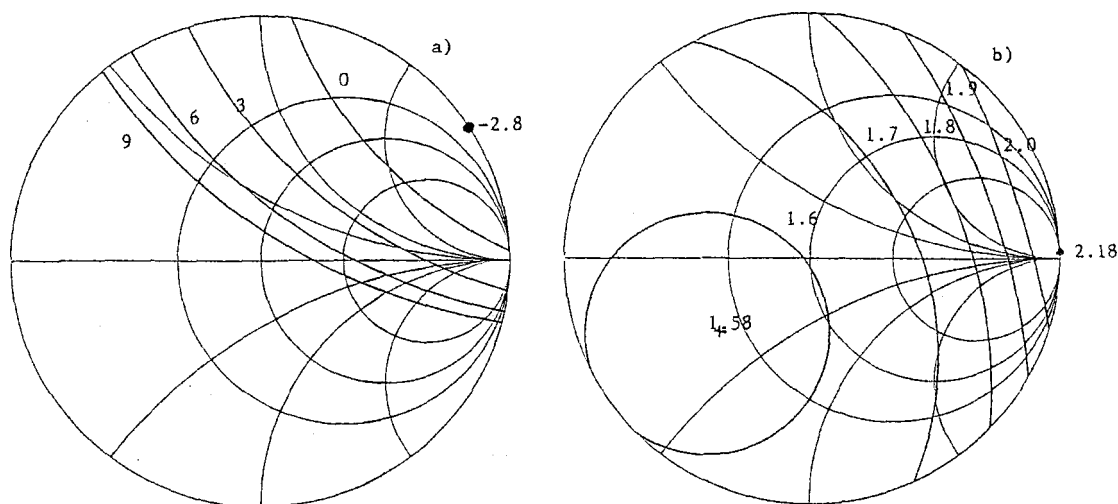
Figure 3.6 Mixer performance vs. y_I, for y_S fixed. The calculations are done using junction 2 at frequency $.1\nu_{GAP} = 130.5$ GHz. a) Available gain in dB vs. y_I. Infinite gain is available for y_I in the lower left half of the Smith Chart. The minimum gain point of -2.8 dB is shown by a •. b) Mixer noise in photons, N_M, vs. y_I. Minimum noise occurs at the point shown with a +, maximum noise occurs at the point labeled with a •.

The results shown above are for the DSB mixer, where y_S and y_I are varied simultaneously. In principal, a mixer could have y_S and y_I set to unequal optimum values. When y_I is held fixed, and y_S is allowed to vary alone, the pictures of mixer temperature and gain generated are not remarkably different from the DSB case presented. This is true because the value of y_S has more effect on mixer performance than the value of y_I. When y_S is held fixed, mixer performance vs y_I shows optimum performance for $y_I \neq y_S$, generally.

Performance found by varying y_I while y_S is held near its optimum value are shown in fig. 3.6. y_I has a much more significant effect on available mixer gain than it does on mixer noise. Over all possible values of y_I, the predicted mixer temperature ranges from 9.9 K (1.6 photons) to 13.6 K (2.2 photons). However, the available conversion gain varies from -2.8 dB to infinite available gain as the image is tuned. As in the DSB case, this gain variation is essentially due to a change in G_{IF} as y_I is changed.

The best and worst gain occurs at values of y_I which are 1) completely reactive, lying on the outer edge of the Smith chart, and 2) almost diametrically opposed on the Smith chart. While a poor choice of y_I can reduce conversion gain, it cannot reduce it by very much. Similarly, an optimum choice of y_I cannot improve mixer performance by any significant amount over the DSB tuning results.
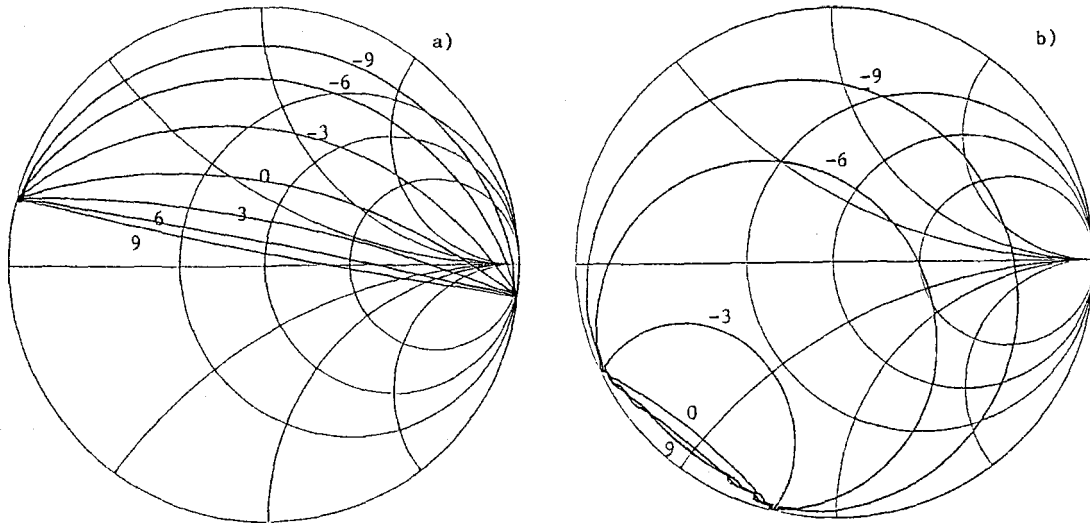
Figure 3.7 Gain vs. $\mathcal{Y}_S$ for two different junctions. Gain contours are labeled in dB. a) Junction 1 at frequency $.1\nu_{GAP} = 148.0$ GHz. Infinite gain is available for $\mathcal{Y}_S$ in the lower half of the Smith chart. b) Junction 3 at frequency $.1\nu_{GAP} = 103.2$ GHz. Large but finite gain is available for $\mathcal{Y}_S$ in only a very small area at the lower left of the Smith chart.

There is a practical difficulty in a mixer with $\mathcal{Y}_S$ and $\mathcal{Y}_I$ chosen to be at their different optima. The output admittance of the mixer is actually, in general, complex,

$$Y_{IF} = G_{IF} + iB_{IF}. \tag{3.5.2}$$

In principle, B_{IF} can be tuned out by proper design of the IF circuit. Further, for the DSB mixer, $B_{IF} = 0$ anyway due to the symmetries of the Y matrix. With the DSB constraint removed, $Y_{IF} = (-.2 - .2i)G_N$ when $\mathcal{Y}_I$ is chosen to minimize T_M. For match, the IF circuit must present an approximately constant reactive admittance of $+.2i\,G_N$ over the entire IF output bandwidth. It is rather difficult to design a circuit with a non-zero imaginary admittance that remains constant over any significant frequency range.

All the results shown so far are calculated using junction 2 from fig. 3.1. Fig. 3.7 shows the DSB gain predictions for junctions 1 and 3. Junction 1 has an essentially ideal I-V, while junction 3 is significantly less ideal than junction 2. The less ideal junction 3 does not quite achieve infinite available gain, but gain greater than $+10$ dB is calculated. Again, it occurs for $\mathcal{Y}_S$ in the lower left of the Smith chart, but the area of the Smith chart over which high gain is predicted is much less than it was with junction 2. The effect of the nearly ideal I-V of junction 1 is to make infinite gain available over almost all of the Smith chart. Mixer temperature for this junction is at the quantum limit when $\mathcal{Y}_S = Y_{LO}$ as discussed in chapter 2.
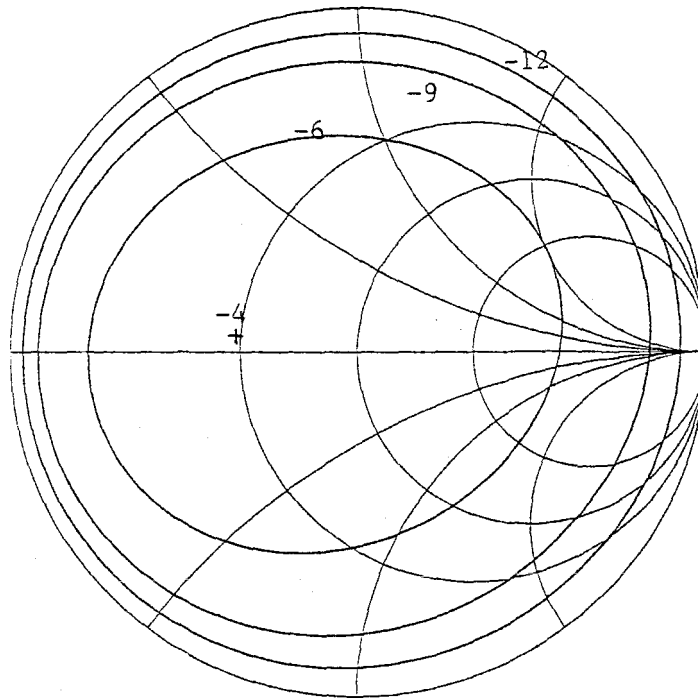
Figure 3.8 Gain vs. $\mathcal{Y}_S$ at a lower frequency. Available gain, labeled in dB, is calculated for junction 2 at a frequency $.025\nu_{GAP} = 32.6$ GHz, keeping $\mathcal{Y}_S = \mathcal{Y}_I$. The maximum available gain point is shown by a +.

All results so far have been at the same normalized frequency of $.1\nu_{GAP}$, which ranges from 103 GHz for junction 3 through 130 GHz for junction 2 to 145 GHz for junction 1, due to the differences in V_{GAP}. For normalized frequencies from .1 to about .8, the results are not very different from those shown. At lower frequencies, the quantum mixer feature of available conversion gain disappears. Fig. 3.8 shows the gain available from junction 2 at a frequency of $.025\nu_{GAP}$, or about 32 GHz. These contours show that the highest conversion efficiencies occur for $\mathcal{Y}_S$ somewhere in the middle of the Smith chart, which is what usually is expected in a classical diode mixer theory. It should be noted that the same calculation for the nearly ideal junction 1 shows infinite available gain at most $\mathcal{Y}_S$. The quantum mixer phenomenon of infinite gain has a lower frequency limit which depends on the sharpness of the I-V. Junction 1 is so sharp that even at a frequency of $.025\nu_{GAP}$, its behavior is still quantum.

3.6 Performance vs. Frequency

In this section, fully optimized mixer performance is presented as a function of LO frequency. The calculations are done for the four junction I-Vs shown in fig. 3.1. For each junction, at each frequency,
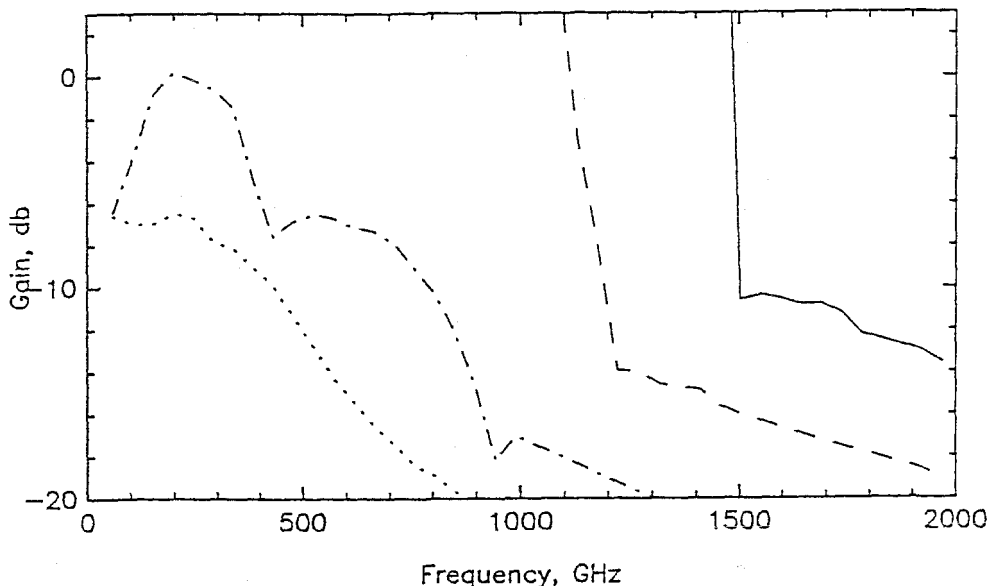
Figure 3.9 Gain vs. frequency for four tunnel junctions. The available gains for the four junctions of fig. 3.2 are shown as LO frequency is varied. At low frequencies, the available gains for junctions 1 and 2 are infinite, and therefore do not appear in the figure.

the values of $y_S = y_I$, V_0, and V_{LO} are found which minimize the receiver noise temperature, T_R in (3.1.4), assuming an IF amplifier chain noise of $T_{IF} = 10$ K. The IF amplifier chain input admittance, y_0, is assumed matched to the mixer output admittance, Y_{IF}, for this optimization. By finding the optimum mixer in this way, high mixer gain and low mixer noise are traded off against each other just as they would be in a real receiver.

Fig. 3.9 shows the maximum available gain. The nearly ideal I-V of junction 1 has infinite available gain up to its gap frequency, ν_{GAP}. The good, but noticeably imperfect I-V of junction 2 also shows high gain up to its gap frequency. The very non-ideal I-V of junction 3 provides non-classical conversion efficiencies of > -3 dB up to about 300 GHz. Finally, junction 4, the SIN, is seen to provide at most -6 dB gain, and this falls off faster than any of the SIS gains, since ν_{GAP} for the SIN is much less than the SIS gap frequencies.

The mixer noise, shown in fig. 3.10, again favors the SISs over the SIN. The best SISs are well within a factor of 2 of quantum limited noise, $N_M = 1$, over most of the frequency range up to ν_{GAP}. The SIN is able to outperform junction 3 below 500 GHz. SIS junctions 1 and 2 are both at physically higher temperatures than the SIN, and yet both the SISs have much lower noise at all frequencies.
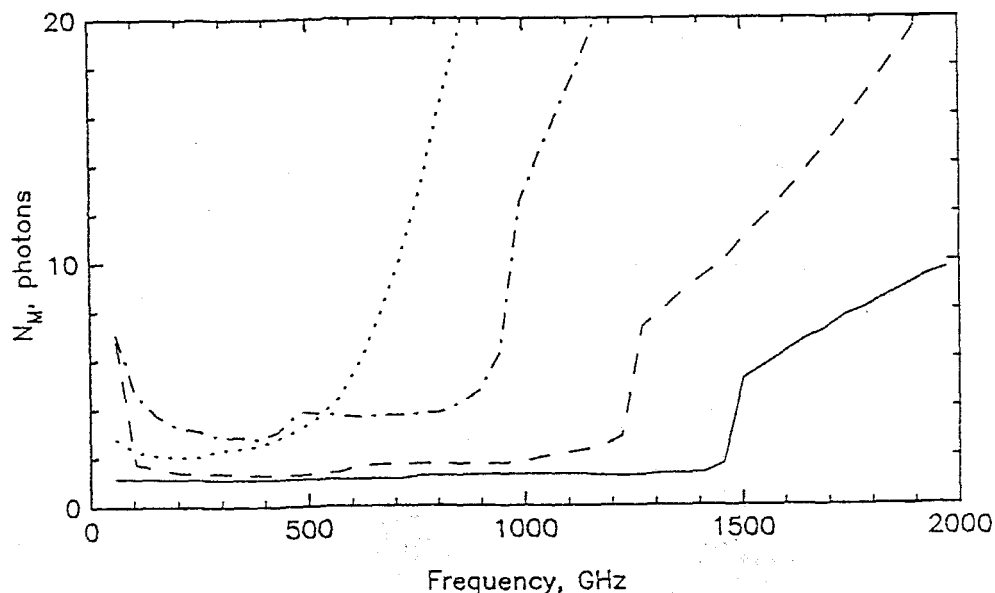
Figure 3.10 Mixer noise, N_M, vs. frequency for the four junctions of fig. 3.1.

In both the gain and the mixer noise, their is an upper frequency limit to efficient mixer performance of ν_{GAP}. The reason for this can be seen from the semiconductor model shown in fig. 1.7. When the dc bias V_0 is just below the diode turn on voltage of V_{GAP}, absorption of a photon of small energy will result in an extra electron in the diode current, and this photon is thus detected. However, there are two ways to absorb a photon of energy $h\nu_{GAP}$. It can result in an electron in the diode current, just as occurs for low energy photons. However, its energy is sufficiently high that it can also cause an electron to tunnel backwards across the diode, producing a current of the opposite sign. On average, there will be more electrons tunneling forward than backward, so there will still be a net photocurrent. However, the responsivity does drop to a fraction of what it was before this backward tunneling became possible, resulting in a sharp drop off of mixer response at ν_{GAP}.

In the mixer noise, a feature can be seen in all three of the SIS predictions at a frequency of $\nu_{GAP}/2$. This is a result of electron tunneling assisted by the simultaneous absorption of two photons. Below the frequency $\nu_{GAP}/2$, it is always possible to bias the junction so that even the two photon process can only cause forward conduction of tunneling electrons. Above $\nu_{GAP}/2$, any dc bias $V_0 < V_{GAP}$ results in a two photon absorption process which can result in electrons tunneling in either direction across the

diode. Just as above for the single photon process, this results in a sudden drop in diode photo-response. Under optimum bias conditions, the single photon process is much more important than the two photon process, so the degradation in performance from the loss of the two photon photocurrent is not nearly as severe as the sudden fall off in performance at ν_{GAP}.

The dc and LO voltage bias points for optimum performance are shown in fig. 3.11. These are the values which minimize the receiver noise temperature, T_R, assuming an IF amplifier chain noise temperature of $T_{IF} = 10$ K. The optimum dc voltage bias is always less than V_{GAP}. The LO voltage is shown in terms of the Bessel function argument, $\alpha = eV_{LO}/\hbar\omega_{LO}$. Its optimum value is in the range .4 to .7 for the high frequency range, and it is nearly the same for all four junctions. At low frequencies, this is not true. While junction 1 has $\alpha < 1$ at the lowest frequency calculated, junctions 2 through 4 require higher LO drive levels at low frequencies.

This is due to the transition from quantum to classical behavior at low frequencies for these junctions. In the expressions of Tucker's theory, the $J_n(\alpha)$ Bessel function term can be identified with the physical process where n photons are absorbed simultaneously to cause an electron to tunnel. Indeed, the probability of the n-photon process is proportional to $J_n(\alpha)$. The Bessel functions have the property that $J_n(\alpha)$ is very small for $\alpha \lesssim n$. Finding the optimum value of α to be in the range .4 to .7 over a large range of frequencies indicates that the most efficient mixing occurs when the single photon process dominates the $n = 2$ and higher processes. This result holds for junction 1 right down to the lowest frequency for which the calculations are done. However, junctions 2 through 4 do not have sharp I-Vs on the scale of a single photon step at the low frequencies. Hence, it is necessary to absorb a few photons simultaneously to get efficient photo-detection, and α must rise so that these multi photon processes have reasonable probability.

The optimum signal source admittance $\mathcal{Y}_S = G_S + iB_S$ is shown in fig. 3.12. The optimum G_S is close to G_N for all junctions over the higher part of the frequency range. However, junction 1 has an optimum G_S which rises quickly at low frequencies. This is true for the low values of α which were found to be optimum for this junction. Junction 1 is also capable of producing good mixer performance when $\mathcal{Y}_S \sim G_N$. For this lower value of source admittance, a higher value of α optimizes the mixer.
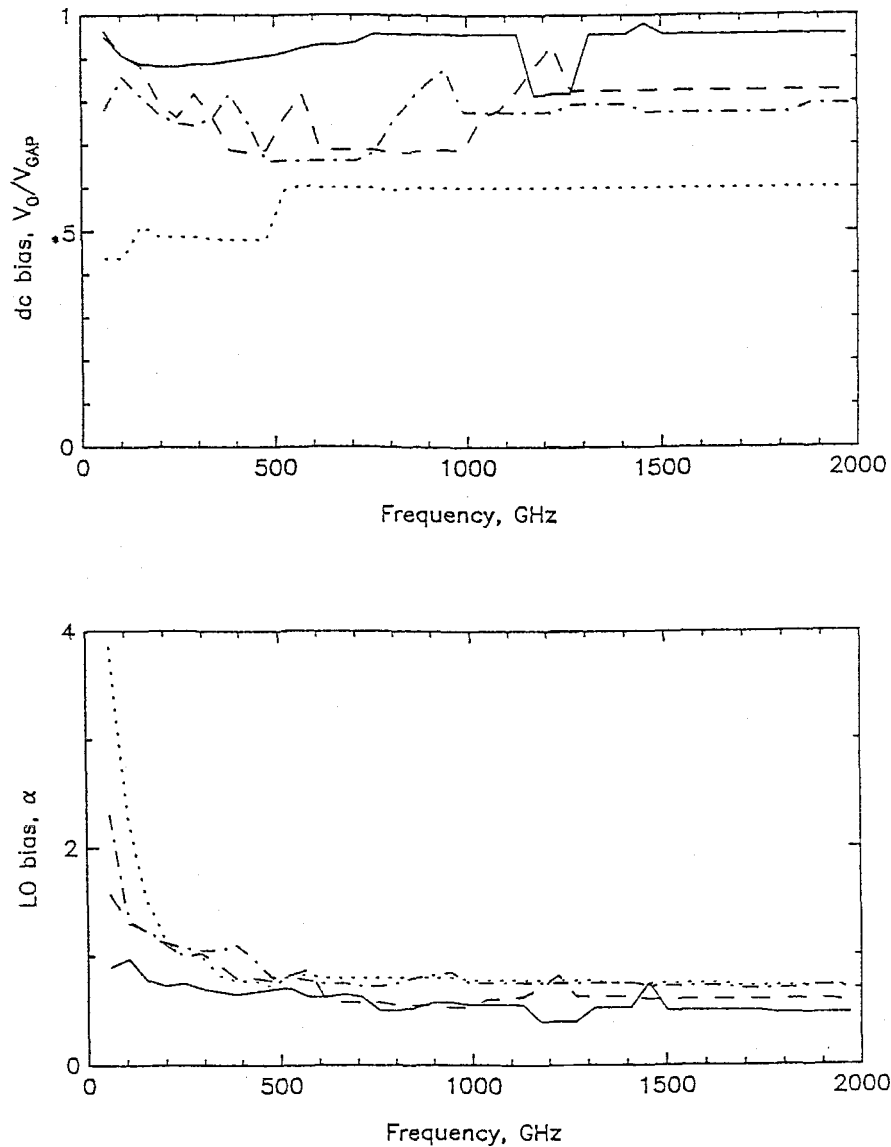
Figure 3.11 Optimum bias vs. frequency. The dc and LO voltages which optimize T_R for the four junctions of fig. 3.1 are plotted. a) The dc bias voltage. b) The LO voltage, shown in terms of the Bessel function argument $\alpha = eV_{LO}/\hbar\omega_{LO}$.

The imaginary part of the optimum source admittance is also shown in this figure. It is not tremendously different from zero for any of these junctions at any of the frequencies investigated. This suggests in mixer design that it will be important to use very low capacitance SISs for higher frequencies, or else to design a circuit in which SIS capacitance is carefully tuned out in some way.

3.7 Summary

In this chapter, an overview of results from numerical calculations has been presented. The method
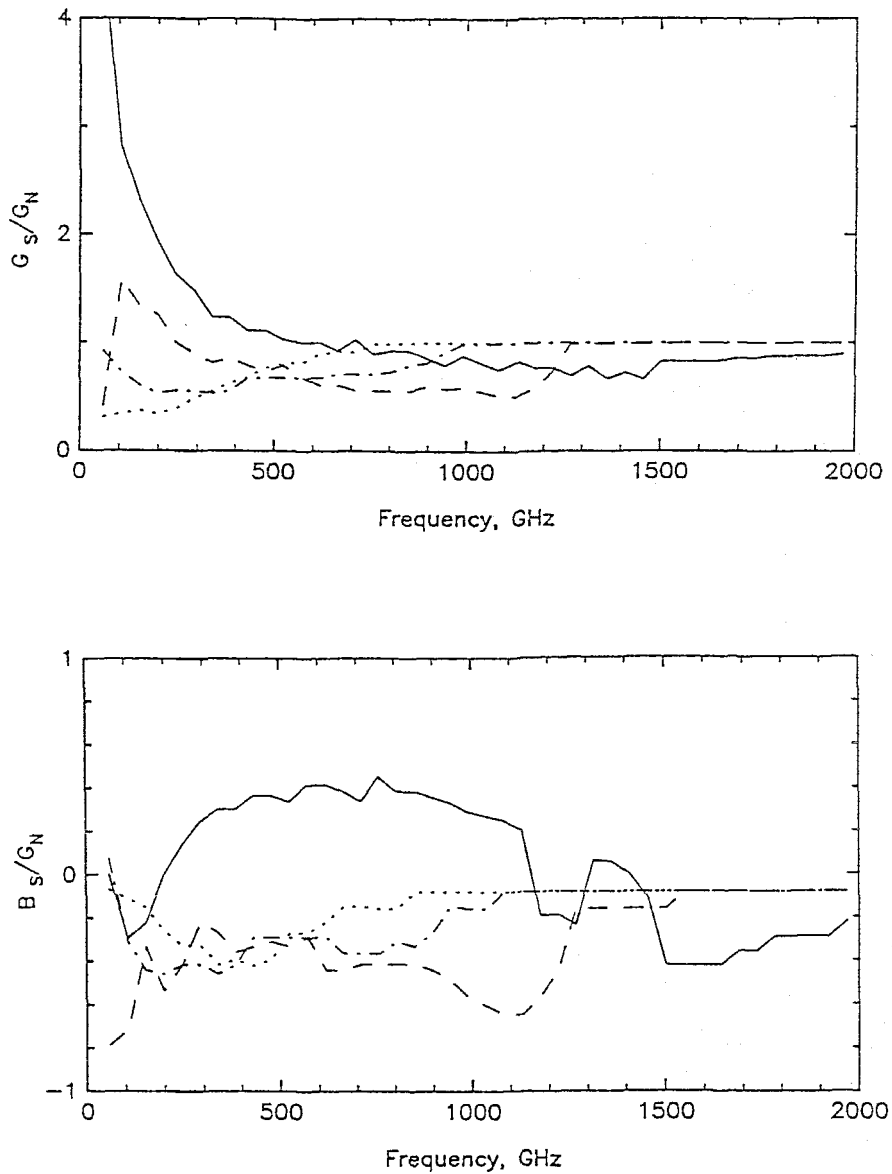
Figure 3.12 Optimum signal source admittance vs. frequency. The real and imaginary parts of $\mathcal{Y}_S = G_S + iB_S$, which result in minimum T_R are plotted for the four junctions of fig. 3.1. a) The real part, normalized to G_N. b) The imaginary part, similarly normalized.

for digitizing I-Vs for use in the calculations was described. Mixing performance as a function of dc and LO bias showed the transition from classical to quantum behavior as LO frequency was increased.

The effects on mixer performance of signal and image source admittances were discussed. While highest mixer gain is usually achieved for very low source admittances, low mixer noise occurs for $\mathcal{Y}_S \approx Y_{LO}$, which is typically close in value to G_N. The minima in mixer noise were fairly broad, suggesting that a mixer circuit designed to present a source admittance $\mathcal{Y}_S \approx G_N$ should provide near optimum mixer performance.

The optimum theoretical performance for various tunnel diodes was calculated as a function of frequency. Reasonable SIS diodes were found to give mixer noises less than $N_M = 2$ up to a frequency proportional to their gap voltage, $\nu_{GAP} = 2eV_{GAP}/h$. SIN performance was predicted to be reasonable at low frequencies, but its lower ν_{GAP} resulted in very poor performance above 600 GHz.

For the lead alloy junctions shown, the high frequency limit, ν_{GAP}, is about 1500 GHz. Junctions made from niobium-nitride are now being developed for mixer applications (LeDuc *et al.*, 1986). These junctions have higher superconducting transition temperatures than lead alloys (13 K instead of 7 K), and correspondingly higher gap voltages (5.5 mV as opposed to 3 mV). With NbN SISs, ν_{GAP} may eventually be as high as about 3000 GHz.

Chapter 4 – SIS-Bowtie Mixer

"This new outfit will save us from Ahab's wrath. You
see, this bowtie allows me to see to higher frequen-
cies. We'll surely spot the quantum limit now."
— Ishmael, in *Moby Mike* or *Captain Phillips
and the Great White Wengler,* by Erich Gross-
man and Jeff Stern.

4.1 Design Overview

This chapter will discuss the design, construction, and testing of a prototype mixer which provides

very low noise detection for millimeter and submillimeter wavelengths. SIS tunnel diodes are the

detector for this mixer. Radiation is coupled to the tunnel diode through a scheme which has been used

for imaging arrays (Rutledge, Neikirk, and Kasilingam, 1984). The optical arrangement of this mixer

is shown in fig. 4.1. The SIS is fabricated at the center of a superconducting bowtie antenna. The

integrated diode and antenna are placed on the back of a truncated quartz sphere (hyperhemisphere).

Radiation is focussed into the bowtie by the hyperhemisphere, and a plastic lens in front of it. The lower

frequency limit (about 100 GHz) of this mixer is set by the size of the lenses and the bowtie antenna,

while the upper frequency limit of this mixer (unknown now, but greater than 761 GHz) is probably

limited by the capacitance of the SIS junction.

Low noise mixers in this spectral range are usually based on waveguide structures. Fig. 4.2 shows

a cross section of the 3 mm wavelength mixers (Woody, Miller, and Wengler, 1985) used at the Owens

Valley Radio Observatory (OVRO). Over about a 30% frequency range, scalar feedhorns give a nearly

perfect coupling between the waveguide mode and the Gaussian free space mode for which the telescope

optics are usually designed. This overall coupling is very important to the ultimate signal to noise ratio

(SNR) of astronomical observations. Poor mode match between the receiver and the telescope results

in a loss of telescope signal coupled to the receiver. Furthermore, the part of the receiver mode which

is not coupled to the telescope will probably be filled with thermal radiation from the receiver room or

the landscape surrounding the telescope. This results in an increase in the noise coupled to the receiver.

Coupling inefficiency therefore hurts SNR in two ways, it lowers signal and it raises noise.
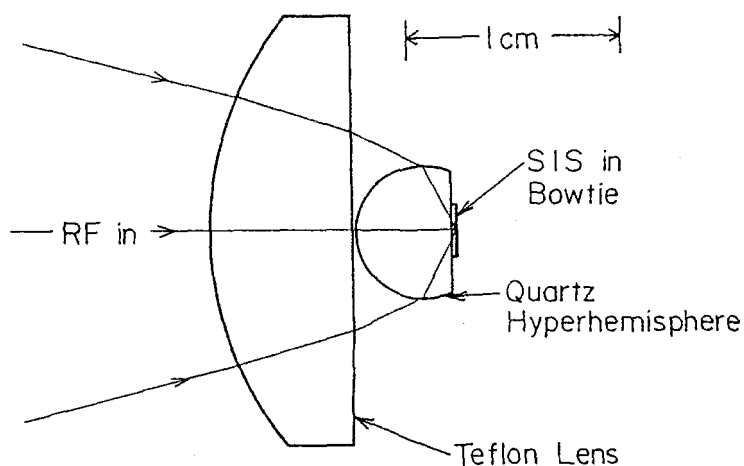
Figure 4.1 Bowtie mixer optics. An SIS junction is fabricated integrally with a planar bowtie antenna, on a thin quartz substrate. This is placed on the flat surface of a quartz hyperhemisphere. Radiation incident on the plastic lens is focussed into the quartz hyperhemisphere, which further focuses the beam into the center of the bowtie antenna. The radiation is thus coupled to the SIS, which is at the center of that bowtie.
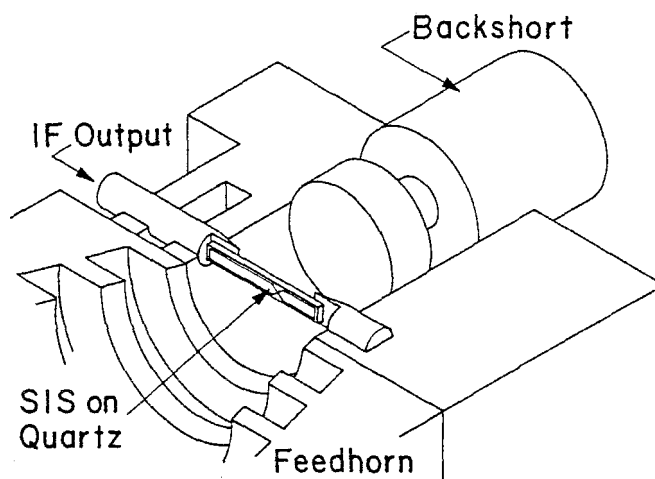
Figure 4.2 Cutaway view of the waveguide-feedhorn mixer block in use at OVRO. The SIS is mounted across a circular waveguide. The waveguide diameter is 2.4 mm, about equal to the free space wavelength of the radiation it will detect. A movable short in the waveguide behind the SIS improves the coupling efficiency between the waveguide and the SIS. A feedhorn efficiently transforms the waveguide radiation to a Gaussian profile free space beam. (Woody, Miller and Wengler, 1985).

The bowtie antenna shown in fig. 4.1 will have a coupling efficiency to the telescope of less than 80% at best, and probably less than 50%, but it will not change much over a very large frequency range. Waveguide structures like the one shown in fig. 4.2, have efficiencies of well over 90% over their frequency ranges of about 30%.

Why then, would one build a low noise receiver in a bowtie antenna? Because the theoretical

work reported previously in this thesis shows that the intrinsic noise of SIS detectors is 50 to 150 times lower than the best receiver noises which are achieved by existing technology. Even with a low coupling efficiency, the SIS-bowtie could still be expected to have much better sensitivity than is actually achieved with other technologies. In addition, the bowtie mixer has two large advantages over waveguide structures. First, the bowtie mixer is cheaper and simpler to build. Second, a single bowtie mixer covers a few octaves of the near-millimeter band, while a waveguide mixer covers a 30 % bandwidth. Even if outperformed by a waveguide mixer in some narrow band, the multi-octave coverage of the bowtie would still make it worthwhile for many applications. As will be seen, however, it does as well as or better than other technologies which have been used in the 300 to 760 GHz range.

4.2 SIS Junctions

The SIS junction is the most critical element of an SIS mixer. The SIS junctions used for the mixer described here are fabricated in R. E. Miller's lab at AT&T Bell Laboratories in Murray Hill, New Jersey. In the last five years, I have spent one or two months each summer developing and fabricating junctions with Miller. Two different observatories have relied on junctions from this lab, to the exclusion of all other possible technologies. The AT&T Bell Labs 7 m telescope at Crawford Hill, New Jersey has used these junctions for the past six years for all of its 3 mm band observations. At Caltech's Owens Valley Radio Observatory (OVRO), junctions from this lab have been used over for the past six years in receivers for 3 mm to 1 mm (Woody, Miller and Wengler, 1985; Sutton, 1983). For the past three years, three SIS receivers have been run nearly constantly at OVRO as part of a three telescope interferometer for 3 mm observations. Other observatories have used SIS receivers for particular experiments, but only AT&T and Caltech have relied on them exclusively. As a result, a major fraction of the world's experience with SIS receivers on telescopes is with junctions from Ron Miller's lab. In this section, the desired properties of SISs for astronomy are presented. The fabrication procedures and experiences at Bell Labs are discussed.

Except for recent results with niobium junctions at the National Radio Astronomy Observatory's Kitt Peak telescope (Pan *et al.,* 1987), all SIS junctions used on radiotelescopes have been based on

lead alloys. In addition to the AT&T and Caltech efforts, lead alloy SIS receivers have been used on telescopes at Onsala in Sweden (Olsson *et al.*, 1983), at the NASA–Goddard Institute for Space Studies (Pan *et al.*, 1983), and at the IRAM telescope in Pico Veleta, Spain (Blundell *et al.*, 1983; Ibruegger *et al.*, 1984).

The original lead alloy junction fabrication technology was developed at IBM (Greiner *et al.*, 1980) as part of a superconducting logic research effort. All of the labs cited above have developed their processes from the IBM process. The fabrication process at Bell Labs was developed by Dolan, who made the junctions for the first SIS quasiparticle mixers (Dolan, Phillips, and Woody, 1979).

Our SIS diodes are shown schematically in fig. 4.3. The base and counter electrodes are thermally evaporated onto the quartz substrate in a vacuum system at pressures of about 10^{-6} torr. The electrodes are alloys of lead including bismuth, indium and/or gold. Electrode thicknesses range from .2 to .3 μm. One method used to form an electrode of a particular alloy is to make a bulk quantity of the proper alloy, and then evaporate small samples of that alloy onto the substrate. Another method is to sequentially evaporate lead, bismuth, indium and/or gold in the proper ratio to achieve the alloy desired. For the alloys we have used, we have not observed differences in results achieved by these two very different methods. For the sequential evaporation method, the order of evaporation of the elemental components does not seem to matter. Since we do not see differences as we vary this part of the process, we conclude that, for the limited range of alloys we have tried, the various components of the alloy interdiffuse readily.

After the base electrode is evaporated, the vacuum chamber is filled with dry oxygen gas to a pressure of about 5×10^{-2} torr. A dc discharge is run through this gas in the vicinity of the substrate for about five minutes. This produces a layer of oxide on the base electrode, which serves as the insulating tunnel barrier for the eventual SIS. After oxidation, the chamber is pumped down once again to 10^{-6} torr, and the counterelectrode is evaporated onto the substrate.

The base electrode alloys always contain 5% to 8% indium by weight. The counter electrode never contains any indium. This results in consistently high current density junctions. Researchers at IBM claim that the electrons in this system are tunneling through a Schottky potential barrier (Baker and Magerlein, 1983). They have determined that the predominant oxide in junctions made this way is
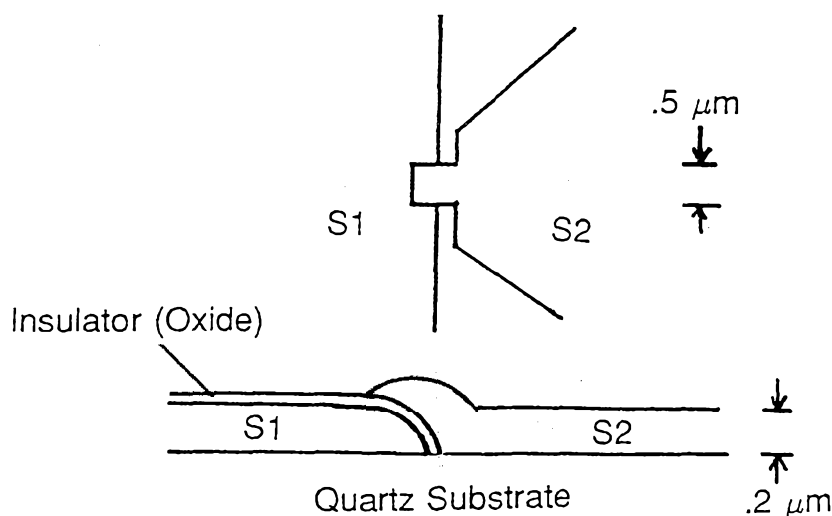
Figure 4.3 Schematic view of SIS junction. At the top is shown the view looking down onto the junction. Below is shown a cross-section through a junction (not to scale). The current path is from S1, through the insulator, to S2.

In_2O_3. This oxide is a semiconductor, as opposed to an insulator. In these junctions, the indium oxide is degenerately doped by excess indium which diffuses into it from the base electrode. The counter electrode, an alloy with no indium content, is on top of the doped indium oxide. Excess indium diffuses out of the top few angstroms of the oxide layer, into the top electrode. The top few angstroms of the In_2O_3 are therefore undoped. The result is a Schottky barrier between the oxide layer and the top electrode.

The tunnel barriers in other SIS technologies usually consist of a good quality oxide of 1 to 2 nm thickness. The oxide is an insulator, so it presents a potential barrier to electrons which is as wide as the oxide layer is thick. As a result, tunneling currents vary exponentially with oxide thickness in these junctions. To fabricate junctions like this with consistently high current densities, it is necessary to fabricate extremely thin oxides. The thinner an oxide, the more probability that there is a pinhole flaw, which results in a short-circuited junction. The indium oxide layer, on the other hand, consists of a physically thick oxide with a consistently thin Schottky tunnel barrier. As a result, consistently high current densities are achieved with these junctions.

For making small area junctions, we use a method invented by Dolan of AT&T Bell Labs (Dolan, 1977) which is based on the tri-level stencil technique (Dunkleberger, 1978). In this method, the base and counter electrodes are both deposited through the same photoresist stencil. In most other techniques,
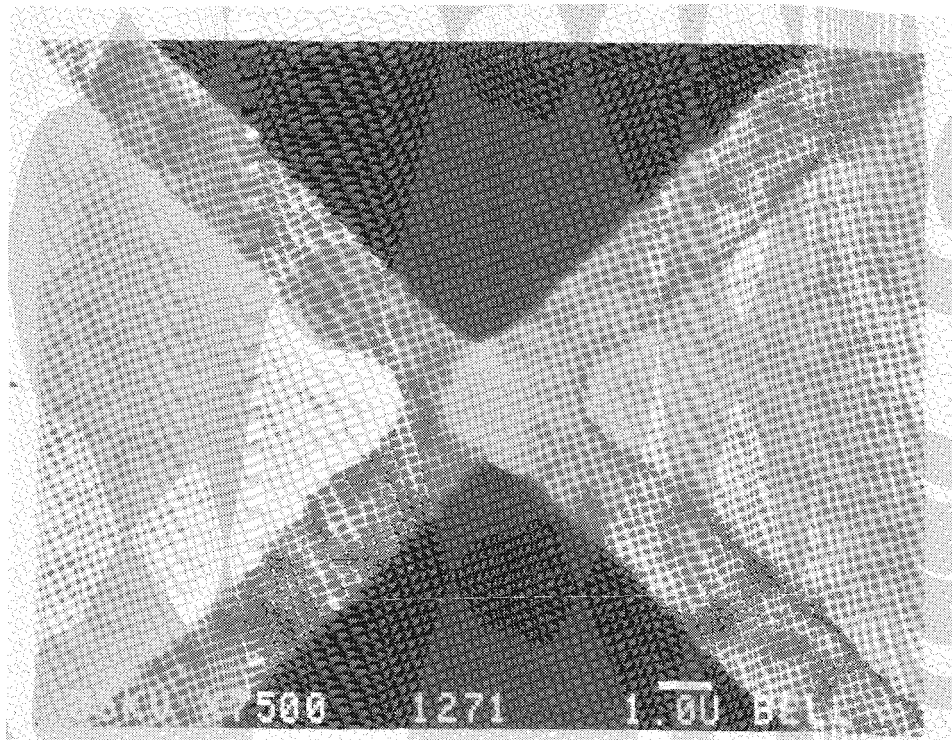
Figure 4.4 Micrograph of an SIS-Bowtie. A scanning electron micrograph of an SIS-Bowtie shows the overlapping superconductors which form the SIS, and the small scale part of the bowtie antenna. The bowtie shape is accurately maintained down to about 1 μm scale size.

substrate processing is required between the evaporations of the base and counter electrodes. This means that the base electrode surface is contaminated by whatever processing steps are required to pattern the counter electrode. With Dolan's technique, however, the base electrode is deposited, oxidized, and the counter electrode is evaporated without the vacuum system being opened up to air. It is also possible with Dolan's technique to make junctions with overlap dimensions of about .5 μm even when the original photolithographic technique used to make the tri-level stencil has a resolution of 1 μm. Using this method we are able to achieve junction areas of $\sim$ .3 $(\mu m)^2$ with tolerable consistency. An electron micrograph of one of these junctions is shown in fig. 4.4.

Two different alloys have been used for junction fabrication. The first is $Pb_{97}Au_{03}$. The superconducting energy gap voltage (Δ/e) of this alloy is about 1.2 mV at 4.2 K, and it transition temperature, T_C, is about 7.2 K. The gold is present in this alloy to avoid the formation of "hillocks" in the lead film as the junction is cycled in temperature between room temperature and 4.2 K. The second alloy we have tried is $Pb_{71}Bi_{29}$. This alloy has been used with good results by another lab (Gundlach et al., 1982). PbBi alloy has a superconducting gap voltage of about 1.5 mV at 4.2 K, T_C is about 9 K. The presence

Table 4.1 – Desirable Characteristics for SIS diode

Desirable electronic characteristics:

1. Good quality I-V. As discussed in section 2.6, an SIS with a perfect I-V responds perfectly to absorbed radiation.

2. Low capacitance. The lower the junction's capacitance, the higher the frequency of radiation that can be coupled to it from a given rf circuit.

3. High current density. A small area junction must carry a high current density so that its radiation impedance is low enough.

4. High critical temperature (T_C). For a given operating temperature, an SIS made from higher T_C superconductors has a better I-V.

Desirable physical characteristics:

1. Small size. Junction capacitance is proportional to junction area.

2. Thermal cyclability. Cycling between cryogenic operating temperatures and room temperature should not degrade or destroy the SIS.

3. Shelf-life. The longer a good junction can be stored for later use, the better.

4. Yield/Repeatability. It should be possible to fabricate high quality junctions on demand.

of ~ 8% indium in the base electrode does not seem to affect the superconducting characteristics of either of these alloys.

We now discuss the quality of the junctions we make. The desirable characteritics of an SIS junction for use in radioastronomy can be divided into its desirable electronic characteristics, and its desirable physical characteristics. Table 4.1 lists these desirable characteristics. Our results with lead junctions can be generally summed up by saying that their electronic characteristics are good to excellent, but that their physical characteristics range from fair to just barely tolerable.

An I-V for one of our PbAu alloy junctions cooled to 4.5 K is shown in Fig. 1.3b. The curve deviates from the ideal SIS curve shown in fig. 1.3a. The real SIS requires a finite dc voltage range in which to switch from its off state to its on state. In its off state, the real SIS carries some current, whereas the ideal SIS does not. There are discontinuities and features present which are due to tunneling of Cooper pairs of electrons. One such feature is the existence at zero voltage of a finite current. This is the dc Josephson effect, also referred to as the supercurrent (Josephson, 1965). It is not possible to bias

the junction at dc voltages between zero and the dropback voltage (V_D). This is indirectly due to the ac Josephson effect. If a finite dc voltage V_0 exists across an SIS, there is a sinusoidal current flowing across the junction at the Josephson frequency (1.2.3). If the junction has a large capacitance, or is otherwise shorted, then these currents can flow without generating much voltage across the junction.

However, if the junction capacitance is small and the junction is not otherwise shorted, these currents will generate relatively large voltages. These voltages will in turn change the Josephson current being generated. Detailed solutions of the current and voltage waveforms depend on details of the circuit external to the junction through which these currents must flow. These solutions include period doubling, quadrupling and chaotic forms. The driving force in this system is the ac Josephson current which flows at a frequency which is proportional to the dc voltage across the junction. Above a certain voltage, V_D, this frequency is high enough that the junction capacitance C_J guarantees small rf voltages which do not result in chaotic behavior. Below V_D, the Josephson frequency is low enough so that rf voltages are large, and chaotic solutions keep the junction from having a stable dc voltage on it.

In fig. 3.1, junction I-Vs are shown for different alloy junctions cooled to different temperatures. The best of these I-Vs are good enough so that at frequencies above 100 GHz, their mixer performance should be only slightly worse than ideal. Therefore, in terms of I-V quality, lead alloy junctions are good.

A real SIS can be thought of as an ideal "point" junction, shunted by a capacitance, C_J. This capacitance is due to the fact that, except for the tunneling currents, an SIS is a superconducting parallel plate capacitor. The capacitance between the base and counter electrodes is

$$C_J = \frac{\epsilon \epsilon_0 A}{d} \qquad (4.2.1)$$

where A is the overlap area of the junction, and d and ϵ are the effective thickness and dielectric constant for the tunnel barrier. For indium oxide Schottky barriers, the values of d and ϵ yield a capacitance of about

$$C_J = 50 \text{ fF } \frac{A}{(\mu m)^2} \qquad (4.2.2)$$

for high current density junctions (Baker and Magerlein, 1983). The smallest area junctions we make are about 1/4 $(\mu m)^2$. The minimum C_J is therefore about 13 fF.

The current densities in our junctions are about as high as any reported for SISs with good quality I-Vs. We can fabricate a R_N = 25 Ω junction of area .25 $(\mu m)^2$, which corresponds to supercurrent densities of a few times 10^4 A/cm^2. With a capacitance C_J = 13 fF, these junctions have a characteristic RC roll off frequency of about 500 GHz. Our mixer results actually show good performance up to about 750 GHz, verifying that we do indeed have very fast junctions.

The critical temperatures for the alloy films used in these junctions are about 7 K for the PbAu alloys and about 8.5 K for the PbBi. The receivers at OVRO are cooled by closed cycle refrigerators which achieve a minimum temperature of about 4.5 K. At this ambient temperature, the slightly higher T_C of the PbBi junctions results in a significant difference in mixer performance. For mixers cooled to 4.2 K by direct exposure to liquid helium, the PbAu I-Vs improve sufficiently so that there is not a large difference between PbBi and PbAu junction performance.

The thermal cyclability of our junctions is more than adequate. Over 90% of our junctions will survive their first cool down and warm up. Once a junction has survived two thermal cycles, it is extremely rare that further cycling causes it to fail.

It is in terms of shelf-life that our junctions receive a barely tolerable rating. For the PbAu junctions, we find that a usable percentage of junction batches will survive for a few months after fabrication. If stored in liquid nitrogen, storage time may exceed one year, for some batches. Unfortunately, the higher transition temperature PbBi alloy junctions have a very small survival rate when stored. Gundlach *et al.*, (1982) experience no such difficulties with their junctions. Because of the short shelf-life of PbBi SISs, all mixer results presented in this thesis are with PbAu alloy junctions.

The fabrication technique we use for junctions is fairly reliable in the sense that a good batch of junctions can be fabricated with only a few days notice. This is usually accomplished, however, by fabricating three to six batches, of which at least one will be high quality. Many of those batches will, however, be unacceptable. The most common failures are batches with excess current below the turn on voltage V_{GAP}, and batches in which almost all junctions are short circuited.

In conclusion, lead alloy junctions from AT&T Bell Labs are capable of producing low noise receivers for near-millimeter wavelengths. The reliability and shelf-life of these junctions is not very

high. It is sufficient for radioastronomy and laboratory research, as long as new batches from Bell Labs can be fabricated on relatively short notice.

4.3 RF optics

A major difficulty in receiver design at mm and sub-mm wavelengths is to provide efficient coupling of radiation to the detector over a reasonable spectral range. For mm waves, this is most effectively accomplished by placing the detector in a waveguide which has one or more tuning stubs. Radiation is coupled into the waveguide with feedhorns. Fig. 4.2 shows the design of the 3 mm wavelength receivers used at Owens Valley Radio Observatory (Woody, Miller and Wengler, 1985).

Waveguide-based systems have a number of disadvantages at higher frequencies. In the sub-mm band, waveguide dimensions become difficult to work with. For example, a 500 GHz circular waveguide of the same design as shown in fig. 4.2 would have a waveguide diameter of .5 mm. The metal structures for mounting the SIS in the waveguide must be small compared to this diameter. An additional difficulty, waveguide loss increases rapidly with frequency due to surface roughness of the waveguide walls. Practically, this becomes important for frequencies above 500 GHz, even when great care is taken to minimize surface roughness. Finally, waveguide-feedhorn structures have only a one-half octave bandwidth, so many different mixers must be built to cover the near-millimeter band.

For Schottky diode-based mixers, an alternative to waveguide mounting is the quasioptical corner reflector and long wire antenna. These are the only broadband heterodyne receivers currently in use for submillimeter astronomy (Röser et al., 1984; Betz and Zmuidzinas, 1984; Zmuidzinas, 1987). Unlike waveguide structures, a single mixer covers 3 or more octaves in the submillimeter. The corner reflector, long wire antenna radiation coupling scheme is particularly appropriate for Schottky diodes. It would be possible to build an SIS receiver using this scheme. However, the thin-film-on-substrate SIS fabrication technology suggest a planar antenna approach for SIS coupling.

The optics of our mixer were derived from the work of Dean Neikirk and David Rutledge of Caltech. Similar optics have been used for an imaging system at a wavelength of 120 μm (Neikirk et al., 1982). An excellent and extensive review of integrated circuit antennas, including the bowtie scheme discussed

here, has been presented by Rutledge, Neikirk and Kasilingam (1984). The intended operation of this scheme for our mixer is illustrated in fig. 4.1. A 30° wide converging beam of radiation is focussed into a 120° converging beam by the plastic lens and the curved surface of the quartz hyperhemisphere. This beam is coupled, with some unknown efficiency, to a detector at the center of a planar bowtie antenna, which is placed on the flat surface of the hyperhemisphere.

Above some lower frequency limit, the bowtie-on-quartz antenna properties do not change with frequency, suggesting its use in extremely broadband systems. Its frequency independent properties are best presented in the language of antenna design. They are: 1) the radiation pattern of the antenna is not symmetric front to back, 80% of the beam is coupled into the quartz, only 20% goes backwards into the vacuum; 2) the antenna impedance is purely real; 3) the SIS and the antenna form a monolithic structure which minimizes parasitic reactances; and 4) choking of the IF line to avoid RF propagation is achieved automatically by the bowtie antenna. These results are derived and experimentally verified (Rutledge, Neikirk, and Kasilingam, 1984). A complete theory for the bowtie, which compares well with measurements, has been presented (Compton *et al.*, 1987).

The operation of the bowtie antenna can be understood by considering it to be a lossy transmission line. An infinitely long bowtie in vacuum is a lossless radial transmission line. This transmission line has some characteristic impedance Z_0 which is independent of frequency, and radiation travels along this line at the speed of light, c. This same transmission line embedded in a dielectric of refractive index n would have a characteristic impedance Z_0/n and radiation would travel along this line at c/n. If this transmission line is now placed on the planar boundary between a half-space of dielectric on the one side and vacuum on the other, it is no longer lossless. As with any wave-guiding structure on a dielectric-vacuum interface, there is a radiative loss which is predominantly into the dielectric. This radiative loss occurs because purely guided wave solutions have different wave speeds in the dielectric and in the vacuum, c/n and c respectively. These solutions do not match at the interface between the two media. What actually happens is that radiation propagates along the bowtie at some intermediate speed. The fields on the bowtie make a reasonable match with radiation modes that can propagate freely through the dielectric, but they do not match well with any propagating modes in the vacuum. Hence,

a wave propagating along the bowtie is lost predominantly into the dielectric.

The antenna impedance for the bowtie is accurately calculated from the transmission line model (Rutledge and Muha, 1982),

$$Z_{\text{ANT}} \sim Z_0/n_m \qquad (4.3.1)$$

where $n_m = \sqrt{(1 + n^2)/2}$. The index n_m is intermediate between the vacuum and dielectric values, it is interpreted as the effective index for the bowtie transmission line. For a $90°$-wide bowtie on quartz ($n = 2$), Z_{ANT} is about 120 Ω.

The bowtie is frequency independent above some lower frequency limit. Consider an infinite bowtie on a dielectric-vacuum interface. This system must have frequency independent performance since it is self-similar on all length scales. Consider an observer at the center of the bowtie. Looking down the bowtie is like looking into mist, since waves propagating on the bowtie get lost into the dielectric. The distance at which the bowtie is lost in the mist must be some number of free-space wavelengths, say $x\lambda_0$. Now consider each arm of the bowtie truncated to some finite length L. When examined at wavelengths L/x and shorter, the truncation is lost in the mist. Hence, the bowtie is effectively self-similar for length scales L/x and shorter.

There are actually two important length scales for the bowtie. The antenna impedance of the bowtie-on-quartz is frequency independent for $\lambda_0 \lesssim nL$. However, the beam pattern is much more sensitive to the length of the bowtie, and it becomes only approximately frequency independent for $\lambda_0 \lesssim .2nL$ (Compton et al., 1987).

A final property of the bowtie which is particularly nice for millimeter and submillimeter detection is that it automatically isolates the rf frequency from the low frequency leads. Low frequency electrical connections to the antenna can be made at a distance of a few λ/n or more from the center of the bowtie. There will be no rf loss due to propagation of the rf into these connections, since the rf has already jumped off the antenna into the dielectric by this point. With a bowtie on dielectric, it is not necessary to include rf filters on low frequency leads.

The ideal bowtie has no upper frequency limit. The real bowtie will deviate from ideal performance if 1) the bowtie is not accurate on a scale of $\sim .1\lambda$, or 2) the dielectric become lossy, or 3) the conducting
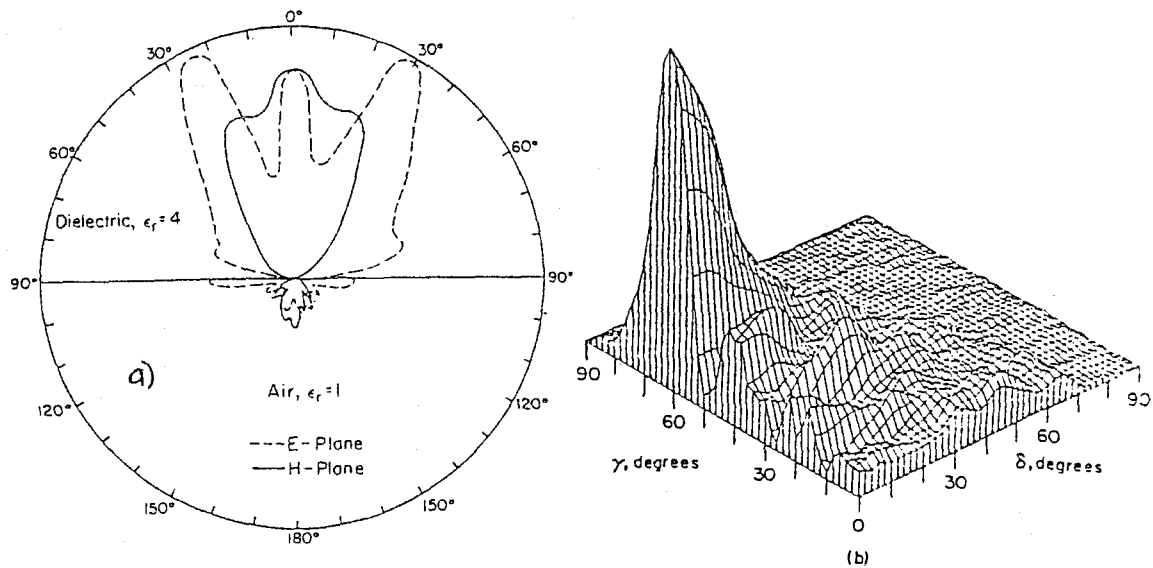
Figure 4.5 Bowtie antenna patterns. a) Pattern measured at 10 GHz on a scale model of an imaging array (Rutledge and Muha, 1982). b) Pattern measured for a single bowtie at 94 GHz (Compton *et al.*, , 1987). The zero of the γ and δ axes show degrees away from the normal in the E-plane and H-plane of the bowtie respectively. Only one quadrant of the pattern is shown, since the other three are simply related to this by the symmetries of the antenna.

material of the bowtie becomes lossy. The SIS that detects the radiation is fabricated at the center of the bowtie as shown in Fig. 4.4. Deviations from bowtie shape occur on the scale of microns, which is much shorter than the wavelength at which loss in the fused quartz will be important ($\sim 200\ \mu$m). The electrical conductivity of the superconducting antenna metal is extremely high for frequencies up to $f \sim 2\Delta/h$ which is about 500 GHz for the lead alloys used here. As the frequency rises above this value, the lead alloy conductivity falls towards its normal state value (Tinkham, 1975). At what frequency this conductivity falls enough to affect performance is not yet known.

The bowtie used in in this mixer has 90° wide bowtie arms, which have a measured antenna impedance of 120 Ω on a dielectric with index $n = 2$ (Rutledge and Muha, 1982). The length of the bowtie arms are 1.5 mm. For bowties with only 60° wide electrodes, beam patterns have been measured at 10 GHz (Rutledge and Muha, 1982) and at 94 GHz (Compton *et al.*, 1987). These measurements are shown in fig 4.5. It has been suggested that the beam of a 90° bowtie should be similar to that of a 60° bowtie, but with a slightly wider E-plane pattern and a slightly narrower H-plane (Rutledge, private communication).

The 10 GHz measurements show a pattern with most of the radiation included in a 60° half-angle

beam into the quartz, which is what the mixer optics were designed to illuminate. Additionally, these measurements show only very small amounts of power in the beam propagating into the vacuum side of the bowtie. The E-plane pattern shows large lobes at 30° away from a line normal to the bowtie plane. For optimum coupling using the optics of fig. 4.1, the beam pattern should be maximum at 0°, but these optics illuminate a large enough angle in the quartz that these 30° lobes should be well illuminated.

The recently reported theory and measurements at 94 GHz (Compton *et al.*, 1987) show beam patterns which are much worse than the earlier 10 GHz measurements around which our mixer was designed. In the measurements at 94 GHz, shown in fig 4.5b, the E-plane pattern has large lobes which are 60° away from the normal to the bowtie. These lobes, carrying most of the power in the bowtie pattern, are just on the edge of the angle which the optics in fig. 4.1 are designed to illuminate. The important difference between the two patterns in fig 4.5 is due to the different length L of the bowtie arms in the two measurements. At 10 GHz, the bowtie arm length was $L \sim .14\lambda_0$. The 10 GHz pattern would correspond to a frequency of about 29 GHz for the $L = 1.5$ mm bowtie arm in our mixer. At 94 GHz, the arm length L was $2\lambda_0$, which corresponds to about 400 GHz for our bowtie. Discussions with Rick Compton about his bowtie theory suggest that the lobes in the E-plane pattern increase in angle as the bowtie is made longer. Contrary to the initial expectations of frequency independent beam patterns, the bowtie pattern in our mixer is probably changing significantly throughout the entire frequency range over which we have measured response.

The beam from the bowtie is focussed by a fused-quartz hyperhemisphere. The optical behavior of a hyperhemisphere is discussed by Rutledge, Neikirk and Kasilingam (1984). It is used because it is capable of aplanatic focussing, *i.e.*, it can focus a beam with no aberrations. Our hyperhemispheres are cut from spheres of fused quartz which have a radius $r = 3.18$ mm. Assuming that the quartz has an index of refraction $n_Q = 2$, the sphere is truncated to a height of $r(1 + 1/n_Q) = 4.76$ mm for aplanatic focussing.

Further focussing of the beam is provided by a plano-convex plastic lens with a design focal length of 2.4 cm. The lens in Bowtie 1 is machined on a lathe from Teflon. In Bowtie 2, The lens is made by pressing polyethylene, which has been heated to about 120 C, in a vacuum mold. A plano-convex
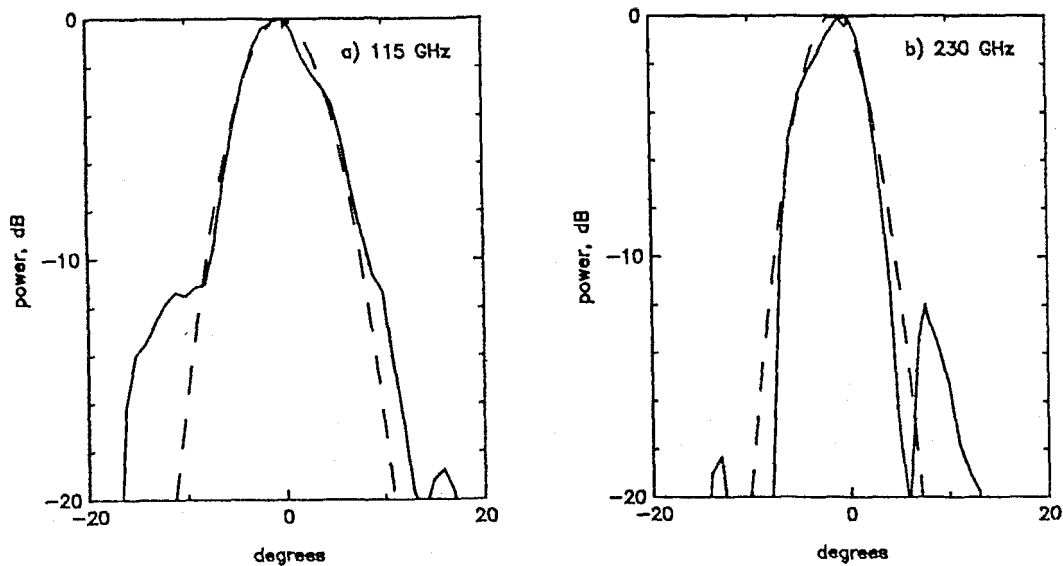
Figure 4.6 Bowtie mixer E-plane beam patterns. The solid lines show the measured E-plane patterns of Bowtie 2. The dashed lines show Gaussian profiles which match the patterns at their half power points. a) Measured at 115 GHz. The full angle between half power points is 8.6°. b) Measured at 230 GHz. The full angle between half power points is 6.7°.

lens shape is used to minimize spherical aberration for the anticipated beam shapes (Jenkins and White, 1957). The curved front surface of the polyethylene lens has a radius of curvature of 1.27 cm, the lens thickness at its center is .38 cm. Polyethylene lens design is based on an index of refraction at submillimeter wavelengths of $n_P = 1.52$ (Smith and Loewenstein, 1975).

Relatively careful measurements of the E-plane beam pattern of our mixer are shown for two frequencies in fig. 4.6. At 115 GHz, the beam is 8.6° FWHM (full width, half maximum). At 230 GHz it is 6.7° FWHM. Low resolution measurements show an H-plane pattern with about the same angular extent as the E-plane. Gaussian profiles that match the measurements at the half power points are shown in the figure. Both beams show reasonably good profiles. They are not as good as scalar feedhorn beams, which would deviate only slightly from gaussian shapes if plotted on this same scale. However, the power is reasonably well contained in a single forward lobe, and we can expect, therefore, to achieve reasonably efficient coupling of that beam to a radiotelescope.

The patterns for the mixer shown in fig. 4.6 are much cleaner and simpler than the patterns for the bowtie antenna shown in fig. 4.5. The reason for this is diffraction. For extremely short wavelengths, the beam pattern of the mixer would have the same structures in it as are shown in fig. 4.5, except the angular scale would be compressed by a magnification factor of four, due to focussing by the hyperhemisphere

and plastic lenses. For instance, lobes at $\pm 30°$ in the bowtie pattern would be focussed to $\pm 7.5°$ in the mixer pattern. However, both the hyperhemisphere and the plastic lens are small enough compared to the wavelength of radiation being focussed, that the sharp structures in the bowtie pattern must be smeared out by diffraction. The small sized lenses act as low pass filters to high spatial-frequency components of the patterns shown in fig. 4.5. Up to 230 GHz, these low pass filters work extremely well, as there is very little high spatial-frequency content in the mixer beams, fig. 4.6. Diffraction effects become less important as wavelengths become shorter, so above some high frequency, the mixer beam pattern will degrade.

Shape is not the only important characteristic of the mixer beam. The overall coupling of the bowtie antenna pattern to the mixer pattern must be considered. Power in the high spatial-frequency components of the antenna beam does not show up in the main Gaussian lobe of the mixer beam. The overall coupling efficiency can be inferred only approximately from the mixer measurements presented below, it is on the order of 20% to 50%. This compares to numbers well over 90% for feedhorn-waveguide based mixers.

In this section, the optics of the bowtie mixer have been described, and measured beam patterns have been shown. Some of the relevant theoretical descriptions of bowtie operation (Rutledge, Neikirk, and Kasilingam, 1984) have been briefly described. The bowtie mixer is shown to have a beam pattern which is reasonably good at 115 and 230 GHz.

4.4 IF Circuit

The output port (IF) circuit of the bowtie mixer is designed to improve mixer gain, short out voltages above the output frequency, and aid cooling of the SIS junction. The arrangement is shown in fig. 4.7. The capacitor is formed by pressing the IF connection wire close to the mixer block, using a .25 mm thick piece of crystal quartz as an insulator. The inductance is achieved by slightly coiling the IF connection wire on its way to the mixer output SMA connector.

The improvement in mixer gain comes about because the IF circuit acts as a matching transformer between the SIS and the following IF amplifiers. In chapter 3, it was seen that a properly operating SIS has an IF output impedance whose magnitude is 100 Ω or higher. This is mismatched from

(a)

(b)
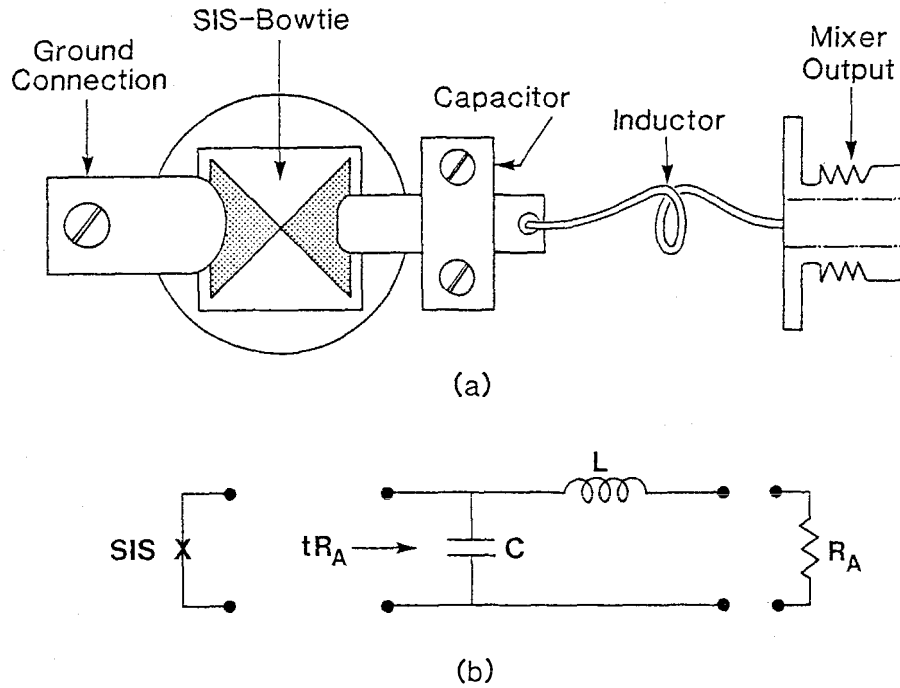
Figure 4.7 Output (IF) circuit. a) The left side of the SIS is shorted to ground. The right side is connected to the output (IF) port. The flat output wire is capacitively coupled to ground as close to the SIS as possible. The wire going to the coaxial connector on the right has a loop in it to provide inductance. b) The lumped-component equivalent circuit for analyzing the output circuit. The output circuit will transform an IF amplifier input impedance of R_A on the right up to tR_A at the SIS.

following amplifiers which usually have 50 Ω input impedances. The IF output circuit transforms the 50 Ω following amplifier impedance to 100 Ω at the SIS. For the case that the SIS output impedance is 100 Ω, this transformation improves mixer gain by a factor of 9/8 (.5 dB). For higher SIS output impedances, the improvement is more substantial. In the extreme case that the SIS output has an infinite impedance, the mixer gain is improved by a factor of 4 (6 dB). The transformer will improve mixer gain for all SIS output impedances above about 71 Ω.

The simple LC circuit shown in fig. 4.7 works as a 2:1 transformer over the output frequency range of 1.1–1.9 GHz. To transform an amplifier input impedance R_A up by a factor of t at angular frequency ω, the desired capacitance is

$$C = \frac{\sqrt{t-1}}{\omega t R_A}. \tag{4.4.1}$$

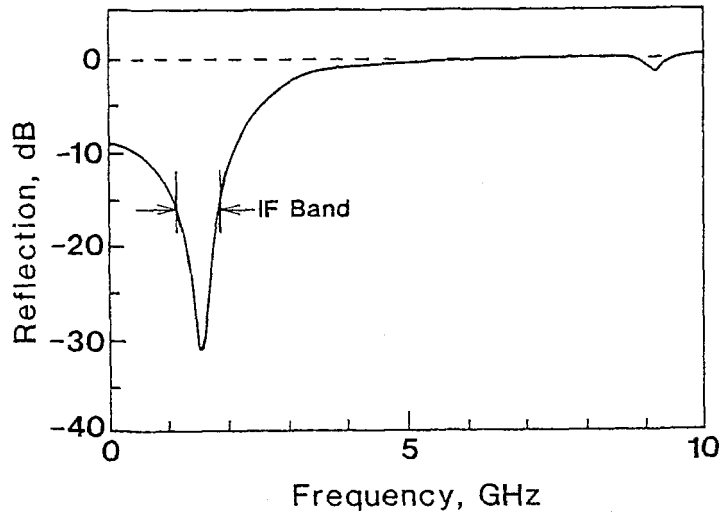Figure 4.8 Reflection coefficient of IF circuit. The transformation properties of the IF circuit are verified by measuring reflection return loss from the mixer with a 100 Ω chip resistor in place of the SIS. The design IF band is centered at 1.5 GHz.

The inductance is chosen so that there is no net reactance at the design frequency,

$$L = tCR_A^2.$$ (4.4.2)

The IF amplifer-isolator combination used in these experiments has $R_A = 50$ Ω. This is transformed by $t = 2$ to 100 Ω at the SIS. Designed for an IF center frequency of $\omega/2\pi = 1.5$ GHz, the desired capacitance is $C = 1.1$ pF and the inductance is $L = 5.3$ nH.

The circuit built to do this transformation is physically about .7 cm long, which is about .35λ at the design frequency. The lumped circuit description of the circuit given above can be expected to be inexact. The actual circuit is tuned using a network analyzer. A 100 Ω chip resistor is put in place of the SIS while this circuit is being built. Transformer operation is then verified by looking at the mixer block power reflection coefficient with the network analyzer attached to the mixer output. If the transformer is operating correctly, the 100 Ω chip resistance appears to be 50 Ω to the network analyzer, and there is no power reflected from the mixer port. The capacitance and inductance can be adjusted to achieve the proper transformation ratio at the proper IF center frequency. The power reflection of the finished transformer is shown in fig. 4.8. At 1.1 GHz, the power reflection is -14.1 dB, this is the worst point in the IF band. At 1.58 GHz, the minimum reflection of -33.1 dB is achieved.

At frequencies immediately above the IF, the transformer appears as a capacitive short to the SIS. Since the capacitor is only 2 mm away from the SIS, it will present a short circuit to frequencies as high as about 15 GHz at the SIS. Smith and Richards (1982) show that an SIS mixer is susceptible to saturation if voltages at or near the output frequency have a root mean square (rms) value of more than about $.1h\nu_{LO}/e$. By presenting a short circuit at out of IF band frequencies, total rms voltage is minimized. Recently, Weinreb (1987) has suggested that low impedance following amplifiers can reduce saturation problems without reducing receiver sensitivity, even though mixer conversion efficiency is lowered. Broad output bandwidths from a mixer such as Weinreb proposes could only be achieved through a close integration of the SIS mixer diode and the transistor which does the first stage of IF amplification.

The capacitor in the mixer output circuit also aids in cooling the SIS diode. The IF line is made to have the proper capacitance to ground by bolting it tightly in a sandwich of mixer block-insulator-IF line-insulator-copper. The mixer block is extremely well heat sunk to a liquid helium bath (or to a closed cycle refrigerator when used at OVRO). Most electrical insulators are fairly good thermal insulators as well. However, crystals such as quartz have high thermal conductivity. By using crystalline quartz for the insulator in this capacitor, the IF line is well heat-sunk to the mixer block. As a result, it serves to help cool the SIS to which it is electrically connected.

4.5 Mixer Block

Two bowtie mixer blocks have been fabricated and tested. Results from the first one have been previously reported (Wengler et al., 1985a, 1985b). In this section, the physical design of the mixer blocks is presented. The primary difficulty of the bowtie mixer blocks has been a proper heat sinking of the SIS junction to the mixer block. A less fundamental consideration dictating design choices is that the bowtie mixer block be usable in cryogenic systems designed for waveguide-feedhorn mixer blocks.

As with cryogenic mixers of many different sorts, the metal used for mixer block construction is oxygen free copper, known usually as either OFC or OFHC. This material is chosen due to its extremely high thermal and electrical conductivities at cryogenic temperatures, and its relatively easy machinablility. An OFC mixer block bolted directly to the cold plate of a helium cryostat or closed-cycle
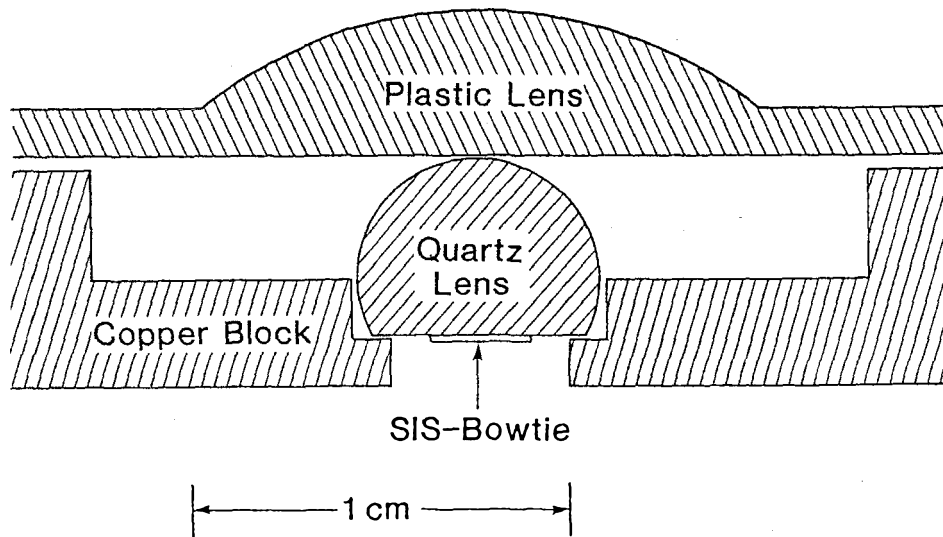
Figure 4.9 Cross section through Bowtie 1. The first mixer block is made so that the quartz hyperhemisphere is located in a hole drilled in the copper mixer block, and held in place by the plastic lens, which is attached to the front of the mixer block. IF connections to the SIS are not shown in this figure.

refrigerator may be considered to be perfectly heat sunk, at least for temperatures (1-5 K) and thermal power levels (milliwatts) involved in mixer design.

A cross-section through the first mixer block (Bowtie 1) constructed is shown in fig. 4.9. A photograph of Bowtie 1 is shown in fig 4.10. The block is basically two-sided. Radiation is incident from the front, so the front side of the block serves to mount the lenses for the mixer. For Bowtie 1, the quartz hyperhemisphere is placed in a hole which is drilled nearly through the mixer block. The hyperhemisphere is held in the block by direct contact with a plastic (Teflon or polyethylene) lens which is mounted with spring-loaded bolts to the mixer block. The hole in the mixer block must be made slightly oversize since copper will shrink more on cooling than quartz will. In Bowtie 1, indium was pressed around the base of the hyperhemisphere to mechanically immobilize it, and to improve thermal conduction to it.

Mounted on the back of the mixer are the IF circuit and the SIS itself. The IF circuit described in the previous section is used, except that the insulator for making the capacitor in Bowtie 1 is mylar. (The use of crystal quartz for that insulator is an improvement made in Bowtie 2.) The SIS, which is on a 3 x 3 x .25 mm fused quartz substrate, is laid on the back of the quartz hyperhemsiphere through a hole of sufficient diameter drilled from the back of the block. By making this hole just large enough
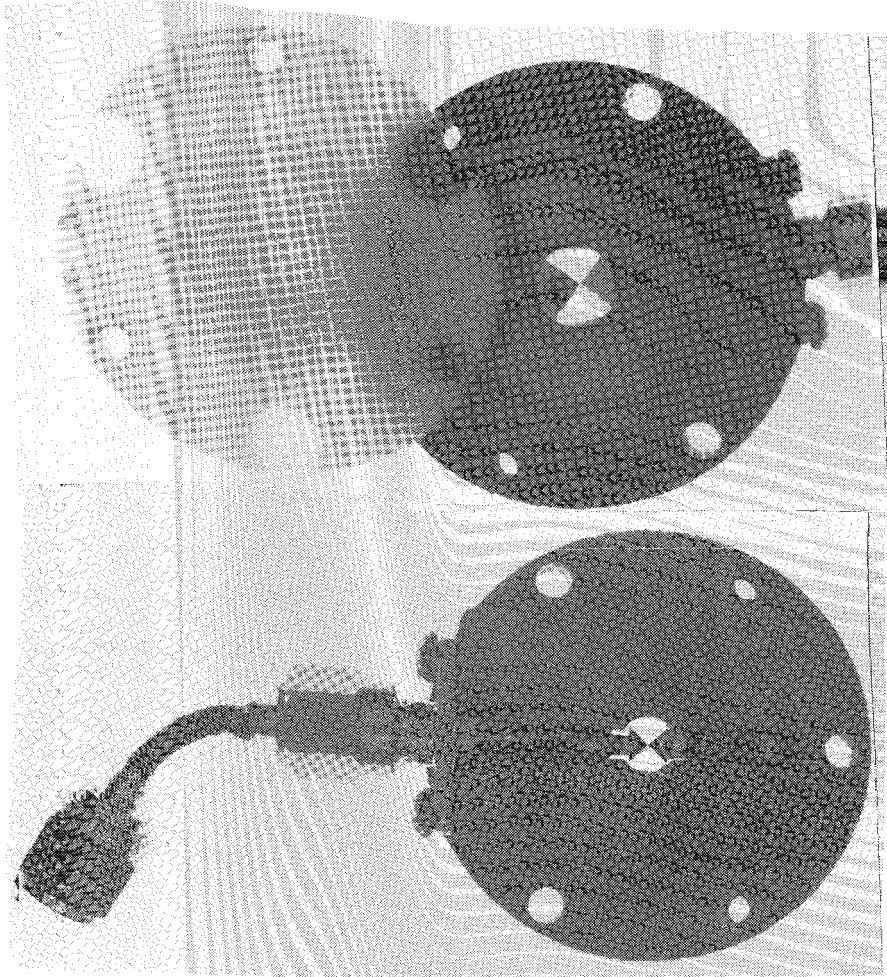
Figure 4.10 Photographs of Bowtie 1. (a) From the RF side, the plastic lens is shown out of place so that the SIS-bowtie can be seen through the fused quartz hyperhemisphere. (b) From the other side, the ground and IF connections to the SIS-bowtie can be seen. These connections are made from springy metal to hold the SIS against the hyperhemisphere.

to clear the SIS-on-quartz, it can be used for locating the SIS relative to the hyperhemisphere with reasonable accuracy. The SIS is held against the hyperhemisphere by two electrodes made from springy beryllium-copper shim stock. One electrode is attached directly to the block to provide a ground to one side of the SIS. This electrode should also present a high thermal conductivity path to the mixer block for cooling the SIS. The other electrode is insulated from the block by a sheet of mylar. It is trimmed to size to provide about 1 pF capacitance, as required for the IF circuit.

Cooling of the junction to the temperature of the mixer block was achieved only when indium was painstakingly pushed into all the gaps between the quartz hyperhemisphere and the mixer block. It was also found necessary to place a sheet of black polyethylene between the hyperhemisphere and

Plastic Lens

Copper
Block

Quartz
Lens

SIS-Bowtie

Quartz Flat

|————1 cm ————|

Figure 4.11 Cross section through Bowtie 2. The hyperhemisphere in this mixer is glued to a thin quartz flat, which is indium-soldered to the copper mixer block.

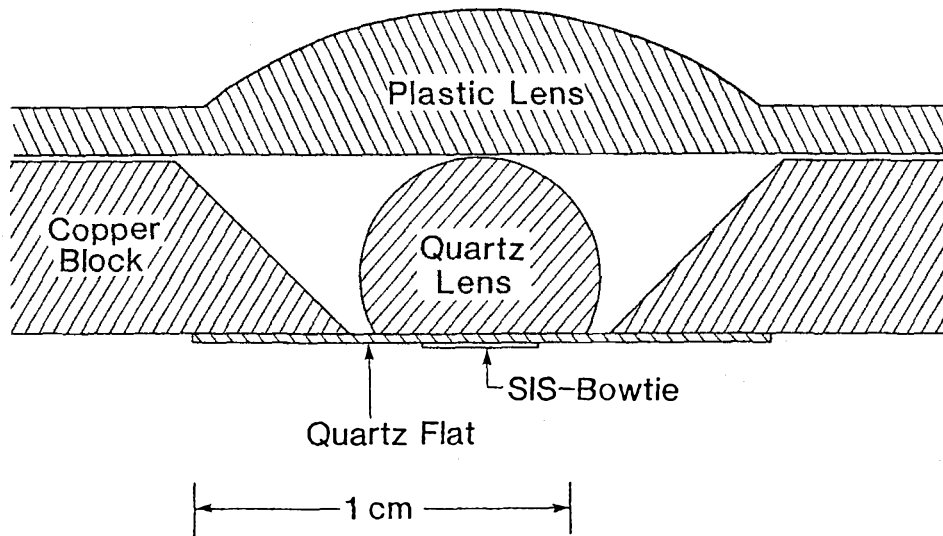the Teflon front lens which held the hyperhemisphere into the block. The tentative conclusion is that thermal radiation from the approximately 100 K radiation shield in the test Dewar is sufficient to heat the fused quartz hyperhemisphere above mixer block temperature unless that radiation is blocked by black polyethylene on the cold stage of the cryostat.

The second mixer block (Bowtie 2) differs from the first primarily in the way in which the quartz hyperhemisphere is attached to the mixer. As shown in fig. 4.11, the hyperhemisphere is glued to a flat piece of quartz, which is soldered to the copper mixer block. Indium is used for the quartz-copper solder joint, lead-tin solder does not work. The hyperhemisphere is glued to the flat with superglue (Eastman 910 adhesive).

Their are a number of advantages to this mounting scheme over that used in Bowtie 1. The metal sides of the hole in which the hyperhemisphere fits in Bowtie 1 are absent in Bowtie 2. The beam pattern of Bowtie 1 may have been affected by reflection or diffraction from the walls of this hole. It is also possible in Bowtie 2 to change the size of the hyperhemisphere. In Bowtie 1, a larger hyperhemisphere would not fit in the hole, while a smaller one would not have been held in place by the front lens. It had initially been expected that the mounting scheme in Bowtie 2 would make for very good junction cooling.

It was intended that the flat piece of quartz to which the hyperhemisphere is glued could be made

from crystalline quartz, which has high thermal conductivity. Indium soldering that quartz to the mixer block would provide a high thermal conductivity connection between the mixer block and the quartz flat. Thus the SIS-on-quartz would be laid flat against a well heat-sunk piece of crystal quartz, and radiation falling on the hyperhemisphere could not heat up the SIS. However, it was discovered that fused quartz and crystalline quartz shrink by different amounts when cooled. When the fused quartz hyperhemisphere is glued to the crystal flat, the quartz hyperhemisphere is broken by differential contraction on cooling. Thus, it has been necessary to use fused quartz flats in Bowtie 2, since all of the hyperhemispheres are made from fused quartz. To achieve efficient cooling of the SIS, it is necessary, as in Bowtie 1, to place a sheet of black polyethylene between the plastic front lens and the hyperhemisphere.

Both bowtie mixers have been built with hyperhemispheres with radii of about 3.2 mm. Referring to fig. 4.1, this should result in a beam with a half width of about 7 mm at the front of the plastic lens. This matches reasonably well to the beams which exit the feedhorns of waveguide-feedhorn mixers that are used at OVRO (Sutton, 1983; Woody, Miller and Wengler, 1985). As a result, it has been possible to use test Dewars originally constructed for use with these other mixers, but more importantly, it has simplified the testing of the bowtie mixers at OVRO.

4.6 Bowtie Receiver Lab Measurements

The true test of a low-noise receiver for radioastronomy is to put it on a telescope and look at spectral lines from known astronomical sources. The signal to noise ratio of those measurements can be determined, and a system noise temperature can be assigned to the whole telescope-receiver-atmosphere system. However, the first step in testing a receiver is to measure some of its properties in the lab. The receiver does not typically go straight to a telescope because 1) time on a telescope is at a premium, and therefore nearly completely given over to already proven receivers, and 2) performance on the telescope will be much better if the receiver is properly coupled to it, which requires knowing a lot about the receiver. The SIS receiver is more difficult to test in the lab than Schottky diode receivers. This is primarily due to noise and instabilities associated with the Josephson effect in the SIS.

The receiver set-up for laboratory measurements is shown in fig. 4.12. LO is injected into the signal
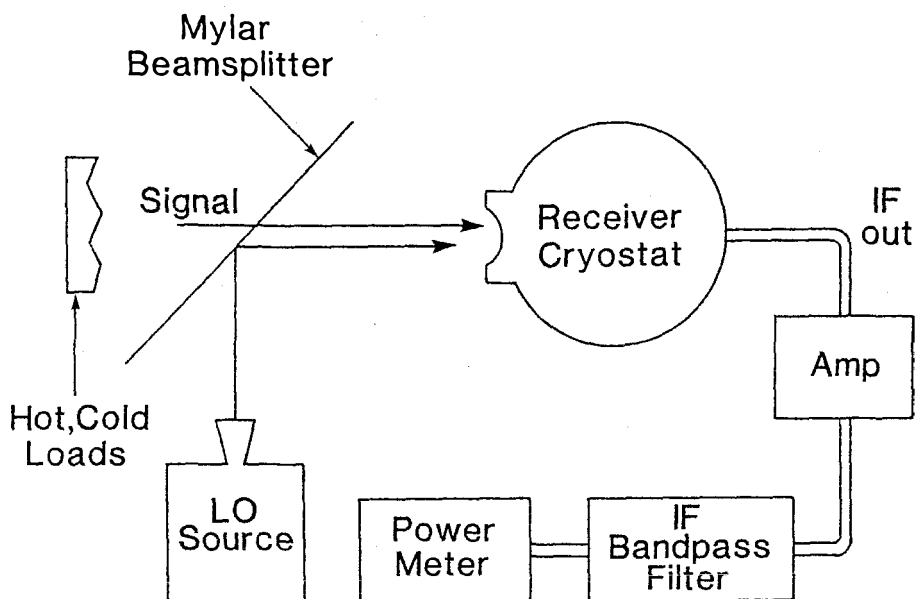
Mylar
Beamsplitter

Signal

Receiver
Cryostat

IF
out

Amp

Hot,Cold
Loads

LO
Source

Power
Meter

IF
Bandpass
Filter

Figure 4.12 Receiver test set-up. The LO is combined with the test signal by partial reflection from a 25 μm thick mylar sheet. The SIS-bowtie mixer and the first IF amplifier are in the receiver cryostat. The mixer output is further amplified and filtered outside the cryostat, and then measured with a power meter.

path by reflection off a 25 μm thick mylar beam-splitter. This reflects $\sim$ 1% of the power from the LO source into the cryostat. A thicker beam-splitter is used when higher LO reflection is required, but this increases the reflection loss which the signal suffers as it is transmitted through the mylar. The LO and signal are mixed in the cryostat, and the first stage of IF amplification is done in the cryostat. Outside the cryostat, the IF is further amplified, and passed through a filter to remove out of IF band power. Finally, the IF power is detected in a power meter.

The receiver cryostat layout is shown in fig 4.13. The RF radiation passes through a mylar vacuum window on its way into the cryostat. The cryostat has a 100 K radiation shield, a single crystal quartz window is mounted in this shield. The quartz blocks most of the 300 K radiation from outside the cryostat since it is lossy at infrared frequencies, but it passes near-millimeter radiation with low loss. The quartz is coated with black polyethylene which helps block infrared, and also acts as an imperfect anti-reflection coating. The bowtie-SIS mixer is mounted on the cold plate, which is directly cooled by liquid helium in the cryostat. The IF output of the mixer passes through an isolator, and is then amplified by a GaAsFET amplifier, both of which are mounted on the cold plate. A superconducting coil is mounted directly behind the mixer block. By passing a current through this coil, a magnetic field
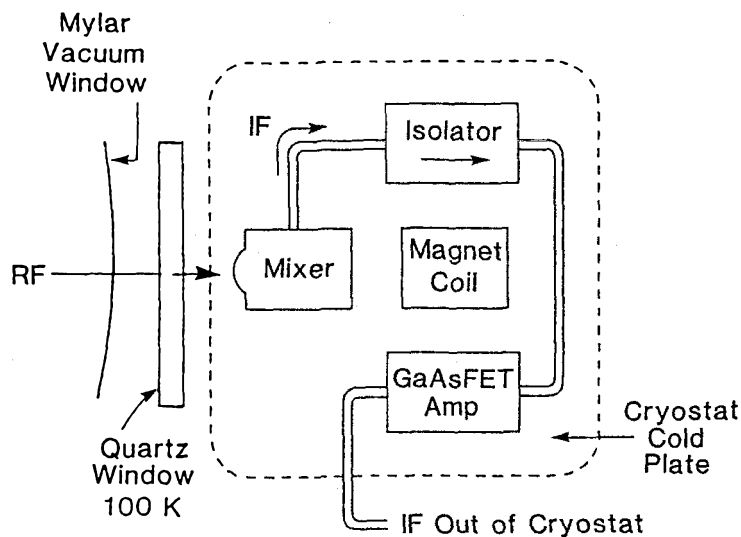
Figure 4.13 Receiver cryostat. RF passes through a mylar vacuum window and a Quartz window at 100 K on its way to the bowtie mixer. The mixer, and the first stages of IF amplification are mounted on the cold plate of this liquid helium cryostat.

is produced which partially suppresses Josephson effect currents in the SIS (Tucker and Feldman, 1985; Barone and Paternò, 1982).

The isolator-amplifier combination has performance which is completely characterized by a minimum noise temperature, T_{IF0}, a maximum gain, Γ_{IF0}, and an input impedance, Z_{IF}. The input impedance of the combination is simply the transmission line impedance of the isolator, 50 Ω for the standard elements used here. The minimum noise temperature and maximum gain for the combination occur when the output impedance of the mixer, Z_M, is matched to the isolator-amplifier input impedance of 50 Ω. Isolator-amplifier response when $Z_M \neq 50$ Ω is

$$\Gamma_{IF} = \Gamma_{IF0} \frac{4 R_M R_{IF}}{|Z_M^* + Z_{IF}|^2}$$

$$T_{IF} = T_{IF0} \frac{|Z_M^* + Z_{IF}|^2}{4 R_M R_{IF}}.$$

(4.6.1)

R_M and R_{IF} are the real parts of Z_M and Z_{IF} respectively. Both gain and noise degradation are due to the mismatch between the mixer and the isolator. Without the isolator, gain would vary with mismatch as in (4.6.1), but noise would have a more complicated behavior.

The isolator-amplifier gain and noise can be measured by using the SIS as a noise source (Woody, Miller and Wengler, 1985). Consider the SIS dc biased at $V_0 > V_{GAP}$. The current flowing across the SIS has shot-noise statistics just as the current in a Schottky diode or in a field-emission vacuum tube
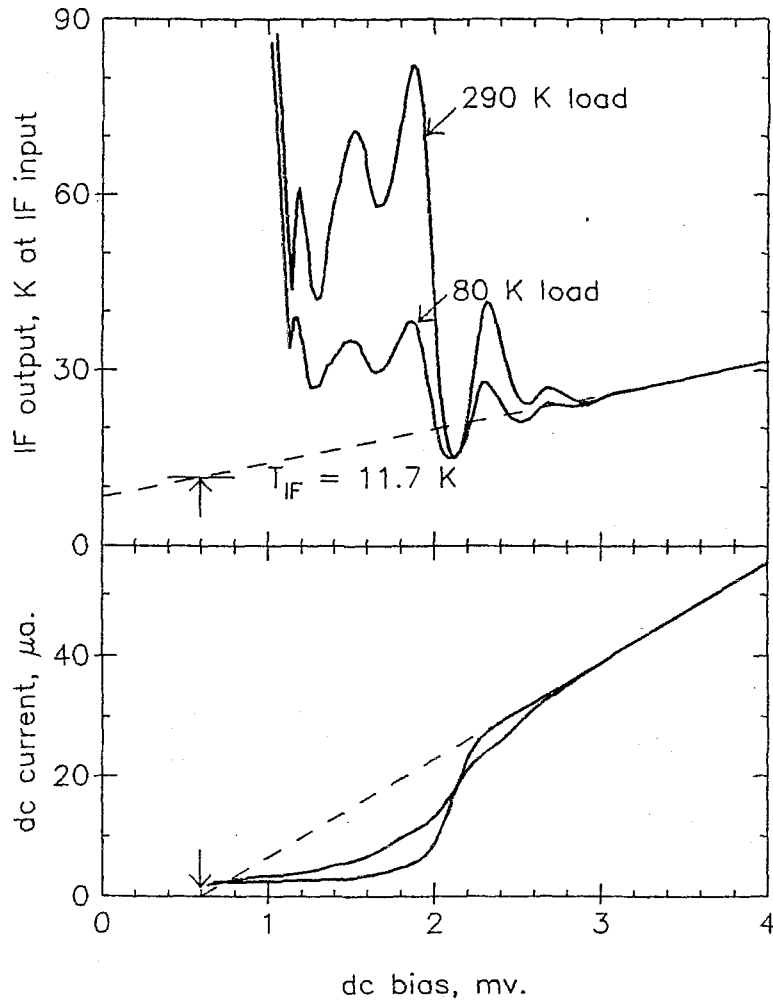
Figure 4.14 *I-V* and IF power vs. dc bias voltage. Below 3 mV, heterodyne response is seen, this is for a waveguide mixer at 95 GHz (Woody, Miller and Wengler, 1985). Above 3 mV, there is no heterodyne response, and the SIS shot noise is used to calibrate the IF amplifier chain as described in the text.

does. IF power and the *I-V* curve are shown in fig. 4.14. The equation for the *I-V* above 3 mV is linear,

$$I_0 = G(V_0 - V_I) \tag{4.6.2}$$

where G is the dynamic admittance of the *I-V* in the linear region, and V_I is non-zero because I_0 does not extrapolate to zero at $V_0 = 0$. The standard expression for the shot noise i in a current I_0 is

$$\langle i^2 \rangle = 2e I_0 B \tag{4.6.3}$$

where B is the bandwidth in which the fluctuations are measured. The standard expression for the Johnson, or thermal noise coming from a resistor of admittance G in thermal equilibrium is

$$\langle i_T^2 \rangle = 4 k_B T G B. \tag{4.6.4}$$

The SIS shot noise source can be assigned a "shot temperature" T_{SHOT} by combining these two expressions. Using (4.6.2) for I_0, the biased SIS looks like a thermal source of temperature

$$T_{SHOT} = \frac{e}{2k_B} \left(V_0 - V_I \right)$$
$$= \frac{5.8 \text{ K}}{1 \text{ mV}} \left(V_0 - V_I \right) \tag{4.6.5}$$

This result, based simply on the assumption that the SIS has shot noise in its dc current, can also be derived from the expressions used by Tucker in his noise theory (Tucker, 1978; Tucker and Feldman, 1985).

The reading on the power meter at the end of the IF amplifier chain, P_M, is linearly related to the noise power at the output of the mixer,

$$P_M = \alpha \left(T_{OUT} + T_{IF} \right) \tag{4.6.6}$$

where the mixer output power is $k_B T_{OUT} B$. Both T_{IF} and α can be determined through measurement of P_M as a function of V_0.

This method of calibrating the IF amplifier chain does depend on 1) finding a sufficiently linear portion of the $I\text{-}V$ to use, and 2) the theory of current conduction in an SIS being correct. The first requirement is generally met in our experiments, although other experimenters have claimed to get unbelievable results when they apply this method. This may be because the isolator between the SIS and the first IF amplifier makes our system less sensitive to small deviations from linearity in the $I\text{-}V$. The second requirement has yet to be tested directly, and could easily be true for some SISs, but not all. For our junctions, however, the T_{IF} calculated in this fashion typically agrees quite well with IF amplifier noise measurements made with standard techniques.

This method, as described, is valid when a single SIS is used as the mixing element. For two SISs in series, there is no consensus on whether the constant of proportionality, 5.8 K/mV, in (4.6.5) should be halved (Tucker, 1983), multiplied by $\sqrt{2}$ (van Kempen et al., , 1981), or left alone. Bowtie 2 was tested with a detector which consists of two SISs in series. The characterization of the IF amplifier chain for these measurements suffers from uncertainty about the correct way to deal with the shot noise from these SISs in series.

The fundamental measurement of mixer/receiver performance is to measure the IF power as a function of the input signal power. Blackbodies provide power $k_B T_S B$ at the mixer input, where B is the bandwidth in which the radiation is measured, and

$$T_S = \frac{h\nu/k_B}{e^{h\nu/k_B T_L} - 1}$$

(4.6.7)

is the Planck-corrected "signal temperature" of a blackbody with physical temperature T_L, at frequency ν. Keeping terms to first order in ν, the Rayleigh-Jeans blackbody signal temperature is

$$T_S = T_L - h\nu/2k_B \qquad \text{for } h\nu \ll k_B T_L$$

(4.6.8)

Neglecting the small correction proportional to $h\nu$ will result in calculated receiver noise temperatures which are low by an amount on the order of $h\nu/k_B$. This amount is only a few percent of the receiver temperatures reported here, but in some SIS receivers the total receiver noise temperature is within an order of magnitude of this value, so it should not be neglected.

Measurements are made with a room temperature blackbody, assumed to have $T_L = 290$ K, and a blackbody cooled with liquid nitrogen, assumed to have $T_L = 80$ K. These are called the "hot load" and the "cold load" respectively. The receiver noise temperature depends on the ratio of the IF power measurements with hot and cold loads at the mixer input,

$$T_R = \frac{T_H - T_C}{Y - 1} - T_C$$

(4.6.9)

where Y is the ratio between IF power measurements with hot and cold loads applied, and T_H and T_C are the signal temperatures (4.6.7) of the hot and cold loads. The calculation of receiver noise temperature neither requires nor yields any information on the separate contributions to gain and noise of the SIS mixer and the IF amplifier chain.

To derive the mixer gain and noise from the IF power measurements, (4.6.6) is used to determine the mixer output temperature T_{OUT} as a function of the input signal, T_S. The mixer gain Γ_M and noise temperature T_M are then determined by the linear relationship

$$T_{OUT} = \Gamma_M \left(T_M + T_S \right).$$

(4.6.10)

The parameters in (4.6.6) are calculated based on what is really only a theoretical model of noise in the SIS. It is more likely that mixer gain, Γ_M, is estimated improperly by this method than that mixer noise is. The model prediction that the linear portion of the I-V should be associated with a linear SIS noise power is verified in all mixer measurements, of which fig. 4.14 shows one example. It is difficult to conceive of a physical system in which a noise power which is proportional to the current I_0 through the SIS should extrapolate to any other value than zero when I_0 is extrapolated to zero. However, it is relatively easier to imagine that physical effects not included in the theory cause a constant of proportionality other than 5.8 K/mV in (4.6.6). From this reasoning, it follows that the intercept, V_I, is more reliably known than is the slope of the line in K/mV. Just as the receiver temperature T_R depends only on the ratio of IF powers with hot and cold loads applied, T_M depends on the ratio of mixer output temperatures. This ratio is unchanged if values other than 5.8 K/mV are used in (4.6.6). However, calculated mixer gain, Γ_M, varies inversely as the assumed constant of proportionality. So, T_R is the least model dependent of the parameters reported here, T_M relies on only one additional assumption about SIS shot noise, and Γ_M depends on the accuracy of both slope and intercept in (4.6.6).

Measurements of the bowtie receiver in the lab are intrinsically double sideband (DSB). Mixer IF output signal at the output frequency ν_0 can be due to downconversion of RF input signal at two different frequencies, $\nu_{LO} + \nu_0$, the upper sideband (USB), and $\nu_{LO} - \nu_0$, the lower sideband (LSB). The hot and cold blackbody signal sources used in the laboratory measurements provide equal amounts of input power at each sideband. If the receiver responds equally to each sideband, then the gain and noise measured with hot and cold loads are called (DSB) values. All gains and noises reported here are DSB values unless otherwise noted. For a mixer with equal response in each sideband, the corresponding single sideband (SSB) gain and noise are related to the DSB values,

$$\Gamma_M^{SSB} = \Gamma_M/2$$

$$T_{M,R}^{SSB} = 2T_{M,R}.$$

(4.6.11)

The bowtie mixers are almost certainly DSB, so (4.6.11) shows how to estimate their SSB performance from the DSB measurements reported here.

To measure mixer and receiver performance at some frequency, an LO at that frequency must be provided. The LO power causes a voltage V_{LO}, at frequency ν_{LO}, across the SIS. For efficient mixing,

V_{LO} must be about $h\nu_{\text{LO}}/e$. The LO power that is absorbed in the SIS when this voltage is produced could be calculated from Tucker's theory (Tucker, 1978). However, there is a simpler calculation which yields the same result, and emphasizes the fact that SISs are photon counters. If the SIS is at some fixed dc bias voltage on the first photon step below the gap, the dc current through the junction rises linearly with applied LO power for small LO powers. When the current rises to about 1/4 of the value it would have if the SIS was dc biased at just above V_{GAP}, the photo-response of the SIS begins to saturate, *i.e.*, the current rises more slowly with additional applied power. Optimum mixing occurs when the LO power is just above this saturation power. So the current that must flow through the SIS due to absorbed LO photons is about $G_N V_{\text{GAP}}/3$. This is about 15 μA for a 50 Ω lead alloy SIS. Tucker has shown (Tucker, 1978) that an SIS has a current responsivity of "one electron per photon" as discussed in chapter 2. The optimum absorbed LO power in an SIS is found by equating the electron flux acros the SIS to the photon flux which produces it,

$$P_{\text{ABS}} \approx \frac{G_N V_{\text{GAP}}}{3} \frac{h\nu_{\text{LO}}}{e}$$

$$= 6 \text{ nW} \frac{\nu_{\text{LO}}}{100 \text{ GHz}} \quad \text{for a 50 } \Omega \text{ lead alloy SIS.} \tag{4.6.12}$$

The required power scales linearly with G_N, so a 25 Ω junction must absorb twice as much LO power. If two 25 Ω junctions in series are used for mixing, as is the case for the Bowtie 2 measurements reported here, the necessary absorbed power will be four times the amount in (4.6.12).

For the Bowtie 1 experiments, LO power was generated by using a Klystron tuned to 116.5 GHz to drive a Schottky-diode cross-guide frequency multiplier (Schneider, 1982). Sufficient power to drive a single 50 Ω SIS was available up to the fourth harmonic, 466 GHz, with this system. For the Bowtie 2 experiments, a Gunn-diode oscillator at 75 GHz drove a Schottky-diode multiplier, to provide sufficient LO power up to the fourth harmonic, 300 GHz. 420 GHz LO was supplied by multiplying a Klystron oscillating at 140 GHz. LO at 525 and 761 GHz was supplied by a far infrared laser built by Dan Watson.

An example of the raw data for Bowtie 1 measured at 466 GHz is shown in fig. 4.15. Results are shown both with and without magnetic field applied to the SIS junction. When no magnetic field is imposed on the SIS, the IF power has a steep slope in the dc bias range 1.9 mV $< V_0 <$ 2.2 mV.

The IF power with cold load applied shows sharp structure at $V_0 = 1.93$ mV. It is impossible, from this data, to say anything sensible about heterodyne performance. However, when magnetic field is applied to the SIS, The IF power curve becomes flat over a region of .15 mV width, just below the structure at $V_0 = 1.93$ mV. One can quantitatively determine an IF power difference between hot and cold loads in this case, and mixer and receiver performance can be calculated based on this difference.

The structure at 1.93 mV, and at other voltages indicated in the figure, are due to the ac Josephson effect, described in section 1.2. The arrows labelled J2 and J3 in fig. 4.15 show the voltages at which the Josephson frequency, (1.2.3), is exactly twice and three times the LO frequency. Structure in the I-V or IF power curve at these voltages are due to mixing of the Josephson and LO oscillations.

The large rise in IF power below 1.9 mV with no magnetic field, and below 1.5 mV in the presence of magnetic field is also attributed to Josephson effect currents. Its cause is the chaotic effects associated with ac Josephson currents. In the dc I-V, fig. 1.3b, this chaos resulted in a region of forbidden dc bias voltages, between 0 and V_D. With LO applied, this chaos produces a large output noise power from the SIS. The difference between this chaotic power output when the mixer signal is a hot or cold load is almost certainly not due to linear mixing of the LO and signal radiation.

Magnetic field is applied to the junction in an attempt to suppress Josephson currents. In larger area SISs than those used here, it is possible to completely eliminate Josephson currents with a magnetic field on the SIS (Barone and Paternò, 1982). However, in the SIS illustrated here, the Josephson currents are lowered by only a factor of two with the application of field. Even with field applied, Josephson structure in the I-V and IF are still apparent. However, the value of V_0 at which the SIS is chaotic is lowered by about .5 mV, allowing heterodyne response to be observed.

The SISs used in the testing of Bowtie 2 had much better quality I-Vs, and there is more effective suppression of the Josephson effect than for the SIS in Bowtie 1. Fig. 4.16 shows raw data for Bowtie 2 at 225 GHz. The detector in Bowtie 2 consists of two SISs in series. If the two SISs were identical, the series array would behave just like a single SIS, except the voltage scale in the problem would be twice as large. This is essentially what is seen in the figure. This data shows a larger non-chaotic region than the data in fig. 4.15. For this reason, the results from bowtie 2 are less likely to be contaminated
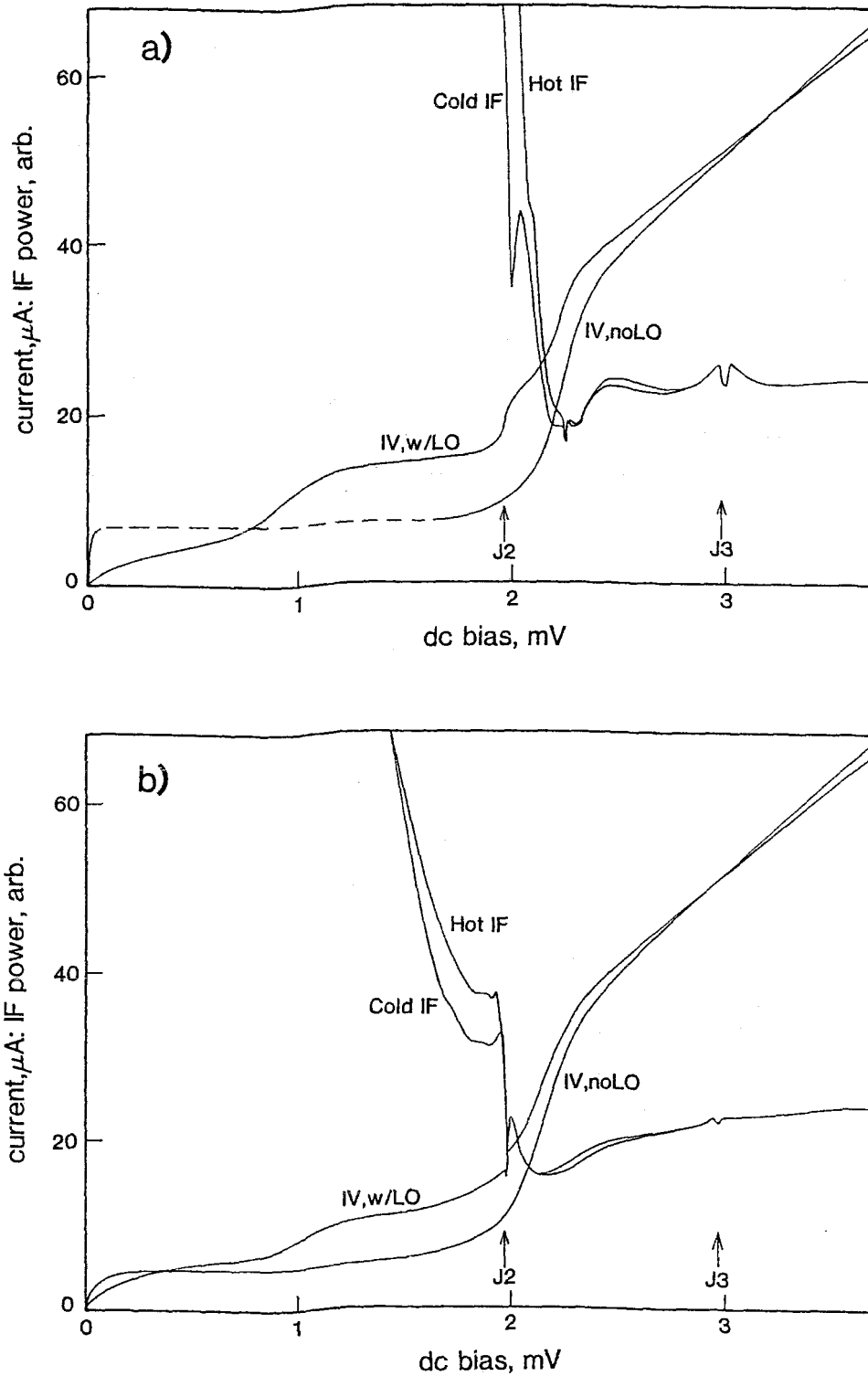
Figure 4.15 *I-V* and IF power at 466 GHz in Bowtie 1. a) With no magnetic field applied, the IF power rises quickly as the dc bias is lowered, reliable heterodyne results seem unlikely. b) With magnetic field applied, their is a flat region in the IF power curve in which heterodyne response can be accurately measured. The voltages marked J2 and J3 are where the ac Josephson frequency is respectively twice and three times the LO frequency.
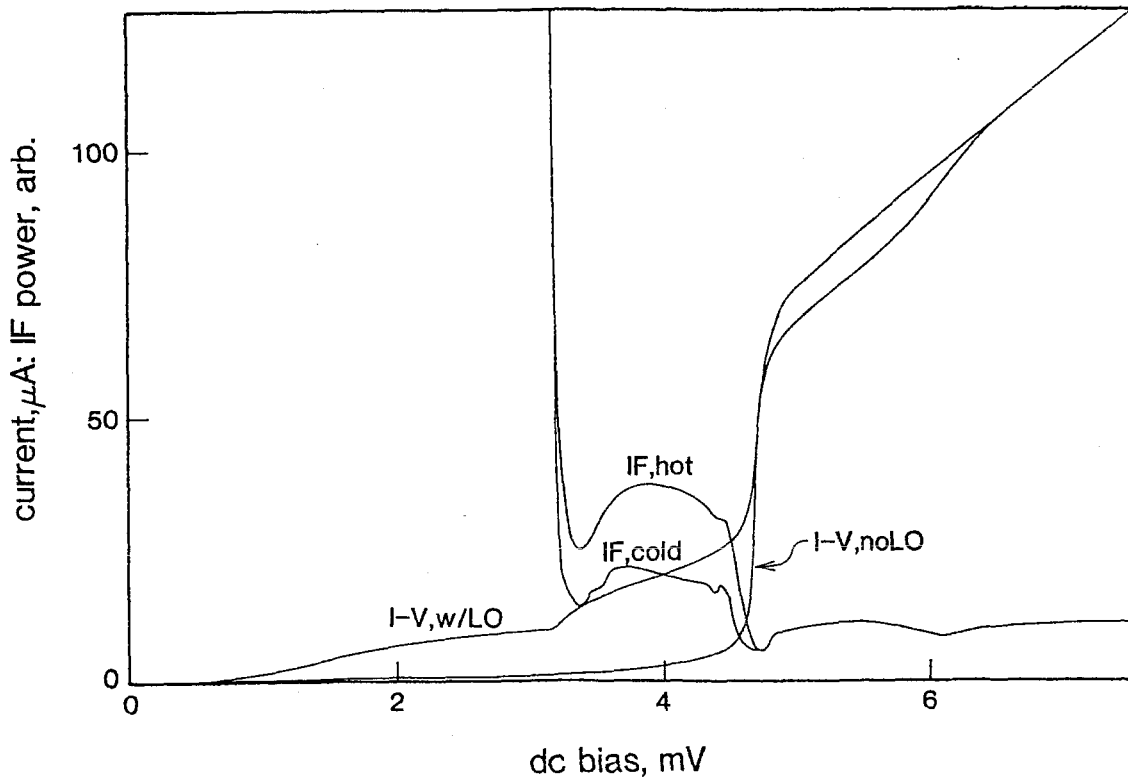
Figure 4.16 *I-V* and IF power at 225 GHz in Bowtie 2. The IF power is measured with a small magnetic field applied. A broad, flat region of heterodyne response is seen above the high IF power region associated with chaotic noise in the SIS.

by non-heterodyne response. The results for Bowtie 2 are generally better than those for Bowtie 1, presumably because the *I-V* for Bowtie 2 is more nearly ideal.

The mixer and receiver results for Bowties 1 and 2 are listed in tables 4.2 and 4.3. They are plotted in fig. 4.17. The data is not corrected in any way for losses in the signal path between the blackbody signal source and the SIS. Performance both with and without magnetic field applied are shown. The major effect of applying magnetic field seems to be to lower mixer gain. The implication is that Josephson currents are part of a useful gain mechanism for this mixer. Examination of the mixer temperature results show that the Josephson currents do not necessarily produce extra mixer noise, as has been postulated (Tucker and Feldman, 1985). The gain measurements for Bowtie 2 in table 4.3 are difficult to estimate because two SISs in series are used as the detector in these experiments. The gains reported here are calculated as though a single SIS detector had been used. These gains would go up by a factor of $\sqrt{2}$ (1.5 dB) or 2 (3 dB) if one or the other of the possibilities mentioned above for noise

Table 4.2 – Bowtie 1 Results (DSB)

LO, GHz	T_{REC}, K	T_{MIX}, K	Gain, dB	Mag. field
116	173	94	−6.6	no
233	263	179	−6.9	no
233	365	193	−9.4	yes
349	410	317	−6.7	no
349	639	329	−11.9	yes
466	741	434	−11.7	yes

Table 4.3 – Bowtie 2 Results (DSB)

LO, GHz	T_{REC}, K	T_{MIX}, K	Gain*, dB	Mag. field
150	198	135	−4.2	no
150	173	89	−5.5	yes
225	163	109	−3.6	no
225	165	87	−5.2	yes
300	498	421	−5.1	no
300	405	269	−7.6	yes
420	492	273	−9.6	yes
525	1160			yes
761	1360			yes

* Gain is uncertain, see text.

in series arrays had been used.

Because of the possibility of non-heterodyne mechanisms for IF power modulation, a technique for relative calibration of mixer gain was used to increase confidence in the performance numbers reported above. The LO for most of the above experiments was an harmonic of a 75 to 140 Ghz oscillator. The harmonic was produced by pumping a Schottky-diode with the fundamental frequency, the desired harmonic is then coupled out through waveguide filters. For the purpose of gain calibration, a 1.5 GHz signal is also imposed on the diode. Sidebands at $\nu_{LO} \pm 1.5$ GHz are then produced on the Schottky. The 1.5 GHz power level is kept low enough so that the sideband power is much less than the LO power at ν_{LO} which is coupled out of the Schottky.

These sidebands can be used as a test signal of unknown absolute power. By monitoring the mixer output on a spectrum analyzer, changes in mixer gain can be measured as dc bias voltage, V_0, is changed. The results of a measurement of Bowtie 1 at 350 GHz by this method are shown in fig. 4.18. Because the calibration signal is reflected off the mylar beam splitter with the LO, it is possible to do these gain measurements while illuminating the signal port of the mixer with hot (290 K) or cold (80 K) blackbody
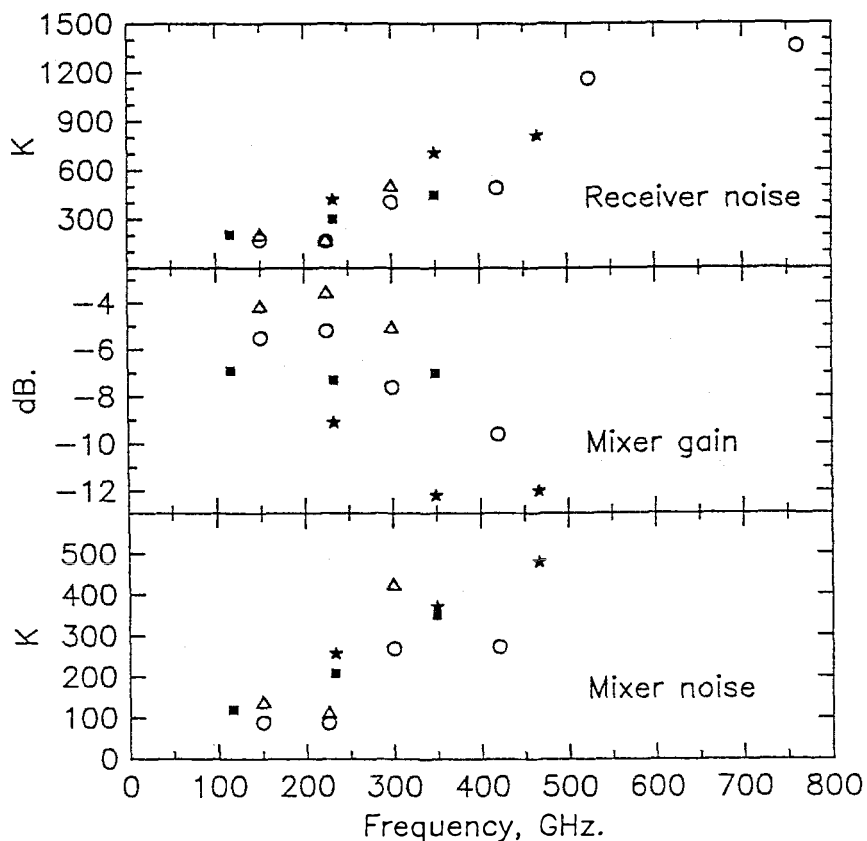
Figure 4.17 Mixer and receiver double sideband performance vs. LO frequency. ★ – Bowtie 1 with magnetic field applied. ■ – Bowtie 1 with no magnetic field. △ – Bowtie 2 with no magnetic field. o – Bowtie 2 with magnetic field. These are the same data as in tables 4.2 and 4.3.

radiation. In this way, saturation of mixer gain can also be measured. Finally, it is possible to turn the magnetic field on and off while observing the downconverted sidebands.

The curve of mixer gain vs. V_0 inferred from measurements with hot and cold load can be plotted on top of the relative gain vs. V_0 curves measured with sidebands. The absolute gain scale for the sideband measurements has been chosen so that the rms difference between sideband gain and hot/cold measured gain is minimized for the data taken with magnetic field applied. As can be seen, gain measured by the two methods has the same shape to within 1 dB. Hence, it is reasonable to conclude that the hot/cold measurements are predominantly measuring heterodyne response.

Without magnetic field, the hot/cold measurements may overestimate actual mixer gain by as much as about 3 dB. However, the mixer gain is significantly higher without magnetic field, even when measured with sidebands. In fact, this effect of higher gain was seen at the three frequencies at which
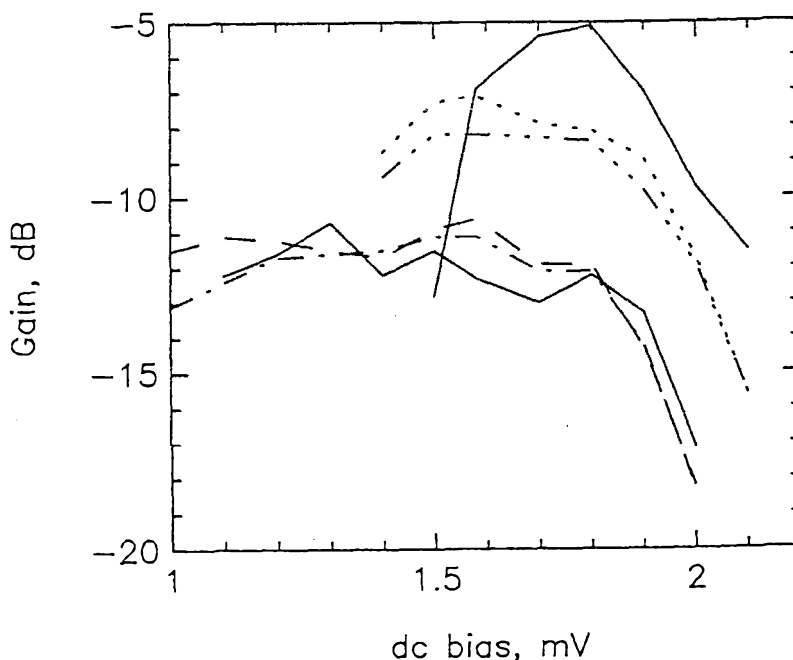
Figure 4.18 Gain measured with sidebands. The measurements were made using Bowtie 1 at an LO frequency of 350 GHz. The dashed line is measured with cold load and magnetic field. The dot-dash line, with hot load and magnetic field. Dotted line, with cold load, no magnetic field. Dash-dot-dot-dot line, with hot load, no magnetic field. The lower and upper solid curves are the gains inferred from hot/cold load measurements, with and without magnetic field, respectively.

sideband measurements were done. Measured in Bowtie 1, mixer gains improved with removal of magnetic field by 2.6 dB at 233 GHz, by 4 dB at 350 GHz, and by 6 dB at 466 GHz. The possible positive effects of Josephson currents on submillimeter mixing results deserve more extensive study than they have been given here.

Information about mixer saturation is also obtained from the sideband measurements. In general, for signal power levels above some permissible maximum, heterodyne response is saturated, IF power rises by less than 1 dB for each additional 1 dB of signal applied. Sideband power levels in this experiment are deliberately chosen so that they are a small fraction of the thermal power load on the mixer. By looking at the sideband gain as hot and cold loads illuminate the mixer, gain compression due to these different thermal powers are observed. In fig. 4.18, the gain compression is less than .5 dB for $V_0 > 1.2$ mV. For the higher gains that occur when no magnetic field illuminates the mixer, gain compression of about 1 dB is observed.

The receiver temperature results reported for Bowtie 2 are compared with the best results achieved
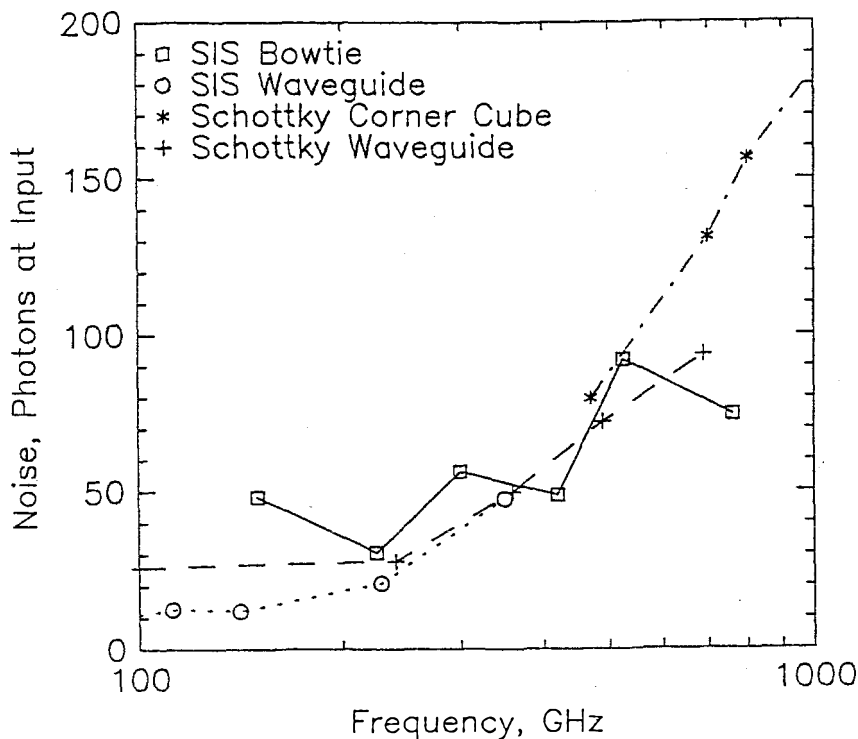
Figure 4.19 Comparison of receiver noises for different technologies. Each waveguide point is measured in a different receiver. The SIS bowtie numbers are from a single receiver (Bowtie 2). The Schottky corner cube numbers are from a single receiver (Betz, 1987; Zmuidzinas, 1987). Each Schottky waveguide datum is from a different receiver (Predmore et al., 1984; Erickson, 1985 & 1987). Each SIS waveguide datum is from a different receiver (Räisänen et al., , 1986; Pan et al., , 1983; Ibruegger et al., , 1984; Ellison and Miller, 1987; Theis DeGrauw, private communication).

for Schottky diode and SIS low-noise receivers in fig. 4.19. The receiver temperatures are divided by the quantum lower limit, so that as described in chapter 2, noise is quoted in photons instead of degrees Kelvin. The theoretical limit of one noise photon is hardly even approached by real receivers. Even ten times the quantum limit represents higher sensitivity than all but a few of these receivers. The SIS receivers are seen to enjoy a slight advantage over Schottky receivers over most of the frequency range. At millimeter wavelengths, waveguide-mounted detectors give the best results. At submillimeter wavelengths, receivers are not as sensitive, even when that sensitivity is expressed in photons. This is mainly due to the difficulties of building waveguide structures with sufficient accuracy for these very short wavelengths. At the highest frequencies, "open structure" mixers such as the Schottky-corner-cube and the SIS-bowtie are more sensitive.

4.7 Bowtie Performance on the Telescope

Both mixers, Bowtie 1 and Bowtie 2, have been tested on a 10.4 m diameter telescope at Caltech's Owens Valley Radio Observatory (OVRO). The maximum frequency of these tests, however, was only 260 GHz. Bowtie sensitivity up to this maximum frequency was good, but not as good as the SIS-waveguide results obtained in this same frequency range (Sutton et al., 1985). Perhaps most importantly, it was shown that the receiver can be calibrated by using hot and cold blackbodies as known signal sources. It was also shown that the bowtie mixer beam pattern coupled to the telescope with about 60% efficiency, as compared to about 90% for waveguide-feedhorn mixers. Finally, the aperture efficiency of the telescope when illuminated by the bowtie mixer beam was shown to be excellent at 115 GHz, and probably as good as with waveguide mixers at 230 GHz.

The bowtie mixers were found to be usable at OVRO as drop-in replacements for the waveguide based SIS mixers (Woody, Miller and Wengler, 1985) which are usually used there. Most importantly, calibrating these receivers with hot and cold loads, as described above, was found to result in the correct measurement of known line intensities at 115 and 230 GHz. Measurements of the line intensities of two spectral lines of the CO molecule are shown in fig. 4.20. The measurements are of spectral intensity in units of "antenna temperature", T_A (Krauss, 1986). The bowtie mixer finds the same intensities for these lines as other receivers at OVRO have found. The conclusion is that at 115 and 230 GHz, the bowtie-SIS heterodyne response is correctly calibrated by use of hot and cold loads.

The mixer is coupled to a telescope at OVRO as shown in fig. 4.21. As is usual for millimeter wavelength telescopes, there are a number of mirrors between the receiver and the primary mirror of the telescope. The mirrors are designed assuming that Gaussian beams will be propagated through the system. The beam patterns for Bowtie 2 are shown in fig. 4.6. It is apparent from that figure that these patterns have a fairly large Gaussian component, so they should couple reasonably well to the telescope optics.

The efficiency with which the bowtie mixer illuminates the telescope is measured by comparing the receiver response to hot and cold loads placed at the Cassegrain focus (between the secondary and tertiary mirrors) with response measured with hot and cold loads directly in front of the receiver. Hot
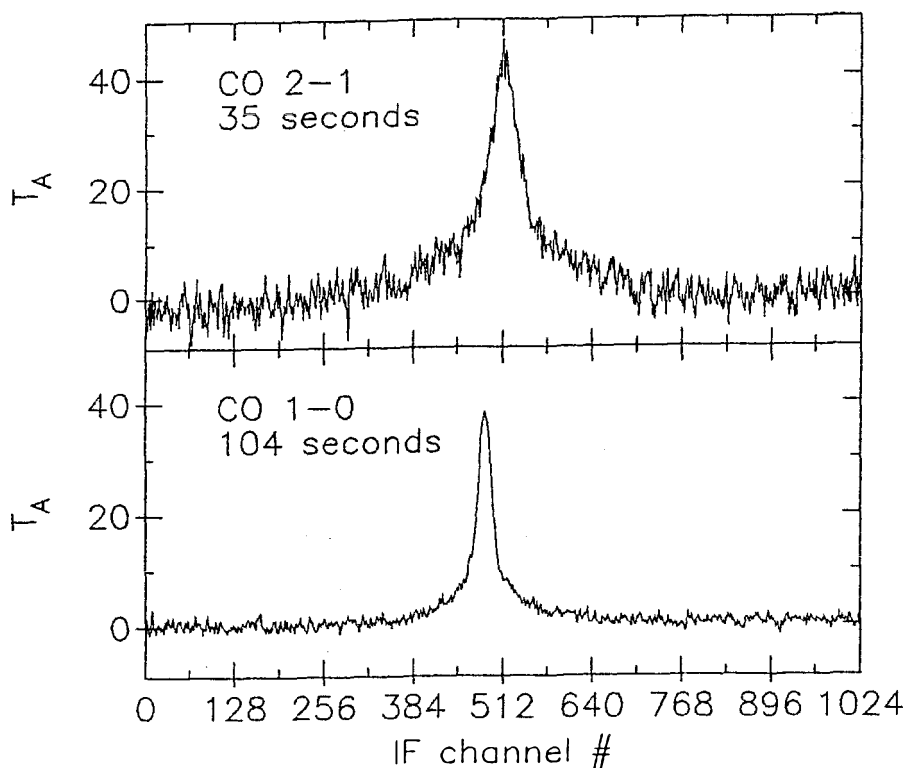
Figure 4.20 Two CO transitions in Orion measured with bowtie-SIS. The data are in 1024 channels spaced .5 MHz apart. The center channel corresponds to line frequencies of 230.531 GHz for the J=2-1 transition and 115.268 GHz for J=1-0. Signal was integrated for the times shown.

and cold load illumination produces a change in IF power, δP_{IF}. The coupling efficiency, x, of the receiver is the ratio of IF response at the Cassegrain focus to the IF response right at the receiver,

$$x = \frac{\delta P_{IF} \text{ (Cass.)}}{\delta P_{IF} \text{ (Rec.)}}.$$ (4.7.1)

The waveguide receivers in use at OVRO (Woody, Miller, and Wengler, 1985), have $x = .9$. For the bowtie receivers, $x = .6$ over the entire frequency range tested, (100-260 GHz).

Besides coupling efficiently in a spatial sense to the Cassegrain focus, it is also necessary that the bowtie beam be focussable. In classical optics, things like spherical aberration and coma result in beams which have minimum focal spots which are bigger than diffraction theory would predict. If the beam leaving the bowtie mixer has non-spherical equiphase surfaces, it will not be possible to achieve diffraction limited angular resolution with the OVRO telescope. The telescope on which the bowtie was mounted is part of a three telescope interferometer. At 115 GHz, it is possible to make extremely high
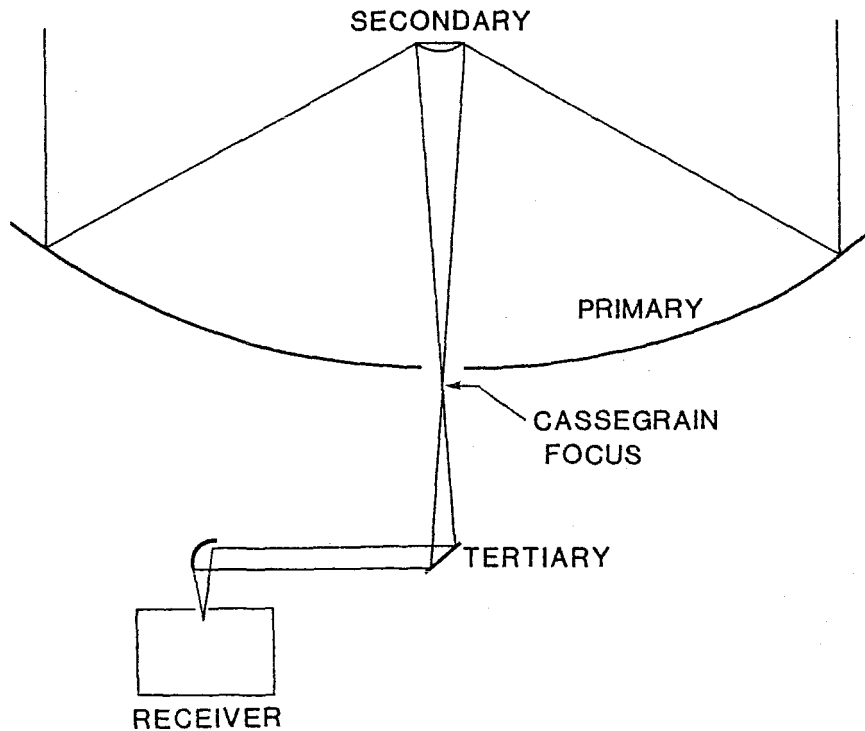
Figure 4.21 Optics on 10.4 m telescope at OVRO. The extreme rays traced are for the -13 dB contour of the Gaussian beam for which the optics are designed.

resolution maps of the beam pattern of one telescope in the interferometer by scanning that telescope around while using the other two telescopes as a constant reference. With the bowtie mixer, the aperture efficiency of the telescope was actually a little bit better than that measured with the waveguide receivers. The two mixers illuminate the primary in slightly different ways, accounting for the small difference. The important conclusion is that there is no evidence at all for any sort of aberation in the bowtie beam at 115 GHz.

At higher frequencies, it was not possible to make accurate beam measurements on the telescope. However, rough measurements at 230 GHz indicate a beamwidth that is no more than 40% wider than the diffraction limit for a 10.4 m diameter telescope. A wider beam than the diffraction limit could be due to inaccuracies in the primary dish of the antenna. It could also be due to a failure to illuminate the entire primary reflector of the telescope, causing it to behave like a smaller telescope. In any case, there is no strong evidence that the bowtie mixer beam cannot be focussed at 230 GHz, but the measurements we made do not completely rule out problems either.

The bowtie mixer was found to have double sideband response, that is, it has equal gain to signals

in the upper and lower sidebands. The CO 2–1 spectral line at about 230 GHz was observed with two different LO frequencies, so that the line was alternately in the upper and lower sidebands. The measured line intensities under these two tunings differed by 1% (which is within the noise of the measurement). As a result, it can be concluded that, at least at 230 GHz, the bowtie mixer has double sideband response to high accuracy. This is expected from the bowtie, since there are no tuning structures to give differential mixer response over a frequency range as small as the separation of the lower and upper sidebands, about 3 GHz for the IF used at OVRO.

The bowtie mixer was checked for harmonic response, none was observed. In addition to response at the upper and lower sidebands, $\nu_{LO} \pm \nu_0$, some mixers respond to higher order mixing products. In particular, signals at frequencies $2\nu_{LO} \pm \nu_0$ may be downconverted into the IF at ν_0. To test this, the LO frequency was adjusted so that the CO 2–1 line would be at $2\nu_{LO} + \nu_0$. The mixer was tuned in the normal fashion to maximize its response to hot and cold loads. The resulting spectra showed no sign of a spectral line, to an accuracy of about 2 K, or two parts in 40 for the CO 2–1 line in Orion. We thus conclude that any harmonic response in this mixer is at least 13 dB below fundamental mixing response. This is in a mixer tuned in the normal way for maximum fundamental mixing response. It is quite likely that harmonic response could be achieved with SISs if it were specially tuned to maximize that response.

In this section, we have discussed the performance of the SIS-bowtie mixer on a radiotelescope. We have found that, for the millimeter wavelengths investigated, the SIS-bowtie presents no unfortunate surprises to the radioastronomer. Its performance is generally about two-thirds as good as the SIS-waveguide mixers which have been used at OVRO (Woody, Miller and Wengler, 1985; Sutton, 1983). However, a single SIS-bowtie covers the whole 3 to 1 mm range, which requires at least two SIS-waveguide mixers. In any case, the true strength of the SIS-bowtie should lie at shorter wavelengths, where waveguide structures become increasingly inefficient and difficult to fabricate. The next step is to test the SIS-bowtie on a telescope at submillimeter wavelengths.

4.8 Conclusion

In this chapter, we have described a prototype low noise mixer for near-millimeter wavelengths (100 to 1000 GHz). A lens-coupled bowtie antenna is used for the first time in a low-noise receiver. The detectors are lead alloy SIS tunnel diodes of the same sort as are used in waveguide mixers at Caltech's Owens Valley Radio Observatory, and at AT&T Bell Labs' Crawford Hill Observatory. However, they have been fabricated so as to maximize their switching speeds, which are estimated to be .3 ps, corresponding to 500 GHz.

The bowtie mixer has demonstrated good low noise performance from 115 to 761 GHz, in laboratory measurements. This multi-octave coverage of the near-millimeter is one of the advantages of the bowtie optics. Above 300 GHz, the bowtie is approximately as good as a number of waveguide based mixers, each of which covers about a half-octave.

Telescope tests, carried out to a maximum frequency of 260 GHz, show that the SIS-bowtie is suitable for radioastronomy. At the frequencies tested, SIS-waveguide mixers are better than the SIS-bowtie. However, the real strength of the SIS-bowtie should be at submillimeter wavelengths. Telescope tests at these short wavelengths are certainly the next step that should be taken.

References

Baker, J. M., and J. H. Magerlein, "Tunnel barriers on Pb-In-Au alloy films," *J. Appl. Phys.*, vol. 54, pp. 2556–2568, May 1983.

Bardeen, J., L. N. Cooper, and J. R. Schrieffer, "Theory of Superconductivity," *Phys. Rev.*, vol. 108, pp. 1175–1204, Dec. 1957.

Barone, A., and G. Paternò, *Physics and Applications of the Josephson Effect*, John Wiley & Sons, New York, 1982.

Betz, A., speaking at U. Ill., Champaign-Urbana, April 1987.

Betz, A., and J. Zmuidzinas, "A 150 μm to 500 μm heterodyne spectrometer for airborne astronomy," *Airborne Astronomy Symposium*, NASA Conference Publication 2353, pp. 320–329, 1984.

Blundell, R., K. H. Gundlach, and E. J. Blum, "Practical low-noise quasiparticle receiver for 80–100 GHz," *Electron. Lett.*, vol. 19, pp. 498–499, June 23, 1983.

Callen, H. B. and T. A. Welton, "Irreversibility and generalized noise," *Phys. Rev.*, vol. 83, pp. 34–40, July 1951.

Caves, C. M., "Quantum limits on noise in linear amplifiers," *Phys. Rev. D*, vol. 26, pp. 1817-1839, 15 Oct. 1982.

Cohen, M. H., L. M. Falicov, and J. C. Phillips, "Superconductive tunneling," *Phys. Rev. Lett.*, vol. 8, pp. 316–319, 15 April 1962.

Compton, R. C., R. C. McPhedran, Z. Popović, G. M. Rebeiz, P. P. Tong, and D. B. Rutledge, "Bow-tie antennas on a dielectric half-space: theory and experiment," *IEEE Trans. Antennas and Propagat.*, submitted July 1986.

Cooper, L. N., "Bound electron pairs in a degenerate Fermi gas," *Phys. Rev.*, vol. 104, pp. 1189–1190, Nov. 15, 1956.

Crété, D. G., W. R. McGrath, and P. L. Richards, "Performance of arrays of SIS junctions in heterodyne mixers," *preprint*, 1987.

Dayem, A. H., and R. J. Martin, "Quantum interaction of microwave radiaton with tunneling between superconductors," *Phys. Rev. Lett.*, vol. 8, pp. 246–248, March 15, 1962.

D'Addario, L. R., "An SIS Mixer for 90–120 GHz with Gain and Wide Bandwidth," *Intl. J. of IR and Millimeter Waves*, vol. 5, pp. 1419–1442, 1985.

Danchi, W. C. and E. C. Sutton, "Frequency dependence of quasiparticle mixers," *J. Appl. Phys.*, vol. 60, pp. 3967-3978, Dec. 1, 1986.

Devyatov, I. A., L. S. Kuzmin, K. K. Likharev, V. V. Migulin, and A. B. Zorin, "Quantum-statistical theory of microwave detection using superconducting tunnel junctions," *J. Appl. Phys.*, vol. 60, pp. 1808–1828, Sept. 1986.

Dolan, G. J., "Offset masks for lift-off photoprocessing," *Appl. Phys. Lett.*, vol. 31, pp. 337–339, Sept. 1977.

Dolan, G. J., T. G. Phillips and D. P. Woody, "Low-noise 115-GHz mixing in superconducting oxide-barrier tunnel junctions," *Appl. Phys. Lett.*, vol. 34, pp. 347–349, Mar. 1, 1979.

Dunkleberger, L. N., "Stencil technique for the preparation of thin-film Josephson devices," *J. Vac. Sci. Tech.*, vol. 15, pp. 88–90, Jan. 1978.

Dynes, R. C., V. Narayanamurti, and J. P. Garno, "Direct measurement of quasiparicle lifetime broadening in a strong-coupled superconductor," *Phys. Rev. Lett.*, vol. 41, p. 1509–1511, Nov. 20, 1978.

Ellison, B. N., R. E. Miller, "A low noise 230 GHz SIS receiver," *Intl. J. of IR and Millimeter Waves*, vol. 8, no. 6, 1987.

Erickson, N. R., speaking at U. Ill., Champaign-Urbana, April 1987.

Erickson, N. R., "A very low noise single sideband receiver for 200–260 GHz," *Preprint #260 of Five College Radio Astronomy Observatory*, 1985.

Face, D. W., D. E. Prober, W. R. McGrath, and P. L. Richards, "High quality tantalum superconducting tunnel junctions for microwave mixing in the quantum limit," *Appl. Phys. Lett.*, vol. 48, pp. 1098–1100, April 21, 1986.

Face, D. W., "Quantum limited detection and noise in superconducting tunnel junction mixers," *Ph. D. thesis*, Yale University, May 1987.

Feldman, M. J., S.-K. Pan, A. R. Kerr, and A. Davidson, "SIS mixer analysis using a scale model," *IEEE Trans. Magn.*, vol. MAG-19, p. 494–497, May 1983.

Feldman, M. J., and S. Rudner, "Mixing with SIS arrays," in *Reviews of Infrared and Millimeter Waves, Vol. 1*, K. J. Button, ed., New York: Plenum Press, 1983.

Feldman, M. J., "Quantum noise in the quantum theory of mixing," *IEEE Trans. Magn.*, submitted, 1986.

Giaever, I., "Energy gap in superconductors measured by electron tunneling," *Phys. Rev. Lett.*, vol. 5, pp. 147–148, 15 Aug., 1960.

Greiner, J. H., C. J. Kircher, S. P. Klepner, S. K. Lahiri, A. J. Warnecke, S. Basavaiah, E. T. Yen, J. M. Baker, P. R. Brosious, H.-C. W. Huang, M. Murakami, and I. Ames, "Fabrication process for Josephson integrated circuits," *IBM J. Res. Develop.*, vol. 24, pp. 195–205, March 1980.

Gundlach, K. H., R. Blundell, J. Ibruegger, E. J. Blum, "SIS quasiparticle mixer receiver for radio-astronomy applications," *Proceedings of IC SQUID 1985*, Berlin, June 1985.

Gundlach, K. H., S. Takada, M. Zahn, and H. J. Hartfuß, "New lead alloy tunnel junction for quasiparticle mixer and other applications," *Applied Physics Letters*, vol. 41, pp. 294–296, 1 Aug. 1982.

Hartfuß, H. J., and M. Tutter, "Numerical design calculation of a mm-wave mixer with SIS tunnel junction," *Intl. J. of IR and Millimeter Waves*, vol. 4, pp. 993–1013, 1983.

Hartfuß, H. J., and M. Tutter, "Minimum noise temperature of a practical SIS quantum mixer," *Intl. J. of IR and Millimeter Waves*, vol. 5, pp. 717–735, May 1984.

Heffner, H., "The fundamental noise limit of linear amplifiers," *Proc. Inst. Radio Engrs.*, vol. 50, p. 1604, July 1962.

Ibruegger, J., K. Okuyama, R. Blundell, K. H. Gundlach, and E. J. Blum, "Quasiparticle 150 GHz mixer with a submicron Pb/Bi/In-oxide-Pb/Bi junction," *Proceedings of LT-17*, Eckern *et al.*, eds., Amsterdam:North Holland, 1984.

Jenkins, F. A., and H. E. White, *Fundamentals of Optics*, New York:McGraw-Hill, 1957.

Josephson, B. D., "Supercurrents through barriers," *Advances in Physics*, vol. 14, pp. 419–451, 1965.

Kingston, R. H., *Detection of Optical and Infrared Radiation*, ch. 3, New York: Springer-Verlag, 1978.

Kraus, J. D., *Radio Astronomy*, Powell, Ohio:Cygnus-Quasar, 1986.

LeDuc, H. G., J. A. Stern, S. Thakoor and S. Khanna, "All refractory NbN/MgO/NbN tunnel junctions," *IEEE Trans. Magn.*, submitted, 1986.

Louisell, W. H., *Radiation and Noise in Quantum Electronics*, S 4.3, New York, McGraw-Hill, 1964.

Marcuse, D., *Principles of Quantum Electronics*, New York: Academic Press, 1980.

McGrath, W. R., P. L. Richards, A. D. Smith, H. van Kempen, R. A. Batchelor, "Large gain, negative resistance, and oscillations in superconducting quasiparticle heterodyne mixers," *Appl. Phys. Lett.*, vol. 39, pp. 655–658, Oct. 15, 1981.

Melville, H., *Moby Dick*, New York:New American Library, 1961.

Neikirk, D. P., P. P. Tong, D. B. Rutledge, H. Park, and P. E. Young, "Imaging antenna array at 119 μm," *Appl. Phys. Lett.*, vol. 41, pp. 329-331, Aug. 1982.

Olsson, L., S. Rudner, E. Kollberg, and C. O. Lindström, "A low noise SIS array receiver for radioastronomical applications in the 35–50 GHz band," *Intl. J. of IR and Millimeter Waves*, vol. 4, pp. 847–858, 1983.

Pan, S.-K., M. J. Feldman, A. R. Kerr, and P. Timbie, "Low-noise 115-GHz receiver using superconducting tunnel junctions," *Appl. Phys. Lett.*, vol. 43, pp. 786–788, Oct. 1983.

Pan, S.-K., A. R. Kerr, J. W. Lamb, and M. J. Feldman, "SIS mixers at 115 GHz using Nb/Al$_2$O$_3$/Nb junctions," National Radio Astronomy Observatory Electronics Division internal report no. 268, April 1987.

Phillips, T. G., and K. B. Jefferts, "A low temperature bolometer heterodyne receiver for millimeter wave astronomy," *Rev. Sci. Inst.*, vol. 44, pp. 1009–1014, Aug. 1973.

Phillips, T. G. and G. J. Dolan, "SIS mixers," *Physica*, vol. 109 & 110B, pp. 2010–2019, July 1982.

Phillips, T. G., and D. P. Woody, "Millimeter- and submillimeter-wave receivers," *Ann. Rev. Astron. Astrophys.*, vol. 20, pp. 285–321, 1982.

Predmore, C. R., A. V. Räisänen, N. R. Erickson, P. F. Goldsmith, and J. L. R. Marrero, "A broad-band, ultra-low-noise Schottky Diode Mixer Receiver from 80 to 115 GHz," *IEEE Trans. Microwave Theory Tech.*, vol. MTT-32, pp. 498–506, May 1984.

Räisänen, A. V., D. G. Crété, P. L. Richards, and F. L. Lloyd, "Wide-band low noise mm-wave SIS mixers with a single tuning element," *Intl. J. of IR and Millimeter Waves*, vol. 7, pp. 1835–1852, 1986.

Richards, P. L., T. M. Shen, R. E. Harris and F. L. Llyod, "Quasiparticle heterodyne mixing in SIS tunnel junctions," *Appl. Phys. Lett.*, vol. 34, pp. 345–347, Mar. 1, 1979.

Richards, P. L., and T. M. Shen, "Superconductive devices for millimeter wave detection, mixing, and amplification," *IEEE Trans. Electronic Devices*, vol. ED-27, pp. 1909–1920, Oct. 1980.

Rickayzen, G., "The theory of Bardeen, Cooper, and Schrieffer" in *Superconductivity*, R. D. Parks, Ed., vol. 1, pp. 51–115, New York: Marcel Dekker, 1969.

Robinson, F. N. H., *Noise and Fluctuations in Electronic Devices and Circuits*, Oxford, Clarendon Press, 1974

Rogovin, D. and D. J. Scalapino, "Fluctuation phenomena in tunnel junctions," *Annals of Physics*, vol. 86, pp. 1–90, July 1974.

Röser, H. P., E. J. Durwen, R. Wattenbach, and G. V. Schultz, "Investigation of a heterodyne receiver with open structure mixer at 324 GHz and 693 GHz," *Intl. J. of IR and Millimeter Waves*, vol. 5, pp. 301–314, March 1984.

Röser, H. P., R. Wattenbach, and P. van der Wal, "Tunable heterodyne receiver from 100 μm to 1000 μm for airborne observations," *Airborne Astronomy Symposium*, NASA Conference Publication 2353, pp. 330–334, 1984.

Rutledge, D. B., and M. S. Muha, "Imaging antenna arrays," *IEEE Trans. on Antennas and Propagat.*, vol. AP-30, pp. 535–540, July 1982.

Rutledge, D. B., D. P. Neikirk, and D. P. Kasilingam, "Integrated-Circuit Antennas" in *Infrared and Millimeter Waves*, K. J. Button, Ed., vol. 10, pp. 1–90, New York: Academic Press, 1984.

Schneider, M. V., "Metal–semiconductor junctions as frequency converters" in *Infrared and Millimeter Waves*, K. J. Button, Ed., vol. 6, pp. 210–275, New York: Academic Press, 1982.

Shapiro, J. H., and S. S. Wagner, "Phase and amplitude uncertainties in heterodyne detection," *IEEE J. Quantum Electron.*, vol. QE-20, pp. 803–813, July 1984.

Shen, T.-M., *Superconductor-Insulator-Superconductor Quasiparticle Tunnel Junctions as Microwave Receivers*, Ph. D. thesis, Berkeley, 1980.

Shen, T.-M., and P. L. Richards, "Computer simulations of the performance of quasiparticle heterodyne mixers," *IEEE Trans. Magn.*, vol. MAG-17, pp. 677–683, Jan. 1981.

Shen, T.-M., P. L. Richards, R. E. Harris, and F. L. Lloyd, "Conversion gain in mm-wave quasiparticle heterodyne mixers," *Appl. Phys. Lett.*, vol. 36, pp. 777–779, May 1 1980.

Smith, A. D., and P. L. Richards, "Analytic solutions to superconductor-insulator-superconductor quantum mixer theory," *J. Appl. Phys.*, vol. 53, pp. 3806–3812, May 1982.

Smith, D. R., and E. V. Loewenstein, "Optical constants of far infrared materials. 3: plastics," *Applied Optics*, vol. 14, pp.1335–1341, June 1975.

Sutton, E. C., "A superconducting tunnel junction receiver for 230 GHz," *IEEE Trans. Microwave Theory Tech.*, vol. MTT-31, pp. 589–592, July 1983.

Sutton, E. C., G. A. Blake, C. R. Masson, and T. G. Phillips, "Molecular line survey of Orion A from 215 to 247 GHz," *Astrophysical Journal Supplement*, vol. 58, pp. 341–378, July 1985.

Tinkham, M., *Introduction to Superconductivity*, New York:McGraw-Hill, 1975.

Torrey, H. C. and C. A. Whitmer, *Crystal Rectifiers*, MIT Rad. Lab. Series, vol. 15, New York:McGraw Hill, 1948.

Tucker, J. R., and M. F. Millea, "Photon detection in nonlinear tunneling devices," *Appl. Phys. Lett.*, vol. 33, pp. 611–613, Oct. 1978.

Tucker, J. R., "Quantum limited detection in tunnel junction mixers," *IEEE J. Quantum Electron.*, vol. QE-15, pp. 1234–1258, Nov. 1979.

Tucker, J. R., in *Reviews of Infrared and Millimeter Waves*, K. J. Button, ed., New York:Plenum, 1983.

Tucker, J. R., and M. J. Feldman, "Quantum detection at millimeter wavelengths," *Rev. Modern Phys.*, vol. 57, pp. 1055–1113, Oct. 1985.

van Kempen, H., W. R. McGrath, P. L. Richards, A. D. Smith, R. E. Harris, and F. L. Lloyd, in *Digest of the Sixth International Conference on Infrared and Millimeter Waves*, K. J. Button, ed., New York:IEEE, 1981.

Weinreb, S., D. L. Fenstermacher, R. W. Harris, "Ultra-low-noise 1.2 to 1.7 GHz cooled GaAsFET amplifiers," *IEEE Trans. Microwave Theory Tech.*, vol. MTT-30, pp. 849–853, June 1982.

Weinreb, S., "SIS-mixer to HEMT-amplifier optimum coupling network," *IEEE Trans. Microwave Theory Tech.*, submitted March 1987.

Wengler, M. J., D. P. Woody, R. E. Miller and T. G. Phillips, "A low noise receiver for millimeter and submilimeter wavelengths," *Intl. J. of IR and Millimeter Waves*, vol. 6, pp. 697–706, Aug. 1985a.

Wengler, M. J., D. P. Woody, R. E. Miller and T. G. Phillips, "A low noise receiver for submilimeter astronomy," *Proceedings of the SPIE*, vol. 598, pp. 27–32, Dec. 1985b.

Wengler, M. J., D. P. Woody, "Quantum noise in heterodyne detection," *IEEE J. of Quantum Electron.*, vol. QE-23, pp. 613–622, May 1987.

Werthamer, N. R., "Nonlinear self-coupling of Josephson radiation in superconducting tunnel junctions," *Phys. Rev.*, vol. 147, pp. 255–263, 8 July 1966.

Woody, D. P., R. E. Miller, and M. J. Wengler, "85–115 GHz receivers for radio astronomy," *IEEE Trans. Microwave Theory Tech.*, vol. MTT-33, pp. 90–95, Feb. 1985.

Yamamoto, Y. and H. A. Haus, "Preparation, measurement and information capacity of optical quantum states," *Rev. Mod. Phys.*, vol. 58, Oct. 1986.

Yurke, B. and J. S. Denker, "Quantum network theory," *Phys. Rev. A*, vol. 29, pp. 1419–1437, Mar. 1984.

Zmuidzinas, J., Ph. D. thesis, U. C. Berkeley, 1987.

Zorin, A. B., "Quantum noise in SIS mixers," *IEEE Trans. Magn.*, vol. MAG-21, pp. 939–942, Mar. 1985.